T · H · E
OHIO
STATE
UNIVERSITY

AD-A229 388

Bispectral Analysis of Radar Signals with Application to Target Classification

I. Jouny, E.K. Walton, R.L. Moses and F.D. Garber

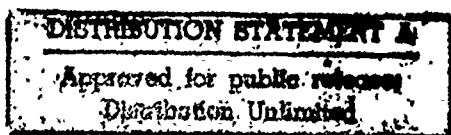The Ohio State University

ElectroScience Laboratory

Department of Electrical Engineering
Columbus, Ohio   43212

DTIC
ELECTE
NOV 26 1990
S B D

50272-101

REPORT DOCUMENTATION PAGE	1. REPORT NO.	2.	3. Recipient's Accession No.

4. Title and Subtitle	5. Report Date
Bispectral Analysis of Radar Signals with Application	August 1990
to Target Classification	6.

7. Author(s)	8. Performing Org. Rept. No.
I. Jouny, E.K. Walton, R.L. Moses and F.D. Garber	723090-2

9. Performing Organization Name and Address	10. Project/Task/Work Unit No.
The Ohio State University	
ElectroScience Laboratory	11. Contract(C) or Grant(G) No.
1320 Kinnear Road	(C)
Columbus, OH 43212	(G) N00014-90-J-1200

12. Sponsoring Organization Name and Address	13. Report Type/Period Covered
Dept. of the Navy, Chief of Naval Research	Technical Report
800 North Quincy Street, Code 1512A:EAM	14.
Arlington, VA 22217-5000	

15. Supplementary Notes

16. Abstract (Limit: 200 words)

This report investigates the bispectral processing of complex-valued radar target scattering signatures and the impact of such processing on target identification. The concept of "birange profile" as two-dimensional display of target scattering mechanisms in the range domain is introduced. It is shown that the birange profile can detect responses due to multiple scattering interactions. An algorithm is proposed to estimate the birange profiles of radar targets. Using this algorithm, multiple interactions of real aircraft are extracted, and interpreted in terms of target geometry. An algorithm that uses autoregressive parametric modeling of radar signatures to obtain high resolution birange profiles was introduced and tested using synthesized data and real scattering data. An alternative estimation procedure, which does produce the true bispectrum, was developed. The classification aspect of birange features was investigated using cross-correlation of birange profile of unknown target with that of a catalog target. It was shown that classification using birange features is inferior to classification using impulse response features if the additive noise is Gaussian. Classification with the birange when the noise is non-Gaussian yields relatively reasonable results in comparison with other classifiers. Finally, it was shown that when scattering from extraneous point scatterers is added to the data, then classification with the birange outperforms other classifiers if the signal-to-extraneous scatterers ratio is low. Keywords:

17. Document Analysis   a. Descriptors

IDENTIFICATION,
SIGNAL PROCESSING,
TARGETS,

RADAR,
STATISTICAL, (JD)

b. Identifiers/Open-Ended Terms

c. COSATI Field/Group

18. Availability Statement	19. Security Class (This Report)	21. No. of Pages
A. Approved for public release;	Unclassified	199
Distribution is unlimited.	20. Security Class (This Page)	22. Price
	Unclassified	

(See ANSI-Z39.13)   *See Instructions on Reverse*   OPTIONAL FORM 272 (4-77)
Department of Commerce

Contents

iv

List of Tables

List of Figures

Chapter 1

INTRODUCTION

1.1   Objective

This study is concerned with the processing of radar signals using higher order spectra. The purpose of radar signal processing, in general, is to extract useful information about target scattering mechanisms. Such information may be used for classification of unknown non-cooperative aircraft targets.

Two main factors can be used to evaluate any radar signal processing technique: 1) the significance of the extracted features in terms of providing a better understanding of the scattering mechanisms that can lead to more accurate description of the target geometry, and 2) the robustness of the extracted features with respect to noise contamination, changes in target position, minor changes in the target physical structure and so on.

The goal in this study is to define the advantages and limitations of the processing of radar signals using higher order spectra and to evaluate, when possible, the utility of such techniques. Although, the final goal is to detect and classify unknown radar signals, the use of the proposed processing technique in identifying scattering mechanisms in the laboratory for canonical objects and model targets is also addressed in this study. The focus is on the interpretation of the responses that result from higher order

1

spectral processing in terms of the scattering features of radar targets.

A radar target recognition system that uses higher order spectral responses as features is shown in Figure 1.1. The catalog consists of noise-free backscatter data for several aircraft at different aspect angles. The "impulse response" and the "bispectral response" of the unknown target are computed and then compared with those of the catalog targets and the decision regarding the identity of the unknown target is based on the comparison. This report is concerned with analyzing the relevant features and performances of the target recognition system shown in Figure 1.1. The proposed radar signal processing technique is tested over a wide spectrum of target models and frequency bands.

Higher order spectral processing of radar signals belongs to the class of time-domain mechanism extraction techniques [1,2]. Further, this research effort can be considered as a part of the automatic target recognition problem. A summary of the numerous contributions to the radar target identification problem is reported in [75]. These contributions include studies in the VHF and UHF frequency bands of a variety of scattering objects. Although, the emphasis in [75] is on time-domain analysis (including polarimetric studies), numerous efforts on feature selection and statistical analysis and evaluation in the frequency-domain are also summarized. Key results in these investigations relevant to the problem at hand are given in [75].

1.2 Overview of The Radar Target Recognition Problem

Automatic recognition of radar targets has been extensively investigated during the last three decades [24]. In a large number of these investigations, and in many current and proposed target identification radar systems, the
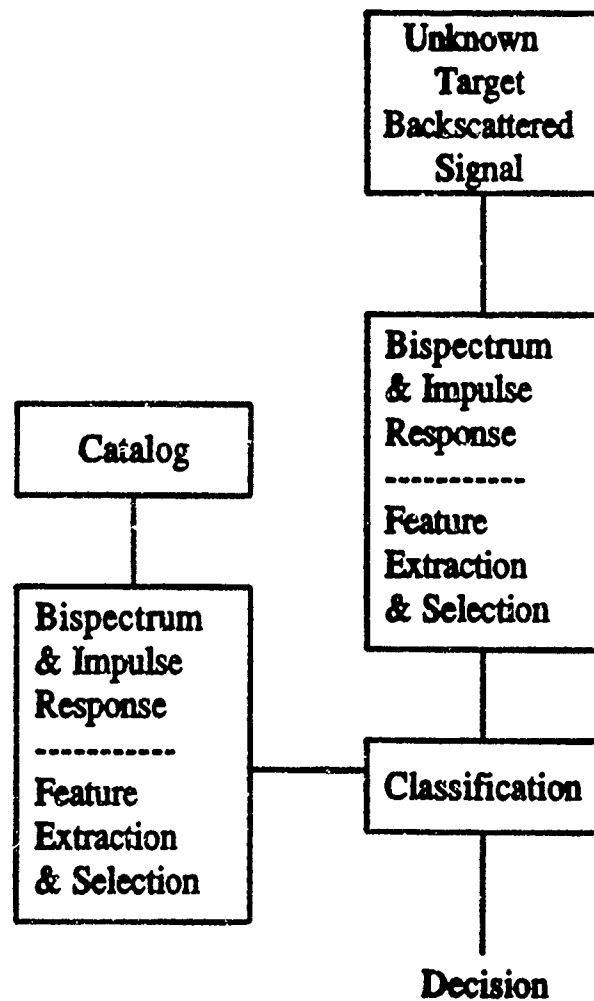
Figure 1.1: Block diagram of proposed target identification system.

radar operates at stepped frequencies. The recorded data are either calibrated scattering coefficients (complex valued) or normalized radar cross-section (RCS) at each of the stepped frequencies. The radar cross section of a target is proportional to the magnitude squared of the ratio of received to incident complex electric (or magnetic) fields and is independent of target range. In [65], the radar cross-section is defined as

$$\sigma = \frac{(4\pi).(\text{power per unit solid angle scattered towards the receiver})}{\text{power per unit area of the incident wave at the target}}$$

(1.1)

The recorded radar cross-section data (amplitude and phase), form the frequency response of a radar target. The impulse response is the inverse Fourier transform of the measured frequency response if an infinite number of samples is available. When only band-limited frequency response data are available, which is always the case in practice, the corresponding time-domain representation is known as the band limited transient response of a radar target [1,2,3]. Scattering mechanisms can be determined from the transient response [1,2].

The primary objective for any radar target recognition system is to reliably and efficiently discriminate between classes of targets using features extracted from the target responses in either the frequency or time domain. Classification of radar signals can be entirely based on the raw data in the frequency domain. Numerous approaches have been followed for the purpose of classification of unknown radar targets based on the measured band-limited frequency response [26,37,39,68]. Furthermore, a limited number of responses at discrete frequencies can be properly selected (feature selection as in [26]) in order to reduce the dimension of the problem without sacrificing considerable loss of information about the target.

Classification techniques in the frequency domain are divided into two categories: parametric and nonparametric. If prior information about the

4

probability of occurence of each target and the likelihood function of the measured noisy frequency-domain samples are known, then it is possible to use an optimal parametric classification technique that minimizes Bayes risk [38]. In some cases, classification is based on more than one frequency sample, thus improving the percentage of correct recognition. The number of samples may be fixed (Bayesian tests with fixed sample size [18]) or may vary depending on the probability of misclassification (sequential probability ratio tests [37]). If the parameters of the underlying distribution of random observations are unknown, then they can be estimated using learning techniques [38].

An alternative to estimating the parameters of the underlying distribution is to adopt a nonparametric classification approach [38]. Nonparametric classification is often based on linear discriminant functions [20] or on nonlinear functions as in neural network algorithms [25]. Also, in [39], a language theoretic approach to classification of radar targets is developed that uses syntactic recognition algorithms where each target is represented by a finite set of strings. Relational graph matching for the purpose of recognizing radar signatures is reported in [76].

Classification of radar signals can also performed in the time domain using both parametric and nonparametric decision-theoretic techniques. Time domain features include transient response (using classical Fourier algorithms), high resolution spectral processing (using autoregressive modeling [8]), and transient polarization responses (using both Fourier [75] and AR modeling [66]. Nonparametric classification of time domain features is more common simply because it is difficult to parametrize the underlying distribution, especially if nonlinear processing (such as autoregressive modeling) is used. Time-domain features, however, can be associated with the geometry and orientation of the target and may provide valuable informa-

tion about the scattering mechanisms of the target.

The performance of any target recognition system is dependent on the type of features used. The decision to adopt a certain set of features is based on the noise distribution, knowledge of the target azimuth position, and computation.

1.3   Organization of the Report

The remainder of this report is organized as follows. A background on some of the time-domain mechanism extraction techniques is provided in Chapter II. Also, a review of some of the existing radar signal processing algorithms and feature extraction techniques is presented there. A summary of the key features of higher order spectra (HOS), particularly the bispectrum, is also given in Chapter II.

Chapter III introduces the birange profile as an additional way of displaying radar signatures. Properties of the birange profile, estimation procedures, and interpretations in terms of scattering mechanisms are discussed. Examples of birange profiles for hypothetical targets, canonical objects and scaled aircraft models are presented. The validity of some of the assumptions needed to compute the bispectrum is tested. Also, Chapter III includes a study on the effect of unwanted signals (such as noise) on the birange profile. Finally, a characterization of radar targets in terms of a finite set of scattering centers and birange responses is presented.

The results reported in Chapter III are based on a classical bispectral estimation technique that use a Fourier transform methods. It is known [60] that classical signal processing of band-limited data using Fourier techniques, especially in two dimensions, yields responses with limited resolution. In Chapter IV, a parametric approach to birange profile is investigated. The focus in Chapter IV is on estimating the birange profile via

6

autoregressive modeling of radar returns. The advantages and disadvantages of this approach are discussed.

Some of the statistical properties of the birange profile are discussed in Chapter V. Further, nonparametric classification of radar targets based on the birange profile is presented. Different nonparametric classification algorithms are compared in terms of performance and efficiency.

Chapter 2

BACKGROUND

The research subject to be investigated in the following chapters is concerned with time-domain representations of radar target signatures using *higher order spectral analysis*. The scattering data (usually noisy) corresponds to calibrated radar returns at uniformly spaced frequencies. A general description of the radar system that provides the raw data, and a description of the nature of the measured data, are given below. Higher order spectral processing of radar signatures, similar to classical spectral analysis of radar data, produces signatures in the *time domain* that are related to the geometrical shape of the target. A background on spectral processing of radar signatures with emphasis on time-domain techniques is also given. Finally, an introduction to bispectral analysis of real-valued signals, properties, and estimation techniques are summarized in this chapter. We extend some of the properties of the bispectrum of real-valued signals to complex-valued signals.

2.1 Stepped Frequency Radar Measurements

The radar data considered in this study (obtained from the Ohio State University compact range) consist of coherent radar cross section measurements at a number of uniformly stepped frequencies. These measurements

8

are in units of dBm^2, which is the radar cross section of the target, relative to 1 square meter, and correspond to multipolarization modes HH (horizontally polarized transmit and horizontally polarized receive), HV, VH, and VV [64]. The data is calibrated so that all system related parameters are removed. A detailed description of the measurement process and data base can be found in [68].

The radar system simulated in this study operates mostly in the 8-58 MHz frequency range. This range of radar frequencies corresponds to the case where the size of the target is about 1-10 times the wavelength (resonant region). It was shown in [22] that this range of frequencies contains sufficient information about the shape of the target and can be used efficiently for target identification purposes. Furthermore, the target signatures over this frequency range are relatively robust with respect to changes in aspect angle. Other frequency ranges (S-band) are also considered in this study.

2.1.1 Scattering Regions Suited for This Study

The application of the bispectrum in radar signature analysis studies requires that the target scattering behavior includes significant multiple interactions. This requirement imposes some constraints on the frequency band to belong to a specific scattering region. A brief description of the three major scattering regions as a function of frequency is given below.

The ratio of the target size to the radar operating wavelength can be used to categorize the scattering properties of the target. The scattering region targeted in this study is mainly the resonance region where the scattered returns include multiple interactions.

The range of frequencies where the wavelength is large compared to the object dimensions is denoted by the Rayleigh region. The radar cross-

section in this region is proportional to the square of the frequency. The range of frequencies where the size of the target is of the order of a wavelength is the resonance region.

The range of frequencies where the wavelength is small compared to target size is the called the high frequency or optical scattering region. The coupling between currents in different parts of the body is insignificant and the scattering is more localized in this region. Scattering in this region is mainly due to specular returns in addition to diffracted returns from edges and other surface discontinuities.

2.2   Processing of Radar Signals

Radars transmit short pulses of electromagnetic waves and receive echoes from any reflector in the path of the transmitted waves. The range R to the electromagnetic waves reflector (target) is related to the time Δt elapsed between transmission and reception of echo.

$$R = \frac{c\Delta t}{2} \qquad (2.1)$$

where c is the speed of light (the 2 accounts for the two way path of radar signals). The range resolution δR, which is the minimum distance for resolving two scatterers, when the transient response is obtained using Fourier techniques, is inversely proportional to bandwidth B.

$$\delta R = \frac{c}{2B} \qquad (2.2)$$

For stepped frequency radars with an increment Δf (distance between frequency samples), an echo is expected within a time interval $[-T/2, T/2]$ where T is given by

$$T = \frac{1}{\Delta f} \qquad (2.3)$$

10

which corresponds, in units of distance, to a range r, $r = cT/2$. Thus, for a target of length L, the maximum frequency increment Δf_{max} (maximum distance between samples in frequency domain) should satisfy

$$\Delta f_{max} \leq \frac{c}{2L} \qquad (2.4)$$

This is Nyquist sampling criterion to avoid aliasing of target responses. The same criterion is sufficient to obtain unaliased bispectral responses [50].

The measured scattering coefficients at frequencies ω_l to ω_h are samples of the target transfer function (frequency response) $H(\omega)$. which, for a single point target, can be written as

$$H(\omega) = A(\omega) \exp\{j(\psi(\omega) - \omega T_r)\} \qquad (2.5)$$

where ω is the radian frequency and T_r is the time required for the radar signal to propagate to the target and back. The amplitude $A(\omega)$ of the returned signal may depend on ω, and similarly for the electric phase ψ (this is a phase change introduced by target scattering). The range to the target is simply $R = \frac{cT_r}{2}$. It is convenient to measure the range from a fixed point at the center of the target. Then, $R = R_0 + r$ where R_0 is the distance to the fixed point on the target. Similarly, the propagation time delay is $T_r = T_0 + t_r$ where $T_0 = \frac{2R_0}{c}$. Then the actual transfer function is

$$H'(\omega) = \exp(-j\omega T_0)H(\omega). \qquad (2.6)$$

A target may consist of P scattering points (or can be modeled as such). If there are no interactions between various scattering points then the transfer function is

$$H(\omega) = \sum_{i=1}^{P} A_i(\omega) \exp\{j(\psi_i(\omega) - \omega T_i\} \qquad (2.7)$$

where A_i, ψ_i, T_i' depend only on the ith scattering point. Multiple interactions between scattering points introduce extra terms that characterize

11

the coupling between the two scatterers and do not correspond to a true physical scattering object. Therefore a more accurate model of scattering from a radar target is

$$
\begin{aligned}
H(\omega) \quad = \quad & \sum_{i=1}^{p} A_i(\omega) \exp\left\{-j(\psi_i(\omega) - \omega T_i)\right\} \\
& + \sum_{k=1}^{p} \sum_{l=1}^{p} A_{kl}(\omega) \exp\left\{-j(\psi_{kl}(\omega) - \omega(T_{kl}))\right\} \\
& + \dots
\end{aligned}
\tag{2.8}
$$

Usually the magnitude A_{kl} of the scattered signals due to an interaction between two specular scattering centers is small compared to either A_k or A_l. However, this is not always the case, especially for certain classes of canonical targets [71]. Conventional radar targets such as aircraft, ships, or tanks are complicated to the extent that one can no longer exclude the possibility of a significant number of interactions with relatively large magnitudes. It is likely, but not necessary, that the interactions between scatterers become smaller in magnitude as the number of interacting scatterers is increased. One focus of this study is to investigate the use of the bispectrum for discriminating between specular scattering and multiple interaction scattering. The use of the trispectrum and even higher order spectral analysis can also be related to more complex scattering mechanisms. In this study we consider only the bispectrum.

Signal processing techniques can be applied in either the time or frequency domain. The measured frequency response has important intrinsic characteristics that permit the extraction of important features such as complex natural resonances (CNR) [70]. Such features are extracted by applying spectral processing techniques to the recorded data over finite bandwidth. Although the emphasis in this report is on time-domain radar signal processing, a summary of spectral analysis studies when applied to frequency-domain data is given below. It will be shown later that the same

spectral estimation techniques can be applied to either time or frequency domain representations of target responses and the difference is only in the characteristics of the extracted features. Therefore, the application of higher order spectra is not limited to time-domain waveforms but may have important applications in the frequency domain as well.

2.2.1 Signal Processing of Radar Signatures: Frequency-Domain

The transient response properties of scattering objects are characterized by their complex natural resonance. The number of natural resonances of scatterers is infinite. Kennaugh [2] suggested that it is possible to approximately characterize the transient responses of scatterers at longer times with a finite number of low-frequency natural resonances. The complex natural resonances can be determined using an iteration process which searches for the zeros of the impedance determinant of the object in the frequency domain [72]. Chuang and Moffatt [72] used the Prony method to extract complex natural resonances from approximate backscattered ramp responses of radar targets.

If a plane wave $E_i = E_0 \exp\{j(\omega t - kr)\}$ is transmitted to illuminate a target, then the backscattered field is $E_s = E_0 c \frac{H(j\omega)}{2r} \exp\{j(\omega t - 2kr)\}$ where $H(\omega)$ is the transfer function seen by the radar and r is the range to the target. If a ramp signal $tu(t)$ (where $u(t) = 1 \quad t > 0, 0$ otherwise) is transmitted, then the ramp response is related to the frequency response as follows

$$h_R(t) = \frac{1}{2\pi} \int_{-\infty}^{\infty} \frac{H(j\omega)}{(-\omega^2)} \exp\{j\omega t\} d\omega \qquad (2.9)$$

The ramp response $h_R(t)$ can then be written, using Fourier series expansion, as

$$h_R(t) = \sum_{n=1,3,\ldots}^{\infty} \frac{2T}{\pi^2 n^2} \left| H\left(\frac{j\pi n}{T}\right) \right| \cos\left(\frac{\pi n}{T} t + \phi_n\right) \qquad (2.10)$$

13

where ϕ_n is the phase of $H(j\omega)$ at $\omega = \pi n/T$ [72]. If one considers the first few terms in the above expansion (which is a reasonable assumption because as the coefficients of the Fourier series are weighted by n^2) then it is easy to notice the resemblance to the function

$$f(t) = \sum_{i=1}^{N} A_i \exp\{\gamma_i t\} \tag{2.11}$$

where the parameters A_i, γ_i can be estimated using the Prony method [72]. The poles γ_i extracted using Prony method represent the dominant natural resonances of the target. The complex natural resonances (CNR's) of a target are *aspect independent* and therefore have been proposed as an aspect insensitive method for discriminating between targets. The Prony algorithm is sensitive to noise contamination [72] and may produce inaccurate CNR's. The extraction of complex natural resonances from noisy radar signals remains an active research area.

For electrically small objects, the CNR's can be obtained from an integral equation formulation and numerical search [73]. For targets with complicated geometry the extraction of the CNR's is from either measured scattering data or from measured surface currents. The Prony method, like most high resolution techniques, requires prior knowledge of the model order (N in equation (2.11)).

Frequency domain target identification studies focus on the extraction of complex natural resonances that are aspect independent features. No information, however, about the scattering mechanisms of a radar target are directly evident from the frequency response data.

2.2.2 The Impulse Response

The information about target shape, size, and orientation resides in the measured backscattered frequency response. Such information can be ex-

tracted by examining the target scattering mechanisms that are displayed in the target impulse response.

In general, electromagnetic scattering from most objects tends to be localized at specific areas. In [70], the individual scatterers are represented as specular reflection, edge diffraction and creeping wave mechanisms. It is often convenient to separately quantify the scattering cross section of each mechanism, particularly for experimental purposes. This can only be accomplished if the response to each individual scatterer is separable and is often done by processing windowed scattering spectrum using the fast Fourier transform (FFT) [5]. The FFT of the band-limited frequency response $H(\omega)$ is the bandlimited transient response. A thorough discussion on the application of transient and impulse response in scattering studies can be found in [2].

The relationship between the impulse response and radar cross section can be described as follows. If an impulsive plane wave E_i is reflected by a linear scatterer [70] then the scattered field $h(t)$, is defined as the impulse response and its Fourier transform $H(\omega)$ is the transfer function of the target as seen by the radar. If a monochromatic plane wave $(\exp\{j\omega t\})$ strikes an object, then the phasor response $H(\omega)$ is related to a transverse component of the scattered electric field, $E^s(t - \frac{r}{c})$ at large r by [70]

$$\Re\left[H(\omega)\exp\left(j\omega(t - \frac{r}{c})\right)\right] = \frac{2r}{c}E^s(t - \frac{r}{c}) \qquad (2.12)$$

where r is the range from scatterer to radar and c is the speed of light, and $\Re$ denotes the real part operation. The radar cross section of the target σ is related to $H(\omega)$ as [70]

$$\sigma = \lim_{r\to\infty} 4\pi r^2 \left|\frac{E^s}{E_i}\right|^2 \qquad (2.13)$$

$$= c\pi |H(\omega)|^2 \qquad (2.14)$$

A more concise definition of the impulse response, [70] is: *The im-*

15

pulse response waveform is the time-dependent electromagnetic field inten-
sity produced at a fixed point in space when a plane electromagnetic im-
pulsive wave strikes an object. If the impulse response is known, then the
scattered signal for any incident pulse shape can be predicted [70]. The
impulse response concept (or the time-domain profile) is widely used for
scattering analysis [2,5,8,10] because it adds insight to the complex rela-
tion between the shape of the target and its reflectivity [70]. To further
emphasize the importance of the impulse response (or transient response)
in electromagnetics research, it is claimed in [70] that such techniques make
it possible to integrate all existing information concerning an object into a
single characteristic function, thus combining the best features of several
approximate methods such as Rayleigh theory, physical optics, geometrical
theory of diffraction, etc. into a single waveform given a specific aspect and
polarization [70].

2.2.3 Signal Processing of Radar Signatures: Time-Domain

The problem concerned with the extraction of scattering mechanisms of a
radar target in order to acquire some information about the target size and
geometry has been investigated by numerous researchers during the last
three decades. There are two aspects to this problem:

- Resolving two closely spaced peaks in the impulse response or discrim-
  inating two distinct mechanisms that are spaced by small increment
  in time.

- Associating each mechanism in the transient response with a physical
  scattering phenomenon. That is, resolving the integration of all scat-
  tering mechanisms into classes of mechanisms (specular, interactions,
  creeping waves, etc...).

16

The first aspect of the problem is a signal processing problem where the resolution of two closely spaced peaks is limited by the bandwidth of the measured frequency response if the transient response was obtained using Fourier transform technique. Some studies suggest using high resolution spectral estimation techniques in order to overcome the bandwidth limitation constraint. The second aspect of the problem is related to the electromagnetic scattering behaviour and depends, not only on the bandwidth, but on the range of frequencies used for measurements (Rayleigh, resonance, optical, etc..).

Improving the resolution will generally have positive impact on the mechanism identification problem. One should be careful, however, that some of the techniques used to improve the resolution are prediction based techniques that implicitly extrapolate the spectrum outside the measurement window. The extrapolated spectrum using signal processing techniques may differ from the true spectrum. This could result in false scattering mechanisms that cannot be associated with the geometry of the target. Thus, a compromise between achieving a high resolution transient response without grossly changing the target scattering features is required.

This study is concerned with both sides of the time-domain signal processing problem. We will use higher order spectra (HOS) to help in solving the mechanism identification problem and we will also study the use of parametric HOS to help solve the bandwidth limitation problem. Several approaches to obtain high resolution transient responses are summarized below. These techniques, slightly modified, may be used to obtain high resolution bispectral responses.

Autoregressive modeling of radar signatures

The key to the estimation of high resolution transient responses is to assume that the scattering data satisfies a certain model. Autoregressive modeling of frequency response is one possibility. In [7] it is assumed that the measured scattering coefficients y_n at the nth frequency satisfy the autoregressive model

$$y_n = \sum_{i=1}^{p} a_i y_{n-i} + e_n \qquad (2.15)$$

where a_i is the ith AR coefficient $\{e_n\}$ is a zero mean Gaussian distributed random signal with variance ρ, and p is the model order. Autoregressive modeling of frequency-domain target signatures permits the estimation of the transient response scattering centers in terms of the zeros of the above difference equation satisfied by the data. The model order is assumed to be known *a priori* and this means (when translated to electromagnetic terms) a prior knowledge of the number of scattering mechanisms. The autoregressive model for radar data is physically intuitive because responses at one radar frequency can be approximately expressed as a linear combination of responses at other frequencies. Autoregressive modeling can be sensitive to noise contamination because of implicit nonlinearities. In [7], this model was used for identification and classification of commercial aircraft transient responses. The results in [7] indicate that the above model produces satisfactory performance for SNR above 10 dB.

Autoregressive moving average modeling (ARMA)

Autoregressive (AR) modeling assumes that the transient response of a scattering object consists only of peaks at different points in time, and no nulls. More accurate modeling of radar signatures would include both peaks and nulls (poles and zeros). Thus, autoregressive moving average modeling is an alternative choice.

In [8], the measured scattering coefficients at the nth frequency is assumed to satisfy the following ARMA model

$$y(f_n) = -\sum_{i=1}^{p} a_i y(f_{n-i}) + \sum_{j=0}^{q} c_j e(f_{n-j}) \qquad (2.16)$$

where $e(*)$ is zero mean white noise and p, q are the model orders. The target impulse response is given as

$$Y(t) = \frac{C\left(\exp\left\{j\pi(1 - 2t/T)\right\}\right)}{A\left(\exp\left\{j\pi(1 - 2t/T)\right\}\right)} \qquad (2.17)$$

where $C(*), A(*)$ are polynomials given as

$$
\begin{aligned}
A(x) &= 1 + a_1 x + \ldots + a_p x^p \\
C(x) &= 1 + c_1 x + \ldots + c_q x^q
\end{aligned}
\qquad (2.18)
$$

The orders p and q may be chosen *a priori*, or can be estimated from the data. One of the findings in [8] is that only 20 samples are needed to generate an impulse response that includes the mechanisms extracted by Fourier techniques using 150 samples. Noise is a problem, especially at low SNR's, but this method may be useful in a low noise environment where the main objective is to study scattering mechanisms. Although, both p and q have to be specified (while in the AR modeling case, only p is needed) it is claimed in [8] that ARMA modeling produces more accurate results than AR modeling.

Impulse response estimation via maximum entropy method

The maximum entropy method (MEM) can be used to obtain high resolution transient responses [5,9]. The MEM estimation technique does not require the data to be stationary or the samples to be uniformly spaced but it requires the exact values of the autocorrelation function of the data [62]. According to Jaynes [62], the estimation of the autocorrelation function

19

does not yield an accurate transient response, especially if the data is noisy, and it does not necessarily maximize the entropy of the data. Unfortunately, in the target identification problem, only estimates of the autocorrelation of the frequency response are available.

In [5], the MEM transient response estimation technique is compared to Fourier methods. It is shown that closely spaced scatterers of some canonical objects are easily resolved using maximum entropy method even though the data is nonstationary. As in the AR case, the model order should be known *a priori* in order to apply the MEM technique. Furthermore, it is important to avoid the line splitting problem in MEM which indicates the existence of two closely spaced scatterers where there is only one scattering mechanism.

Transient response using MUSIC algorithm

The MUlti SIgnal Classification algorithm (MUSIC) is used in [7] to obtain high resolution estimates of scattering mechanisms. The MUSIC algorithm produces satisfactory results when the measured scattering coefficients are noisy. The scattering data is assumed to be sinusoidal with a uniformly distributed random phase (the electric phase ψ). The covariance matrix of the noisy data is given as

$$\Phi(\omega) = E\{H'(\omega)H'^*(\omega)\} \tag{2.19}$$

$$= H(\omega)H^*(\omega) + \sigma^2 I \tag{2.20}$$

$$= \sum_i \lambda_i e_i e_i^T \tag{2.21}$$

where $H'(\omega) = H(\omega) + n(\omega)$, σ^2 is the noise variance, and I is the identity matrix. The eigenvalues and eigenvectors of the covariance matrix Φ are denoted by λ_i and e_i respectively. The matrix Φ is Hermitian and the space spanned by its eigenvectors can be divided into two subspaces, one spanned

by noise and the other subspace is spanned by eigenvectors associated with scattering mechanisms. Details of the algorithm can be found in [7].

This algorithm assumes that ψ is uniformly distributed over $[0, 2\pi]$. It is possible to avoid this assumption by manipulating the data in $H'(\omega)$ and thus randomizing ψ. This is done by dividing the measured data into subbands with subband covariance matrices. Then the covariance matrix Φ is simply the average of all subband covariance matrices [7].

In addition to high resolution estimation of scattering centers, the MUSIC algorithm also requires less data than conventional Fourier techniques. The main disadvantage of the MUSIC algorithm as well as AR, ARMA, MEM techniques, is the loss of information about the amplitude of scattering mechanisms. These algorithms are mainly used to estimate the location of scattering mechanisms in time.

Extensions of the MUSIC algorithm to higher order spectra are derived in [30]. Unfortunately, the computational burden becomes significant and the dimensions of the covariance matrix increase rapidly.

Transient response estimation using Prony based models

One may argue that all the above techniques are based on statistical spectral estimation theory; however, in the RTI problem the data may consist of a deterministic signal corrupted by additive noise. Furthermore, the stationarity of the radar scattering data is not a strictly valid assumption. Therefore, a more appropriate radar data model should be based on a deterministic modeling approach. The Prony method is a deterministic approach to modeling of radar data. In [67], the transient response is estimated using an improved version of the Prony method.

In the Prony method the scattering y_n at the nth frequency is modeled

21

as

$$y_n = \sum_{i=1}^{m} d_i p_i^n \qquad (2.22)$$

where m is the number of scatterers (known a priori). This data satisfies the AR model

$$y_n + \sum_{i=1}^{m} a_i y_{n+i} = 0 \qquad (2.23)$$

The poles p_i are estimated using the same equations as AR parameter estimation methods where the covariance matrices are replaced with data matrices and the amplitudes d_i are then estimated directly from the data in terms of the estimates of the poles p_i. Singular value decomposition of an associated data matrix results in improved estimation of the poles especially for noisy backscattered signals. Although it is necessary to know the model order *a priori*, it seems that this method is less sensitive than other parametric techniques to changes in model parameters and frequency band employed [67].

2.3   Introduction to The Bispectrum

The focus in this report is on the processing of radar data (treated as a time series) using higher order spectral analysis techniques and the bispectrum in particular. The application of HOS in radar scattering analysis is novel and the goal of this study is to investigate the benefits, if any, of applying HOS to target signatures. There is no doubt that HOS processing of any set of data provides additional knowledge about the hidden characteristics of the data. Higher order spectra, and the bispectrum in particular, are not commonly used in the radar community. For this reason, a brief summary of the bispectrum in a signal processing framework is given below. In this summary, we investigate some properties of the bispectrum of complex-valued signals.

22

Signal processing using higher order spectra was suggested by Brillinger and Rosenblatt in [12]. The bispectrum has long been considered a valuable tool for analyzing nonlinear processes, and there are numerous applications of the bispectrum in a wide variety of nonlinear problems and disciplines [11]. But the interest in the bispectrum as a general signal processing technique is recent. The reason is that the bispectrum is computationally expensive technique with limited rewards. That is, the additional knowledge provided by the bispectrum has not justified the increased computational burden. Also, the mathematics of the bispectrum are far more complicated than for other spectral analysis techniques, and the physical insight of the bispectrum is not fully understood. Today, with the development of fast computing facilities, more attention is given to the bispectrum and its applications. The main problem that remains unsolved is the intuitive interpretation and understanding of bispectral processing of a time series.

Currently, there are three main applications for higher order spectra in signal processing. These applications are stated in [11] as follows: 1) to extract information about deviation from Gaussianness (normality) [11], 2) to estimate the phase and amplitude of a non-Gaussian parametric signals [11], and 3) to detect and characterize the nonlinearities of mechanisms in a time series [11]. The first application is based on the fact that for a Gaussian signal all polyspectra of order greater than two are identically zero. The second application is based on the fact that the bispectrum preserves the phase information of non-Gaussian parametric signal [11]. The third application is due to the fact that HOS plays a key role in detecting and characterizing nonlinearities from the output data of a nonlinear system [11].

Recently, the interest in the bispectrum as a signal processing tool has

23

moved into different research areas and disciplines. There are numerous papers on the bispectrum in analyzing data structures such as electroencephalogram (EEG) data [30], seismic data [49], ocean gravity waves [51], sonar data [11], underwater acoustic transients [50], and bioelectric data. There are also several applications of the bispectrum in texture discrimination, reconstruction of shift and invariant objects, tomography, image reconstruction, non-Gaussian image modeling [59]. Cumulants and bispectra are also used to separate stochastic processes and in training of neural networks and adaptive antenna arrays and detection problems [59]. In [44] Bartelt et. al. propose an algorithm to estimate the phase and amplitude of the original signal from its triple correlation using bispectral processing. Signal reconstruction using the bispectrum is also investigated in [49]. Furthermore, two sub-optimal detection schemes using both spectra and bispectra are proposed in [56,57].

To our knowledge, there does not exist any published literature on the bispectrum of radar signals other than our recent work in [21,52]. The following chapters address this novel problem of bispectral processing of radar signals and its impact on identification of scattering mechanism and target classification.

2.3.1 Definitions

Real-Valued Random signals:

Higher order spectra are defined in terms of cumulants (often called cumulant spectra) [11]. Given a set of n real random variables $\{x_1, x_2, \ldots, x_n\}$, the joint cumulants of order $r = k_1 + k_2 + \ldots + k_n$ are defined as

$$C_{k_1 \ldots k_n} = \left((-j)^r \frac{\partial^r \ln \Phi(\omega_1, \ldots, \omega_n)}{\partial \omega_1^{k_1} \ldots \partial \omega_n^{k_n}} \right)_{\omega_1 = \ldots = \omega_n = 0} \tag{2.24}$$

where

$$\Phi(\omega_1, \ldots, \omega_n) = E\{\exp\left[j(\omega_1 x_1 + \ldots + \omega_n x_n)\right]\} \qquad (2.25)$$

The joint moments of order r of $\{x_n\}$ is given as

$$m_{k_1 \ldots k_n} = \left((-j)^r \frac{\partial^r \Phi(\omega_1, \ldots, \omega_n)}{\partial \omega_1^{k_1} \ldots \partial \omega_n^{k_n}}\right)_{\omega_1 = \ldots = \omega_n = 0} \qquad (2.26)$$

$$= E\{x_1^{k_1} x_2^{k_2} \ldots x_n^{k_n}\} \qquad (2.27)$$

The joint cumulants are related to the joint moments. For example, if the first moment is zero then assuming that we have a single random variable x_1 [11]

$$C_{10\ldots0} = 0 \qquad (2.28)$$

$$C_{20\ldots0} = m_{20\ldots0}$$

$$C_{30\ldots0} = m_{30\ldots0}$$

$$C_{40\ldots0} = m_{40\ldots0} - 3m_{20\ldots0}^2$$

For a zero mean process the third order moment is equal to the third order joint cumulant. A random process $\{x_l\}_{l=1}^n$ is stationary to order $m = k_1 + \ldots + k_n$, if

$$E\{x_1^{k_1} x_2^{k_2} \ldots x_n^{k_n}\} = E\{x_{1+i}^{k_1} x_{2+i}^{k_2} \ldots x_{n+i}^{k_n}\}.$$

If the random process $\{x_k\}_{k=1}^n$ is stationary with zero mean then the second and third order joint cumulant (identical to second and third order joint moment) are given as

$$C_{110\ldots0}(k, l) = E\{x(k)x(l)\} \quad \text{or} \qquad (2.29)$$

$$C_2(m) = E\{x(k)x(k+m)\}$$

$$C_{1110\ldots0}(j, k, l) = E\{x(j)x(k)x(l)\} \quad \text{or} \qquad (2.30)$$

$$C_3(m, n) = E\{x(k)x(k+m)X(k+n)\}$$

Notice that the fourth order cumulant is not identical to fourth order moment. If the process has non-zero mean then the cumulant $C_{110...0} =$ Covariance$\{x(k)x(l)\}$. The general relation between moments and cumulants have been derived by Leonov and Shiryaev [14] as

$$E\{x_1 \ldots x_n\} = \sum_{\gamma_1, \ldots, \gamma_p} C(\gamma_1)C(\gamma_2) \ldots C(\gamma_p)$$

where the summation extends over all partitions γ_i of the integers $(1, \ldots, n)$; and $C(.)$ are the cumulants of $\{x_n\}$. The following examples (given in [14]) are based on this theorem

$$E\{x_k\} = C(k)$$
$$E\{x_k x_l\} = C(k)C(l) + C(k, l)$$
$$E\{x_j x_k x_l\} = C(j)C(k, l) + C(k)C(j, l) + C(l)C(j, k) + C(j, k, l)$$

If we assume $E\{x_i\} = 0, \forall\, i$, then we obtain the relation [14]

$$E\{x_j x_k x_l x_m\} = C(j, k)C(l, m) + C(j, l)C(k, m)$$
$$+ C(j, m)C(k, l) + C(j, k, l, m)$$

If x_k is a Gaussian random variable then $C(j, k, l, m) = 0$.

The following are few important properties of cumulants (taken from [13,14]),

- Cumulant$(a_1 x_1, a_2 x_2 \ldots, a_n x_n) = a_1 a_2 \ldots a_n$ Cumulant$(x_1, \ldots, x_n)$.

- If the random process can be partitioned into two disjoint sets that are independent from each other, then Cumulant$(x_1, \ldots, x_n) = 0$.

- Cumulant$(x_1 + y_1, \ldots, x_n + y_n) =$Cumulant$(x_1, \ldots, x_n) +$ Cumulant$(y_1 + \ldots, y_n)$, where $\{x_n\}$ and $\{y_n\}$ are two independent random processes. This relation does not hold for moments.

26

The spectrum and bispectrum are defined as the Fourier transform of the second and third order joint cumulants respectively [11].

$$S(\omega) = \sum_{m=-\infty}^{\infty} C_2(m) \exp\{-j(\omega m)\} \qquad (2.31)$$

$$B(\omega_1, \omega_2) = \sum_{m=-\infty}^{\infty} \sum_{n-\infty}^{\infty} C_3(m, n) \exp\{-j(\omega_1 m + \omega_2 n)\} \qquad (2.32)$$

Unlike the spectral density, the bispectrum is generally complex. A sufficient condition for the existence of the bispectrum is that the third order cumulant is absolutely summable.

The bispectrum is also defined for a continuous time signal $x(t)$ as [11]

$$C_3(\tau_1, \tau_2) = E\{x(t)x(t+\tau 1)x(t+\tau 2)\} \qquad (2.33)$$

$$B(\omega_1, \omega_2) = \int_{-\infty}^{\infty} \int_{-\infty}^{\infty} C_3(\tau_1, \tau_2) \exp\{-j(\omega_1 \tau_1 + \omega_2 \tau_2)\} d\tau_1 \ d\tau_2 (2.34)$$

Little insight is provided from the above definition of the bispectrum. Intuitively, using equation (2.32), a spiky bispectrum is the result of flat triple correlation and therefore the time series $x(t)$ changes slowly over time intervals. A flat bispectrum, however, implies that the time series changes rapidly over short intervals of time.

An alternative definition of the bispectrum is based on the Cramer (or Fourier-Stieltjes) spectral representation $dZ(\omega)$ [11], where the time series $\{x(k)\}$ can be written as

$$x(k) = \frac{1}{2\pi} \int_{-\infty}^{\infty} \exp\{j\omega k\} \ dZ(\omega) \qquad (2.35)$$

where $dZ(\omega)$ is random process with

$$E\{dZ(\omega)\} = 0 \qquad (2.36)$$

$$E\{dZ(\omega_1)dZ^*(\omega_2)\} = 2\pi S(\omega)d\omega, \quad \omega_1 = \omega_2 = \omega$$

$$E\{dZ(\omega_1)dZ(\omega_2)dZ^*(\omega_3)\} = B(\omega_1, \omega_2)d\omega_1 d\omega_2, \quad \omega_1 + \omega_2 = \omega (2.37)$$

then

$$x(k) = \sum_{\omega=-\infty}^{\infty} X(\omega) \exp\{j\omega k\} \quad \text{then} \qquad (2.38)$$

$$S(\omega) = \langle X(\omega)X^*(\omega) \rangle \quad \text{and}$$

$$B(\omega_1,\omega_2) = \langle X(\omega_1)X(\omega_2)X^*(\omega_1+\omega_2) \rangle. \qquad (2.39)$$

where $\langle\rangle$ denotes the ensemble average. The above definition of the bispectrum is more insightful than the cumulants based definition. This definition implies that the bispectrum at a particular frequency pair (ω_i,ω_j) (or bifrequency) is nonzero if at least one of the three spectral responses $X(\omega_i), X(\omega_j)$, and $X(\omega_i+\omega_j)$ is correlated with the other two.

Real-Valued Deterministic signals

The definition of the bispectrum given in the previous section is based on the expectation of the triple product of a random signal. In many practical deconvolution and filtering problems the signal is deterministic. Also, the addition of noise to the deterministic signal produces a nonstationary random signal. The expectation based definition of the bispectrum is not applicable for time varying deterministic signals even if these signals are embedded in noise. The following definition of the bispectrum is applicable if the measured time series has a deterministic time varying component added to a random component such as noise. The distinction between deterministic and time varying signals, however, is only in the statement of the problem and not in the estimation procedure.

Bispectrum of Real-Valued Energy signals [79]:

If $\{x(k)\}$ is a real energy signal i.e.,

$$E_x = \sum_{k=-\infty}^{\infty} |x(k)|^2 < \infty \qquad (2.40)$$

28

then, the spectrum of $\{x(k)\}$ is given as

$$X(\omega) = \sum_{k=-\infty}^{\infty} x(k) \exp\{-j\omega k\} \qquad (2.41)$$

and the second and third moments are given as

$$M_2^x(m) = \sum_{k=-\infty}^{\infty} x(k)x(k+m) \qquad (2.42)$$

$$M_3^x(m,n) = \sum_{-\infty}^{\infty} x(k)x(k+m)x(k+n)$$

the spectral and bispectral densities are respectively

$$S^x(\omega) = X(\omega)X^*(\omega) \qquad (2.43)$$

$$B^x(\omega_1,\omega_2) = X(\omega_1)X(\omega_2)X^*(\omega_1+\omega_2)$$

Notice that the bispectrum for deterministic signals is defined in terms of moments and that of random signals is defined in terms of cumulants. Also notice that the estimation procedures for both third order cumulants and third order moments are identical.

Bispectrum of Real-Valued Periodic signals [79]:

If the sequence $\{x(k)\}$ is periodic, i.e., $x(k+N) = x(k)$ then $x(k)$ is a power signal with finite average power given by $S^x = \frac{1}{N}\sum_{k=0}^{N-1}|x(k)|^2$. The line spectrum of $\{x(k)\}$ is obtained using discrete Fourier transform defined as

$$x(k) = \frac{1}{N}\sum_{n=0}^{N-1} X(n)\exp\{j2\pi kn/N\} \qquad (2.44)$$

$$X(n) = \sum_{k=0}^{N-1} x(k)\exp\{-j2\pi kn/N\}$$

where $X(n)$ is also periodic with period N. The second and third order moments are given as

$$R_2^x(m) = \frac{1}{N}\sum_{k=0}^{N-1} x(k)x(k+m) \qquad (2.45)$$

$$R_3^x(m,n) = \frac{1}{N}\sum_{k=0}^{N-1} x(k)x(k+m)x(k+n)$$

29

and the spectral density and bispectrum are, respectively

$$S^x(p) = \frac{1}{N}X(p)X^*(p) \tag{2.46}$$

$$B^x(p,q) = \frac{1}{N}X(p)X(q)X^*(p+q)$$

The estimation of polyspectra of periodic signals is similar to that of energy signals with finite data lengths.

2.3.2 Properties of The Bispectrum of Real-Valued Signals

The cumulant $C(m,n)$ of a real stationary random sequence $\{x(k)\}$ has six symmetry regions in the two-dimensional time domain. These symmetry regions are defined by the following equations [11]

$$
\begin{aligned}
C(m,n) &= C(n,m) \tag{2.47}\\
&= C(-n,m-n)\\
&= C(n-m,-m)\\
&= C(m-n,-n)\\
&= C(-m,n-m)
\end{aligned}
$$

Therefore it suffices to compute third order cumulant in one region, and the other sectors can be generated using the above relations. Figure 2.1 shows how these symmetry regions are distributed in the (m,n) plane. Notice that with this type of skewed symmetry, the correspondence between data points in one sector is not a twofold symmetry in the other sector. Figure 2.2 shows how the data is arranged in different sectors of the (m,n) plane. For example, samples that are distributed horizontally in the sector $m,n \geq 0$, $m \geq n$ are the mirror image of the sector $m,n \geq 0$, $m \leq n$ but they are arranged vertically in the sector $m \leq 0, n \geq 0$. The arrows in Figure 2.1 indicate the arrangement of cumulant samples (from c to b) in

30

each symmetry sector of the third order cumulant plane. All sides of the symmetry triangles are labeled accordingly for all symmetry regions (see Figure 2.1). Furthermore, the data samples on the axis $m \geq 0$ has a mirror image on the axis $n \geq 0$ but the third image is on the diagonal defined by $m, n \leq 0$, and $m = n$. Therefore a set of responses on the axes $m \geq 0$, or $n \geq 0$ may look similar but less dense on the third axis $m = n, m, n \leq 0$.

The bispectrum $B(\omega_1, \omega_2)$ of a real stationary sequence $x(k)$ has twelve symmetry regions. The twelve sectors in the two-dimensional frequency domain are related as [11]

$$
\begin{aligned}
B(\omega_1, \omega_2) &= B(\omega_2, \omega_1) \qquad\qquad (2.48)\\
&= B^*(-\omega_2, -\omega_1)\\
&= B^*(-\omega_1, -\omega_2)\\
&= B(-\omega_1 - \omega_2, \omega_2)\\
&= B(\omega_1, -\omega_1 - \omega_2)\\
&= B(\omega_2, -\omega_1 - \omega_2)
\end{aligned}
$$

The bispectrum is generally complex with an amplitude and phase. Also, for discrete signal processing, the bispectrum is doubly periodic with period 2π.

$$
B(\omega_1, \omega_2) = B(\omega_1 + 2k\pi, \omega_2 + 2l\pi). \qquad (2.49)
$$

Figure 2.3 shows the twelve symmetry regions of the bispectrum. The principle triangle in the first quadrant of the (ω_1, ω_2) plane is defined by $\omega_1 \geq \omega_2$ and $\omega_1 \leq \pi$. There is an additional triangle that is adjacent to the principle triangle and is defined by $\pi/2 \leq \omega_1, \omega_2 \leq 2/3\pi$. The two triangles combined define the first of the twelve sectors of the bispectrum. As in the cumulant case, the knowledge of the bispectrum in one sector is sufficient to determine the other sectors using the above relations. Also, because of the skewness of symmetry regions, one should be careful when trying

31

to read the bispectral responses. Figure 2.4 shows a data arrangement in the bispectral plane where the solid lines represent the boundaries of the symmetry regions. Notice that the data is arranged parallel to these boundaries as indicated by the arrows (from side c to side b) in each of the six major symmetry regions. Each of these six symmetry regions has twofold symmetry along an axis S where $S \in \{\omega_2 = \omega_1, \omega_2 = -\omega_1, \omega_2 = -2\omega_1, \omega_2 = -\frac{1}{2}\omega_1\}$ (see Figure 2.4).

Due to the hexagonal shape of the bispectrum, it is a bit difficult to follow its periodicity in the ω_1, ω_2 plane every increment of 2π in each frequency axis. Figure 2.5 shows how the (ω_1, ω_2) plane is subdivided into hexagons of bispectra with period 2π.

Aliasing in the bispectral domain occurs in the triangle abf (see Figure 2.5) adjacent to the principle triangle oaf [50]. Notice that if a rectangular display of bispectral signatures is used then the responses in the triangles $\{abc, cgb, bgd, bde, bef, abf\}$ (see Figure 2.5) are all symmetric with different data arrangements. The reason for this symmetry is that the triangles $\{abc, abf\}$ belong to the first bispectral hexagon centered at $(0, 0)$, the triangles $\{cgb, bdg\}$ belong to the hexagon centered at $(2\pi, 0)$, and the triangles $\{bde, bef\}$ belong to the hexagon centered at $(0, 2\pi)$. The same symmetry is repeated in the third quadrant of the rectangular display of bispectral signatures. Estimates in these regions are unreliable because they may be due to an overlap of bispectral responses in the three adjacent bispectral hexagons.

An important property of the bispectrum is that it vanishes when $\{x(k)\}$ is a zero mean stationary Gaussian signal. Also, if the waveform $x(k)$ has a bispectrum $B(\omega_1, \omega_2)$, then the shifted signal $x(k-n)$ has the same bispectrum. Thus, the bispectrum as well as the spectral density are unaffected by a linear phase shift of the spectrum of $\{x(n)\}$. Further, if $e(k)$ is white

non-Gaussian noise defined such that $E\{e(k)\} = 0$, $E\{e(k)e(k + m)\} = \sigma^2$ and $E\{e(k)e(k + m)e(k + n)\} = \beta\delta(m, n)$. The bispectrum of $e(k)$ is constant over the (ω_1, ω_2) plane with magnitude β.

In many practical situations, the waveform $\{x(k)\}$ is bandlimited where $X(\omega)$ is defined over the frequency interval $[\omega_L, \omega_H]$. The bispectrum of $x(k)$, $B^x(\omega_1, \omega_2)$ is then nonzero only in the triangle $\omega_L \leq \omega_1, \omega_2 \leq \omega_H$, $\omega_1 + \omega_2 \leq \omega_H$ [49]. Figure 2.7, shows the bispectrum of a bandlimited signal.

2.3.3 The Bispectrum of Complex-Valued Signals:

The above definitions and properties of the bispectrum are limited to real-valued signals. Little information can be found on extensions of these definitions to complex-valued signals [76,43,44]. However, for the radar signal processing problem, the bispectrum of complex signals is needed. Below we discuss definitions and properties of the bispectrum of complex-valued signals.

If the data $\{x(k)\}$ is a complex stationary process, then the second order cumulant is defined as $C_2(m) = E\{x^*(k)x(k + m)\}$. It is also possible to alternate the conjugate so that $C_2(m) = E\{x(k)x^*(k + m)\}$. For the third joint cumulant case, the conjugate can be placed either on one or two entries of the triple product in (2.30). Only one In fact, placing the conjugate in a particular position defines which one of the six symmetry relations given in (2.48) remains valid. In general, the bispectrum of complex signals has twofold symmetry about an axis S such that $S \in \{\omega_1 = \omega_2, \quad \omega_2 = -\frac{1}{2}\omega_1, \quad \omega_1 = -\frac{1}{2}\omega_2, \quad \omega_1 = -\omega_2\}$. Figure 2.6 shows the configuration of the bispectral response with respect to its symmetry axis for all possible positions of the complex conjugate in the cumulant (as designated in each symmetry region in Figure 2.6). If the first quadrant $\omega_1, \omega_2 > 0$ is preferred then the third order cumulant is defined as

33
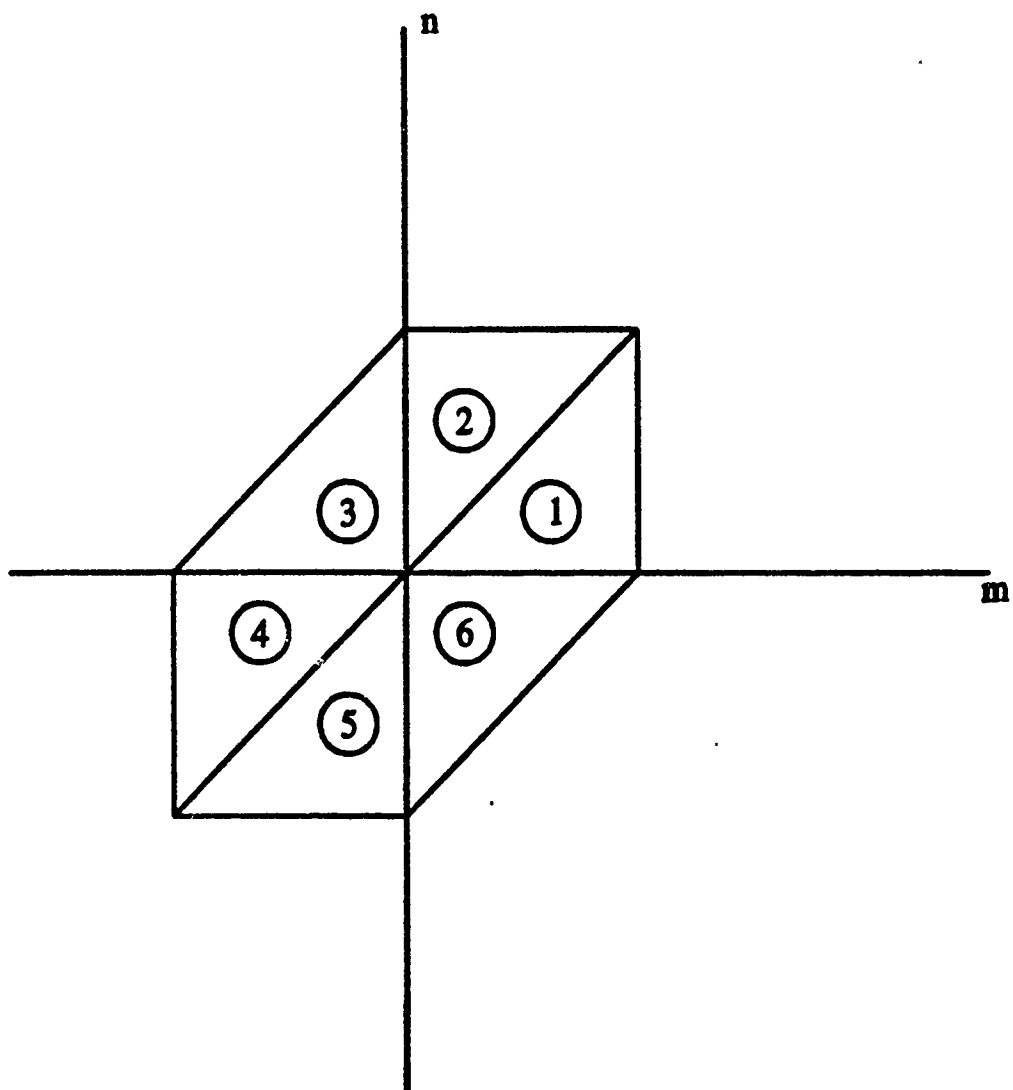
Figure 2.1: The six symmetry regions of the third order cumulant function $c(m,n)$
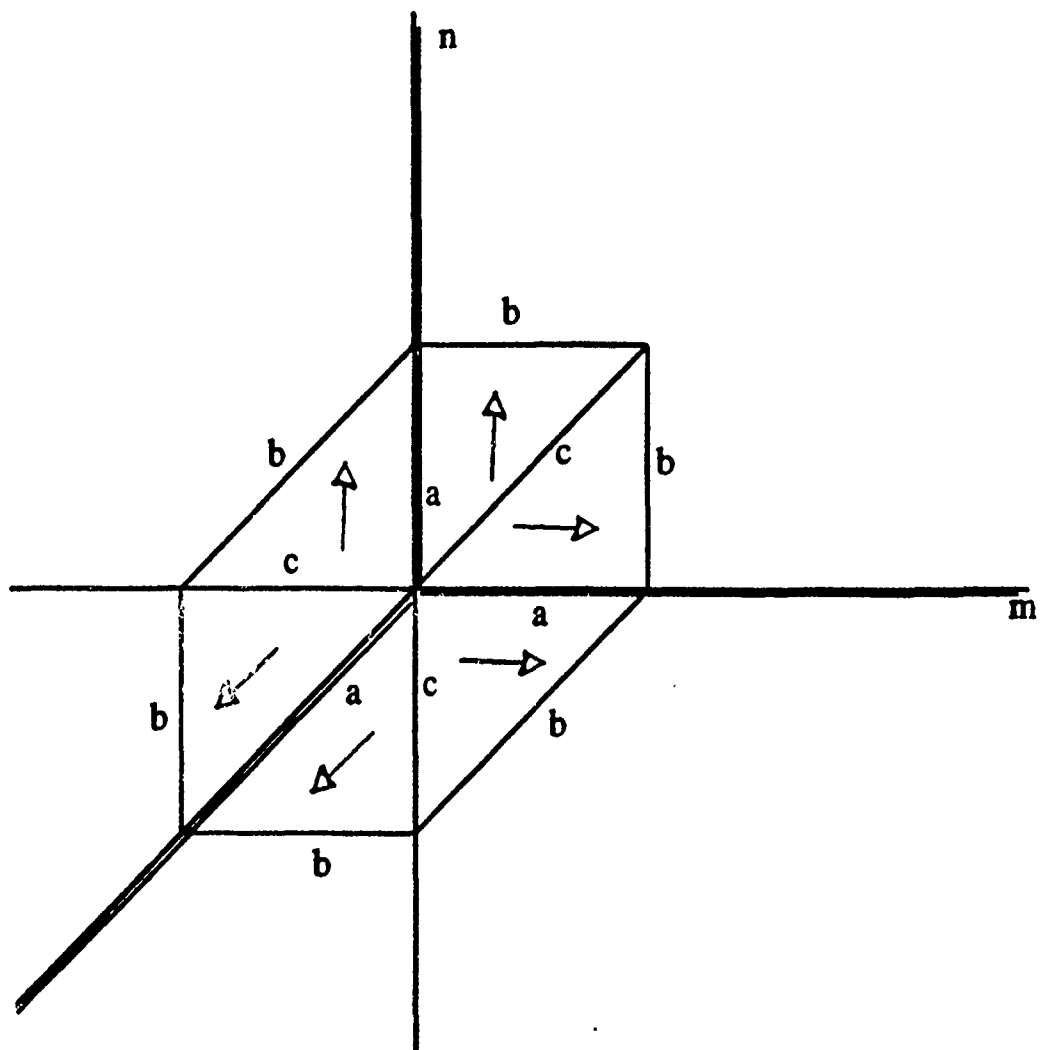
Figure 2.2: Data arrangement of third order cumulants.
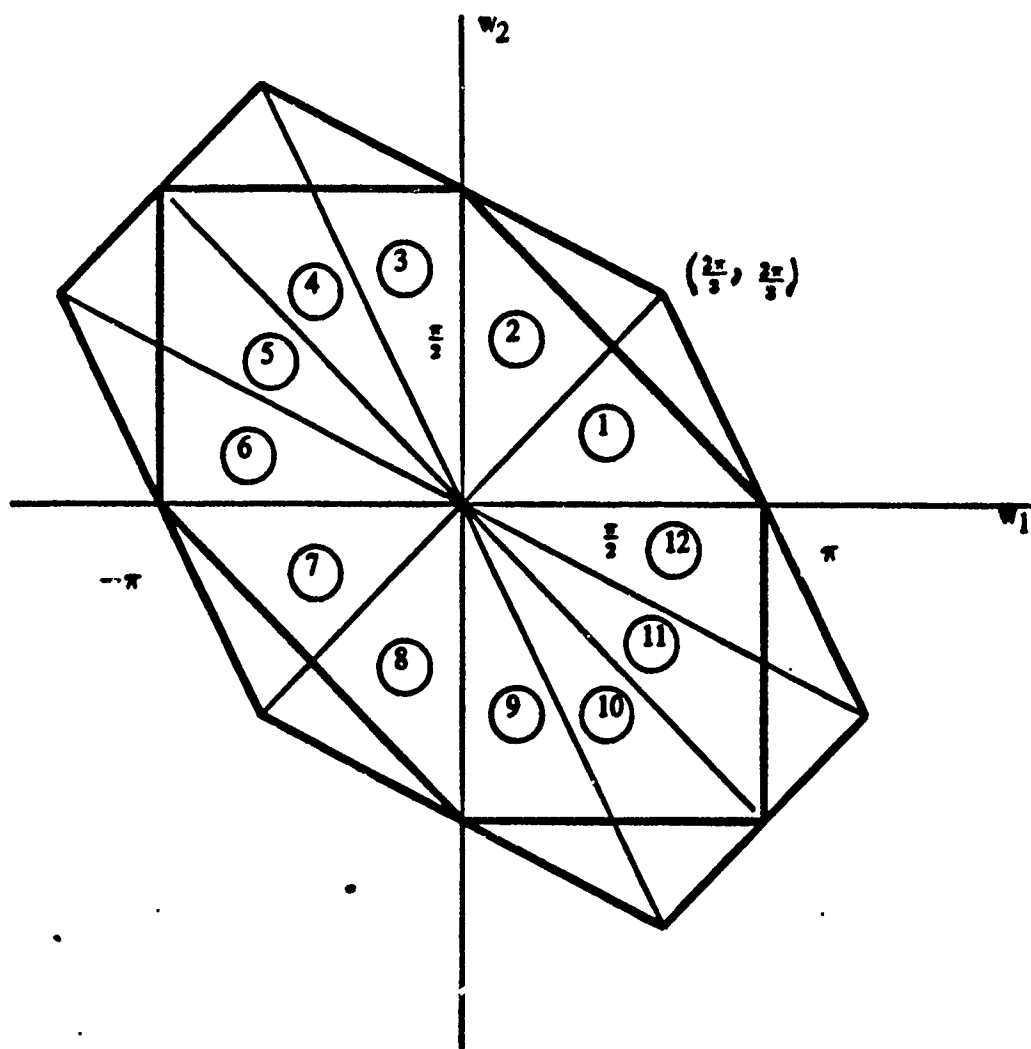
Figure 2.3: The twelve symmetry regions of the bispectrum $B(\omega_1, \omega_2)$
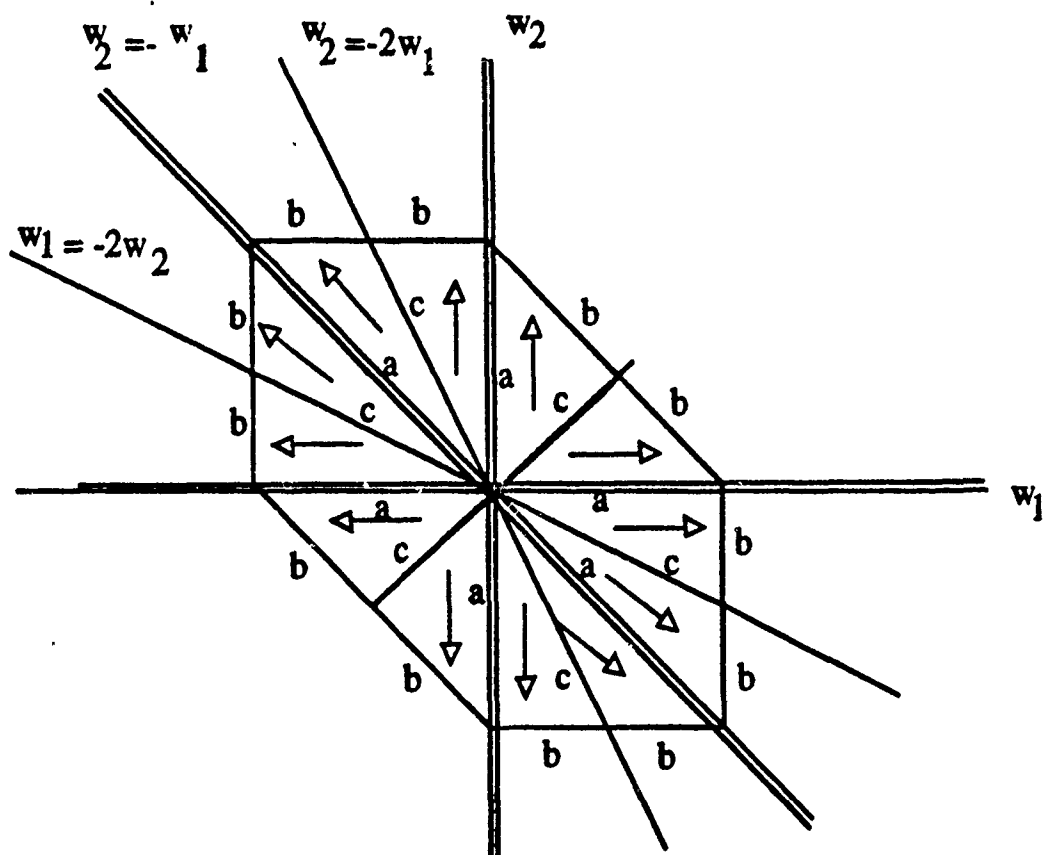
Figure 2.4: Data arrangement of the bispectrum.
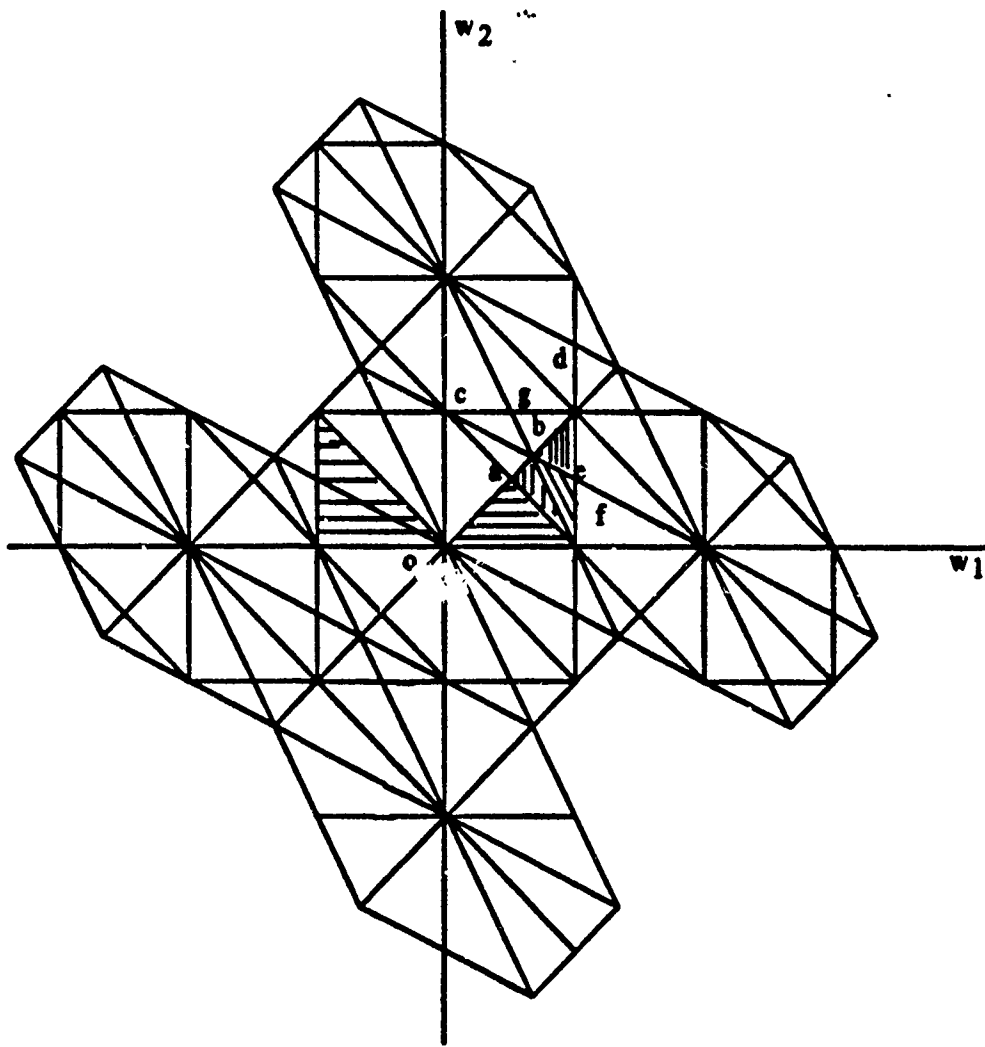
Figure 2.5: Periodicity of the bispectrum in the (ω_1, ω_2) plane.
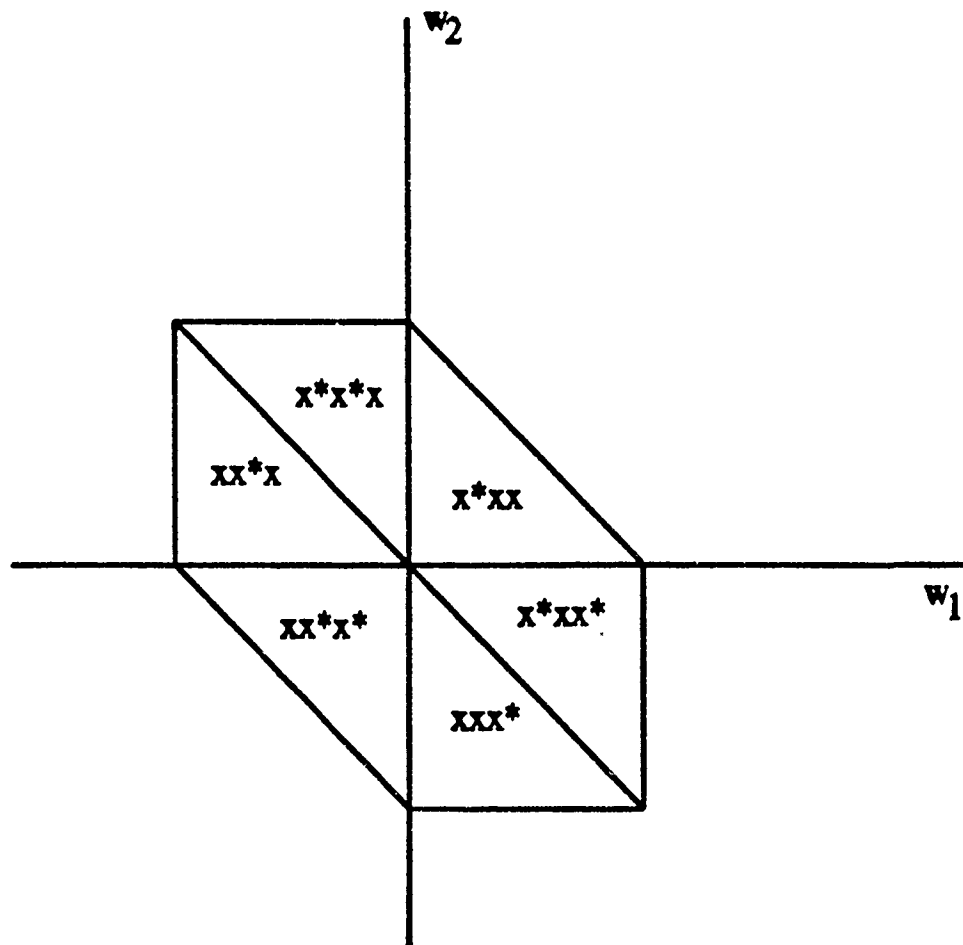
Figure 2.6: Distribution of the responses in the bispectral domain dependent on the placement of the conjugates in the third order cumulants

$$C_3(m,n) = E\{x^*(k)x(k+m)x(k+n)\}.$$

The following relations define the bispectrum of complex-valued signals for all possible positions of the complex conjugate.

$$E\{x^*(k)x(k+m)x(k+n)\} \xleftrightarrow{\mathcal{F}} \langle X(\omega_1)X(\omega_2)X^*(\omega_1+\omega_2)\rangle$$

with the symmetry relation $\quad\quad B(\omega_1,\omega_2) = B(\omega_2,\omega_1)$

$$E\{x(k)x^*(k+m)x(k+n)\} \xleftrightarrow{\mathcal{F}} \langle X^*(-\omega_1)X(\omega_2)X(-\omega_1-\omega_2)\rangle$$

with the symmetry relation $\quad\quad B(\omega_1,\omega_2) = B(\omega_1,-\omega_1-\omega_2)$

$$E\{x(k)x(k+m)x^*(k+n)\} \xleftrightarrow{\mathcal{F}} \langle X(\omega_1)X^*(-\omega_2)X(-\omega_1-\omega_2)\rangle$$

with the symmetry relation $\quad\quad B(\omega_1,\omega_2) = B(-\omega_1-\omega_2,\omega_2)$

$$E\{x(k)x^*(k+m)x^*(k+n)\} \xleftrightarrow{\mathcal{F}} \langle X^*(-\omega_1)X^*(-\omega_2)X(-\omega_1-\omega_2)\rangle$$

with the symmetry relation $\quad\quad B(\omega_1,\omega_2) = B(\omega_2,\omega_1)$

$$E\{x^*(k)x^*(k+m)x(k+n)\} \xleftrightarrow{\mathcal{F}} \langle X^*(-\omega_1)X(\omega_2)X^*(\omega_1+\omega_2)\rangle$$

with the symmetry relation $\quad\quad B(\omega_1,\omega_2) = B(-\omega_2-\omega_1,\omega_2)$

$$E\{x^*(k)x(k+m)x^*(k+n)\} \xleftrightarrow{\mathcal{F}} \langle X(\omega_1)X^*(-\omega_2)X^*(\omega_1+\omega_2)\rangle$$

with the symmetry relation $\quad\quad B(\omega_1,\omega_2) = B(\omega_1,-\omega_1-\omega_2)$

The symmetry properties for each position of the complex conjugate can be easily derived from the above equations. Note that it is possible to obtain one bispectral response from other bispectral responses using cumulant transformations. For example if $R_1(m,n) = E\{x^*(k)x(k+m)x(k+n)\}$ and $R_2(m,n) = E\{x(k)x^*(k+m)x(k+n)\}$ then $R_1(m,n) = R_2(-m,n-m)$. Similarly, if $R_3(m,n) = E\{x(k)x(k+m)x^*(k+n)\}$ then $R_1(m,n) = R_3(m-n,-n)$, and $R_1(m,n) = R_4^*(-m,n-m)$ where $R_4(m,n) = E\{x(k)x^*(k+m)x^*(k+n)\}$. Other relations can be obtained similarly.
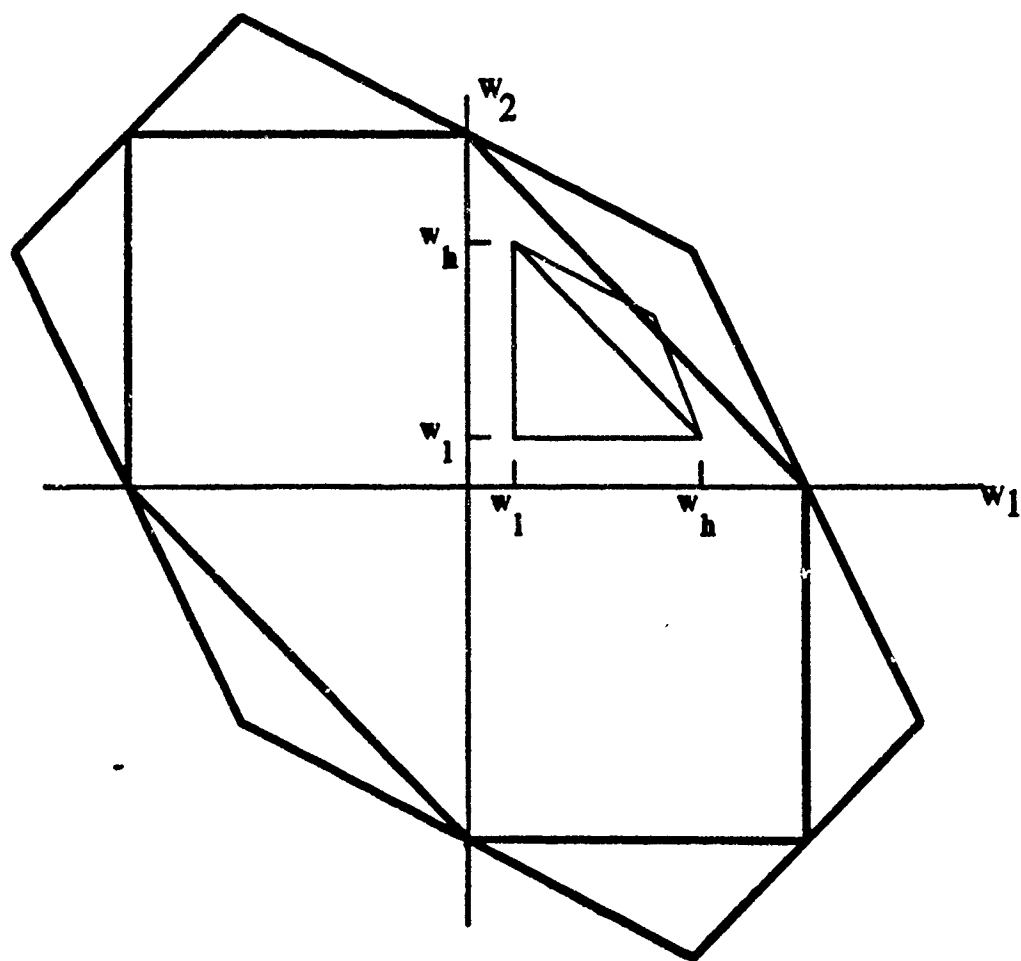
Figure 2.7: Bispectrum of bandlimited signals

2.3.4   Examples of Interpretation of The Bispectrum

Some of the properties of the bispectrum are better understood in the light of the following examples. For this reason, the following examples are common in the bispectrum literature [11,48], and are mentioned here because of their relevance to bispectral processing of radar signals.

Example 1 [11]: Quadratic phase coupling of two harmonic components of a random process due to quadratic nonlinearities. The signal

$$x(k) = \cos(\theta_1 k + \phi_1) + \cos(\theta_2 k + \phi_2) + \cos((\theta_1 + \theta_2)k + \phi_1 + \phi_2) \quad (2.50)$$

where ϕ_1 and ϕ_2 are random variables, uniformly distributed over $[0, 2\pi]$. The bispectrum of $x(k)$ is a single impulse at (θ_1, θ_2),

$$B^x(\omega_1, \omega_2) = \frac{1}{8}\delta(\omega_1 - \theta_1, \omega_2 - \theta_2) \quad (2.51)$$

This example demonstrates that the bispectrum is useful in detecting quadratic phase coupling between harmonic components [11].

Example 2 [48]: If $\{x(k)\}$ is a zero mean non-Gaussian stationary random process which is the input into a linear filter (with impulse response $h(k)$) then the bispectrum of the output signal $y(k)$ is given as

$$B^y(\omega_1, \omega_2) = B^x(\omega_1, \omega_2)H(\omega_1)H(\omega_2)H^*(\omega_1 + \omega_2) \quad (2.52)$$

The special case, where $x(k)$ is white non-Gaussian ($B^x(\omega_1, \omega_2) = 1$), is useful for parametric estimation of the bispectrum [42], where the bispectrum of the filter output is simply $H(\omega_1)H(\omega_2)H^*(\omega_1 + \omega_2)$.

Example 3 [11]: Let

$$y(k) = x(k) + ax^2(k) \quad (2.53)$$

where $x(k)$ is a zero mean stationary Gaussian random process. Then

$$B^y(\omega_1, \omega_2) = 2a\{S^x(\omega_1)S^x(\omega_2) + S^x(\omega_2)S^x(\omega_1, \omega_2)\} \quad (2.54)$$

$$+ar(0)\{S^x(\omega_1)\delta(\omega_2) + S^x(\omega_2)\delta(\omega_1)$$

$$+S^x(\omega_2)\delta(\omega_1, \omega_2)\} + o(a^3) \quad (2.55)$$

42

where $S^x(\omega)$ is the power spectral density. This example shows the role of the bispectrum in analyzing nonlinear systems. Exploring the relation between the bispectrum and the spectrum of $y(k)$ may indicate the type of nonlinearity applied to the process $x(k)$, particularly for $a < 1$.

The above examples are basic examples of the major applications of the bispectrum in signal processing. Additional examples can be found in [11,12,42,48]. An extensive study on the analysis of bilinear systems using bispectra can be found in [14,48].

2.3.5   Bispectral Estimation Techniques

The problem addressed in this section is the estimation of the bispectrum of the finite complex-valued data sequence $x(1), x(2), \ldots, x(N)$. As in the spectral estimation case, the notion of expectation if $x(k)$ is random and the notion of infinite summation if $x(k)$ is deterministic can be replaced by finite summation over the available data record weighted by the factor $1/N$. The expectation of the triple product can be replaced by segmenting the data records and then averaging the triple correlations of all segments. Segmentation also minimizes the estimate variance, thus improving the stability of the bispectral estimates.

The following techniques produce approximate estimates of the bispectrum and the true bispectral response is obtained only if the data record is of infinite length ($N \rightarrow \infty$). The estimation techniques given below are classical Fourier based bispectral estimation procedures and can be implemented using the fast Fourier transform. There are several parametric estimation techniques that are based on modeling the data as an AR or ARMA process [11,14,27,28,32].

43

Indirect method

The indirect bispectral estimation method [11] can be outlined as follows,
(this method is given in [11])

1) Segment the data into K records of M samples each.

2) Subtract the average value of each record (to get a zero mean record).

3) Estimate the third moment for each segment $r^{(i)}(m,n)$, $i = 1, \ldots, k$ by:

$$r^{(i)} = (N\Delta t)^2 \frac{1}{M} \sum_{l=s_1}^{l=s_2} x^{(i)^*}(l)x^{(i)}(l+m)x^{(i)}(l+n) \qquad (2.56)$$

where $s_1 = \max(0, -m, -n)$, $s_2 = \min\{M-1, M-1-m, M-1-n\}$,
and Δt is the sampling interval.

4) Average $r^{(i)}(m,n)$ over all segments

$$\hat{R}(m,n) = \frac{1}{k} \sum_{i=1}^{k} r^{(i)}(m,n) \qquad (2.57)$$

5) The bispectrum is computed using two-dimensional discrete Fourier
transform (2DFT) of $\hat{R}(m,n)$.

$$\hat{B}(\omega_1, \omega_2) = \sum_{m=-L}^{m=L} \sum_{n=-L}^{n=L} \hat{R}(m,n)W(m,n) \exp\{-j(\omega_1 m + \omega_2 n)\} \qquad (2.58)$$

where $L < M-1$ is the triple correlation lag and $W(m,n)$ is a two-
dimensional window function that can be generated from a one dimensional
window $d(m)$ as follows

$$W(m,n) = d(m)d(n)d(n-m) \qquad (2.59)$$

where $d(m) = d(-m)$, $d(0) = 1$, and $D(\omega) > 0$ $\forall \omega$. There are several
choices of $d(m)$, [11,14]. One popular choice is the Optimum Bias Supre-
mum window [11] defined as

$$d(m) = \frac{1}{\pi}\left|\sin\frac{\pi m}{L}\right| + \left(1 - \frac{|m|}{L}\right)\left(\cos\frac{\pi m}{L}\right), \quad |m| \leq L. \qquad (2.60)$$

Figure 2.8 shows the two-dimensional optimum bias supremum window function in frequency and time domains. An impulse in the bispectrum before windowing is convolved with the frequency response of the window, thus producing an elliptically spread response. The window design criterion is similar to the one dimensional case [11] but has to satisfy the symmetry properties of third order cumulants.

The above method is similar to the Correlogram spectral estimation method with the slight difference that we do not have to worry about nonnegativity of the estimate. Van Ness [35], has shown that if the 12th moment of the sequence $\{x(k)\}$, $E\{|x(k)|^{12}\}$ is finite, and all cumulants of order less than or equal to six are also defined, then the estimates of the bispectrum using the indirect method are asymptotically ($N \to \infty$) complex normal.

Direct method

The direct method [11] is based on the definition of the bispectrum as the ensemble average of the product $X(\omega_1)X(\omega_2)X^*(\omega_1 + \omega_2)$, and does not require using the two-dimensional FFT. Further, bispectral estimation as given below is similar to the periodogram spectral estimation method. The direct method consists of the following steps (this method is outlined in [11]):

1) Segment the data into K records of M samples each.

2) Subtract the average of each record.

3) Generate the DFT of all K records

$$X(\lambda) = \frac{1}{M} \sum_{k=0}^{M-1} x(k) \exp\left\{-j2\pi k\lambda/M\right\}$$
(2.61)

45
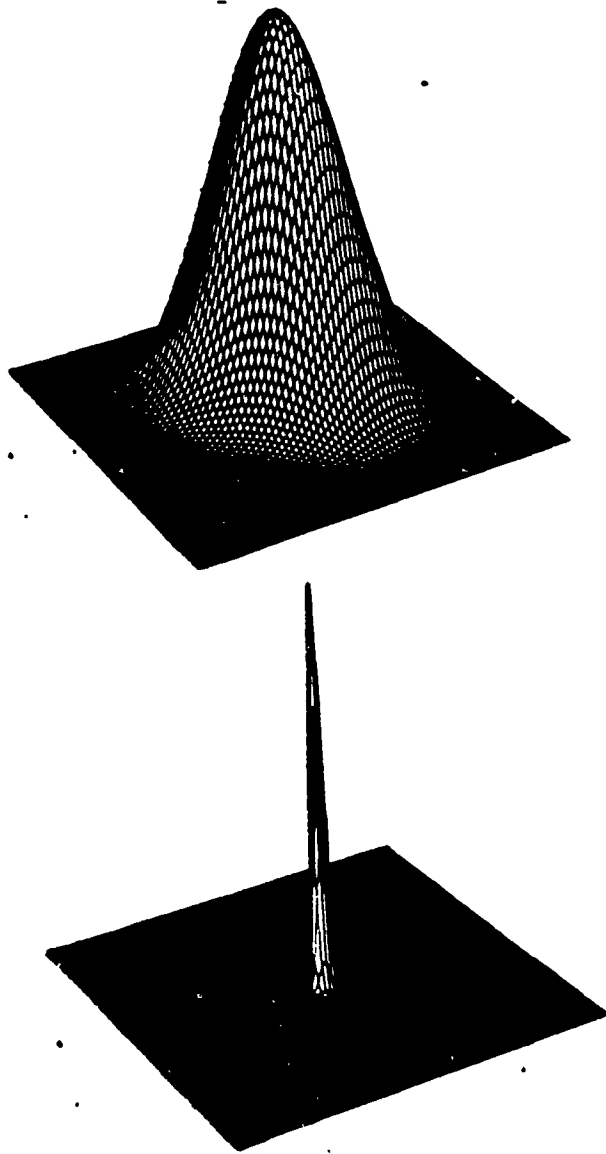
Figure 2.8: The two-dimensional window (2.59), (2.60) in the time (top) and the frequency domain (bottom)

46

4) Let $M = M_1 \times N$ and $M_1 = 2L_1 + 1$. Also, assume that the time increment between samples is Δt. Estimate the bispectrum of each segment using

$$b^{(i)}(\lambda_1, \lambda_2) = (N\Delta t)^2 \sum_{k_1=-L_1}^{L_1} \sum_{k_2=-L_1}^{L_1} Y^{(i)}(\lambda_1 + k_1) \qquad (2.62)$$
$$Y^{(i)}(\lambda_2 + k_2) Y^{(i)^*}(\lambda_1 + \lambda_2 + k_1 + k_2)$$

5) The bispectrum estimate of $x(k)$ is then given as

$$\hat{B}^x(\omega_1, \omega_2) = \frac{1}{k} \sum_{i=1}^{k} b^{(i)}(\omega_1, \omega_2) \qquad (2.63)$$

where $\omega_1 = \left(\frac{2\pi}{N\Delta t}\right) \lambda_1$ and $\omega_2 = \left(\frac{2\pi}{N\Delta t}\right) \lambda_2$.

Both direct and indirect bispectral estimation methods have high variance and therefore need a large number of data samples. The estimates can be made smoother if more segments are used but this will decrease the resolution of the bispectral estimates as a result of introduced nonstationarity problems [11]. In general, however, the above methods are easy to implement using FFT algorithms.

Other Methods

There are other more elaborate methods for estimating the bispectrum. Hinich [48] proposed another periodigram bispectral estimation technique. His technique is similar to the direct method with slight modification. Hinich's estimation method is generally useful for avoiding aliasing in the triangle adjacent to the principle triangle although oversampling is another way to avoid the aliasing problem. Statistical properties of the Hinich algorithm can be found in [36,50].

Thompson, [63], used a multiwindow bispectral estimation method where the information in a narrow band is summarized by the coefficients of its expansion in Slepian (discrete prolate spheroidal) sequences. The bispectrum estimates are then computed by averaging over time or over a three

47

dimensional element in the frequency domain. Details of this method can be found in [63]. In general, this method is computationally more demanding than the above methods. Thompson [63] claims that frequency domain averaging over a three dimensional element is less sensitive to nonstationarity in the data than the conventional methods. The bispectral estimates derived using Thompson's multiwindow techniques are consistent, unlike the direct method discussed above [63], where consistency means that both the variance and the bias of estimate approach zero as the number of data points increases [60]. It is shown in [12] that the bias in the estimates obtained using the direct method does not approach zero as $N \to \infty$.

Chapter 3

THE BIRANGE PROFILE OF RADAR SIGNATURES

3.1 Introduction

The focus in this chapter is on interpreting and understanding the bispectral features of radar targets. The goal is to provide an appropriate interpretation of the bispectrum of radar signatures, and to identify the advantages and disadvantages of this type of radar signal processing. To this end, we first investigate the role of the bispectrum in achieving a better understanding of the scattering mechanisms of radar targets. Secondly, we extract features that characterize the illuminated target. An investigation of the role of the bispectrum in identifying radar targets is presented in Chapter V.

The type of signal processing addressed in this study is based on a specified target scattering model. The model is that of equation (2.10), where the scattered signal is a combination of specular scattering terms from localized areas on the target and multiple interactions terms. The scattering region of interest is the resonance region (in which the target size is on the order of a wavelength). The bispectral signatures of measured (or computed) scattering coefficients in the optical region are also examined.

The purpose of bispectral analysis of radar signals is to add to the

49

knowledge that the transient response already offers. It is important to emphasize that the bispectrum is not an alternative to conventional radar signal processing (i.e., estimating the impulse response) but an addition that may be useful depending on the prevailing circumstances such as data conditions, noise statistics, and scattering region.

It is known that the scattering mechanisms of complex structures such as airplanes and ships are far more complicated than what can be deduced from the target transient response. The bispectral responses of such complicated targets are also difficult to analyze. For this reason, it is constructive to first consider synthesized targets and simple objects. Thus, the bispectra of a synthesized target, a simple generic aircraft model and a tilted flat plate are first examined. The bispectral responses of aircraft models are also investigated.

Bispectral analysis of radar signatures, as implemented in this study, has two major applications: 1) identification of multiple interactions, and 2) partial noise suppression. This chapter is primarily concerned with the interpretations of target bispectra in terms of modeled scattering mechanisms where the model in (2.10) serves as a basis for the interpretation. The effect of additive noise on the bispectral response of radar signatures is also investigated.

3.2   The Birange Profile: Definition and Properties

Target scattering features are more intuitive using time-domain signatures [2] than using frequency domain responses. Further, the transient response is an important representation of time-domain radar signatures. However, it is often difficult to deduce accurate information about the target shape using only the transient response because of the presence of multiple in-

50

teractions. In the following, the definition of the bispectrum in a radar signature analysis framework is given. The bispectrum of radar signals, as defined in this Chapter, can be used as a tool for discriminating between multiple interactions and specular scattering.

In most signal processing problems, the data sequence consists of samples taken from a time-dependent waveform. Then the bispectrum, as defined in Chapter II, is a function of two variables ω_1 and ω_2 in the frequency domain. The radar scattering data sequence, however, is not a time series but recorded in the frequency domain. The triple correlation of the frequency domain data is a two-dimensional profile in the frequency domain and is defined as

$$R(\omega_1, \omega_2) = E\{H^*(\omega)H(\omega + \omega_1)H(\omega + \omega_2)\} \qquad (3.1)$$

The bispectrum is then given as

$$B(t_1, t_2) = \sum_{\omega_1 = -\infty}^{\infty} \sum_{\omega_2 = -\infty}^{\infty} R(\omega_1, \omega_2) \exp\left\{-j(\omega_1 t_1 + \omega_2 t_2)\right\} \qquad (3.2)$$

Therefore, the bispectrum is a profile of target scattering signatures in the two-dimensional time domain and can be termed the "bi-time" profile of radar targets. Further, the bispectrum can be expressed as a two-dimensional profile in the range domain using the relation

$$t = \frac{2r}{c} \qquad (3.3)$$

where r is the range from the radar to the target, t is the time needed for the signal to propagate to the target and back, and c is the speed of light. Therefore, the bispectrum as a function of range is given as

$$B(r_1, r_2) = \sum_{f_1} \sum_{f_2} R(f_1, f_2) \exp\left\{-j4\pi/c(f_1 r_1 + f_2 r_2)\right\} \qquad (3.4)$$

where $f_i = \omega_i/2\pi$. This representation of the bispectrum corresponds to a birange profile of the target. Hence, the *birange profile* is a bispectral

51

display of target signatures in the two-dimensional range domain r_1 and r_2 where the term "range" denotes the propagation distance along the target.

The birange profile of complex radar signals satisfies only one symmetry property defined as

$$B(r_1, r_2) = B(r_2, r_1). \qquad (3.5)$$

The definition of the birange is more insightful when expressed in terms of the impulse response as

$$B(r_1, r_2) = \langle h(r_1)h(r_2)h^*(r_1 + r_2) \rangle \qquad (3.6)$$

where $h(r)$ is the impulse response as a function of range and $\langle \rangle$ indicates the ensemble average. Defining the birange as such implies that a non-zero bispectral response is the result of interaction between the responses at r_1 and r_2 which appears as a response at $r_1 + r_2$. Furthermore, the bispectrum at (r_1, r_2) is non-zero only if the responses at r_1 and r_2 and $r_1 + r_2$ are correlated. Notice that the definition of the birange as given in (3.4) corresponds to the case where the triple correlation is computed using (3.1); i.e. the conjugate is placed on the first element of the triple product.

3.2.1   Estimation of The Birange Profile

The classical bispectrum estimation techniques, summarized in Chapter II and slightly modified, can be used to estimate the birange profile. The modifications are due to data conditions such as stationarity and data-length. Stationarity requires that the third order cumulant of the measured data be invariant with respect to the frequency band used. Also, having a finite set of data imposes some constraints on segmenting the data without reducing the resolution in the birange. The following bispectral estimation algorithm is used throughout this chapter.

The birange profile can be estimated using either the direct method or the indirect method (based on the triple correlation of the data). Estimates

of the birange profile in the experimental part of the study are computed using a slightly modified version of the indirect classical method. The algorithm used for birange estimation given a finite set of data $\{H(\omega)\}$, is outlined below:

1) Subtract the average value of the data. The purpose of this step is to have a zero mean signal, which is needed to achieve noise suppression.

2) Estimate the triple correlation

$$R(m,n) = \frac{1}{N} \sum_{l=s_1}^{s_2} H^*(l)H(l+m)H(l+n) \qquad (3.7)$$

where $s_1 = \max(0, -m, -n)$ and $s_2 = \min(N-1, N-1-m, N-1-n)$. The number of data points is denoted by N, and $-L \leq m, n \leq L$.

3) The birange is generated using

$$B(r_1, r_2) = \sum_{m=-L}^{L} \sum_{n=-L}^{L} R(m,n)W(m,n) \exp\{-j(\omega_1 m + \omega_2 n)\} \qquad (3.8)$$

where $W(m,n)$ is the window function defined in (2.62) and where L is the triple correlation lag (usually chosen to be $\approx N/5$). Because no data segmentation is employed, high variance birange profiles are obtained particularly for large values of L. The reason for avoiding segmentation is that the data may not be stationary (because target scattering features are dependent on the frequency band used) and segmentation introduces potential non-stationarities [11] and reduces the resolution of the bispectral estimates [60].

The assumption that the scattering data are stationary requires that the triple correlation is dependent only on the frequency increment, that is

$$E\{X^*(f_i)X(f_j)X(f_k)\} = E\{X^*(f)X(f+f_j-f_i)X(f+f_k-f_i)\} \quad \forall f \quad (3.9)$$

In radar scattering, this assumption is not valid over a wide frequency range. Therefore, the birange $B(r_1, r_2)$ is, in general, dependent on frequency. It is

53

possible, however, to assume that the birange does not change significantly over small frequency bands. Further, by avoiding data segmentation and large data bandwidths, it is possible to obtain an estimate of the birange profile which is approximately frequency independent.

The definition of the triple correlation as given in (3.1) requires that the measured data have zero mean in order to exclude second order moments from the definition of the third order cumulant. This constraint is particularly useful to ensure suppression of additive Gaussian noise. There is no guarantee, however, that this condition is satisfied. One can avoid this problem by simply removing the mean of the data. But, when the sample mean is removed from the data, the birange may erroneously indicate the presence of a response at time zero [60]. Furthermore, the scattering data may include transient signals and removal of sample mean is undesirable [60] in this situation. On the other hand, if the average is not subtracted from the data, then the third order cumulant differs from third order moment and will include the second order moment of the data sequence. Further, the addition of the second order moment to the cumulant introduces undesirable noise effects because the second moment of additive Gaussian noise is not zero (see details in Section 3.8). Thus, for the radar application the benefits of mean removal seem to outweigh the disadvantages.

3.3 Interpretation of The Bispectrum of Radar Signatures

An interpretation of the bispectrum of radar signatures based on an assumed scattering model is given in this section. The assumed model corresponds to scattering in the resonance region, and it is assumed the scattered signal is composed of two major components. The first component is due to specular direct scattering from localized positions on the target. The

scattered signal due to the first component is given as

$$H_1(\omega) = \sum_{p=1}^{m} A_p(\omega) \exp\left\{-j(\psi_p + \omega t_p)\right\} \qquad (3.10)$$

where m is the number of scattering centers and A_p is the amplitude of the scattered signal from the pth scattering center. The electric phase of the pth scatterer is denoted by ψ_p, and t_p is the propagation time between the radar and the pth scattering subcomponent and back. Notice that the inverse Fourier transform of the above returned signal is given by

$$h_1(t) = \sum_{p=1}^{m} A_p \exp\left\{-j\psi_p\right\}\delta(t - t_p) \qquad (3.11)$$

assuming that the amplitude A_p and phase ψ_p are independent of frequency. The impulse response $h_1(t)$ thus consists of m impulses displayed at times $t_p, \forall p = 1, \ldots, m$. Therefore, each peak in the impulse response is an indication of specular scattering at time t_p. If either the amplitude A_p or the phase ψ_p is a function of frequency then the corresponding peak may be displaced from t_p and may have nonzero width; this phenomenon is a characteristic of frequency dispersive scattering.

The second major component that contributes to target scattering is the effect of multiple interactions. This type of scattering occurs in several ways. The interactions may include multiple propagation between two or three scattering centers. Multiple interactions may also occur between scatterers that are not collinear with the radar axis. In general, there is no defined rule for multiple interactions in terms of direction or magnitude.

The multiple interactions can be modeled as

$$
\begin{aligned}
H_2(\omega) &= \sum_{p=1}^{m}\sum_{q=1}^{n} A_{pq}(\omega) \exp\left\{-j(\psi_p + \psi_q + \omega(t_p + t_q))\right\} \qquad (3.12) \\
&\quad + \sum_{p=1}^{m}\sum_{q=1}^{n} A'_{pq}(\omega) \exp\left\{-j(\psi_p + \psi_q + \omega t_{pq})\right\}
\end{aligned}
$$

where $A_{pq}(\omega), A'_{pq}(\omega)$ indicate the amount of coupling between the pth and q^{th} scattering points. The distinction between A_{pq} and A'_{pq} is needed because some interactions of magnitude A'_{pq} are not necessarily scattered at $t_p + t_q$. The inverse Fourier transform of $H_2(\omega)$ is given by

$$h_2(t) = \sum_{p=1}^{m} \sum_{q=1}^{m} \exp\left\{-j(\psi_p + \psi_q)\right\} \left(A_{pq}\delta(t - (t_p + t_q)) + A'_{pq}\delta(t - t_{pq})\right)$$

(3.13)

and consists of impulses at times $t_p + t_q$, and t_{pq} and $p, q = 1, \ldots, m$ assuming that A_{pq}, ψ_p, and ψ_q are independent of frequency. Furthermore, the relations between A_{pq} or A'_{pq} and the pair (A_p, A_q) are not usually known. Notice that while some interactions (indicated by multiple propagation of the transmitted radar signal between scatterers) are received by the radar at $t_p + t_q$, other types of interactions (mainly due to single propagation between scatterers) are received at time $t_{pq} \neq t_p + t_q$. Both forms of interactions are modeled in $H_2(\omega)$.

A scattering model which includes both specular and interaction terms is a combination of $H_1(\omega)$ and $H_2(\omega)$. Hence, the returned backscattered radar signal can be modeled as

$$H(\omega) = H_1(\omega) + H_2(\omega) \tag{3.14}$$

$$= \sum_{p=1}^{m} A_p(\omega) \exp\left\{-j(\psi_p + \omega t_p)\right\} \tag{3.15}$$

$$+ \sum_{p=1}^{m} \sum_{q=1}^{n} A_{pq}(\omega) \exp\left\{-j(\psi_p + \psi_q + \omega(t_p + t_q))\right\}$$

$$+ \sum_{p=1}^{m} \sum_{q=1}^{n} A'_{pq}(\omega) \exp\left\{-j(\psi_p + \psi_q + \omega t_{pq})\right\}$$

Based on the above model, which is more realistic than using $H_1(\omega)$ only, it is clear that conventional spectral analysis does not provide the necessary distinction between specular scattering and multiple interactions. Also, the Fourier transform or modern spectral estimation techniques of the radar backscatter data cannot identify the coupling between interacting

56

subcomponents. Using the definition of the bispectrum given in Section I of this Chapter, the bispectral response of a radar target whose backscattered signal satisfies (3.15) is

$$
\begin{aligned}
B(t_1, t_2) &= \langle h(t_1)h(t_2)h^*(t_1 + t_2) \rangle \qquad\qquad (3.16) \\
&= \sum_{p=1}^{m} \sum_{q=1}^{m} A_p A_q A_{pq} \{ \delta(t_1 - t_p, t_2 - t_q) + \delta(t_1 - t_q, t_2 - t_p) \}
\end{aligned}
$$

that is, the birange profile of $H(\omega)$ consists of impulses at the pairs (t_p, t_q), $p, q = 1, \ldots, m$ with magnitudes $A_p A_q A_{p+q}$. Hence, the bispectrum of radar signals will detect the interactions with A_{pq} terms, but will not detect interactions with A'_{pq} terms. In otherwords, the birange profile detects multiple interaction terms when the time delay is the sum of the two time delays of the pth and q^{th} specular scattering terms. Based on the above modeling of radar signatures, it is reasonable to say that peaks in the birange (or bispectrum) of radar signals are indications of multiple interactions between scattering subcomponents. Furthermore, these interactions occur between subcomponents whose distance to the radar is determined by the coordinates of the peaks in the birange.

The intuition behind the identification of these interactions is that the birange profile $B(r_1, r_2)$ (or bi-time $B(t_1, t_2)$) is related to the impulse response using the Cramer spectral representation (2.41) $B(t_1, t_2) \propto \langle h(t_1)h(t_2)h^*(t_1 + t_2) \rangle$. Therefore, the birange exhibits peaks at (t_i, t_j) when the impulse response has peaks at t_i, t_j, and $t_i + t_j$, and these peaks are correlated. There are two situations in which the impulse response may peak at these points simultaneously: 1) when a multiple interaction of the form given in (3.15) occurs, or 2) by coincidence when there are specular scattering components at all three time instants. A method for discriminating between these two possibilities is discussed in Section (3.3.3) below.

The above interpretation is valid for the interior regions of the birange but not for the responses at the axes. In fact the responses on the time (or

57

range) axes may not correspond to any interactions. The bitime profile on the time axes is given by

$$B(0, t_2) = B(t_1, 0) = \langle h(0)|h(t)|^2 \rangle \qquad (3.17)$$

Notice that the responses on the axes of the birange are proportional to the power spectral density of the target signatures. Therefore, the information provided by the bi-time profile is twofold: 1) multiple interactions are displayed in the internal region between the axes, and 2) the square of the magnitude of the impulse response is displayed along the time axes. If the birange is estimated using only the real component of the radar signal then the magnitude squared of the impulse response will be also displayed along the line $t_1 + t_2 = 0$.

The interpretation of the bispectrum of radar signatures as given above is clarified by the following two examples. The identification of multiple interactions of real radar targets using the bispectrum is also demonstrated using several examples of experimental radar scattering data.

3.3.1 Example 1: Synthesized Target

The first example consists of scattering from a hypothetical three point-scatterer hypothetical target. The purpose of this example is to present an intuitive interpretation of the role of the bispectrum in identifying multiple interactions as discussed in the previous section. For conceptual purposes only, the first two point-scatterers correspond to the leading and the trailing edges of a blade, and the third scatterer corresponds to the specular scattering mechanism from a sphere.

Consider, as shown in Figure 3.1, a blade of width $r_1 - r_0$ and a sphere at a distance $r_2 - r_1$ from the trailing edge of the blade. If one considers

58

only four ray paths, the backscattered signal (assuming $r_0 = 0$) is

$$\tilde{S}_t(f_j) = A_1 + A_2 \exp\left(-j4\pi r_1 \frac{f_j}{c}\right) + A_3 \exp\left(-j4\pi r_2 \frac{f_j}{c}\right)$$
$$+ A_4 \exp\left(-j4\pi(r_1 + r_2)\frac{f_j}{c}\right). \tag{3.18}$$

We have assumed that the amplitudes A_1, A_2, A_3, and A_4 (see Figure 3.1 for the values of A_1, A_2, A_3, and A_4) are frequency independent and that the sphere creeping wave terms are negligible.

The scattered signal from this target satisfies the complex exponential model of (3.15). The transient response of the blade and sphere target as computed using Fourier transform with a Hanning window over a frequency band from 1.5 GHz to 12 GHz is shown in Figure 3.2. Note the one to one correspondence of the first three responses with the geometry of the target. The fourth response, however, is an interaction term and does not correspond to any target components. The birange of the above signal in the first symmetry region (defined by $t_1, t_2 > 0, t_1 + t_2 = 1/2\Delta f$ where Δf is the sampling period) is

$$B_{S_t}(R_1, R_2) = \frac{1}{8}\{A_1^3 \delta(R_1, R_2) + A_1 A_2^2 \delta(R_1 - r_1, R_2) \tag{3.19}$$
$$+ A_1 A_3^2 \delta(R_1 - r_2, R_2) + A_1 A_4^2 \delta(R_1 - (r_1 + r_2), R_2)$$
$$+ A_2 A_3 A_4 \delta(R_1 - r_2, R_2 - r_1)\}.$$

Figure 3.2 shows this birange profile (with no windowing). Notice the response at $(t_1, t_2) = (1.6, 2.4)$ meters which is due to interaction between the trailing edge of the blade and the sphere and is represented by the term $\exp\left(-j4\pi(r_1 + r_2 - r_0)\frac{f_j}{c}\right)$. Further, the response on the range axes $r_1 = 0$, $r_2 = 0$ and also along the line $r_1 + r_2 = 0$ is proportional to the magnitude squared of the transient response. Therefore, the birange of the blade-sphere target includes information about multiple interactions at (r_1, r_2) as well as the magnitude squared of the transient response.

Tapering the triple correlation function of the frequency response using a two dimensional-window (to avoid Gibbs sidelobe phenomenon) [14] results in the bispectral response shown in Figure 3.3. The window function used is the Minimum Bias Supremum given in [11]. Note that each impulse in the original bispectrum is spread into an ellipse corresponding to the contour of the window response in the time domain [14].

3.3.2   Example 2: Thin-Blade & Sphere Target

The scattering model in this case is similar to the previous example. The width of the blade $r_1 - r_0$, (or the distance between the first two point-scatterers), is reduced such that

$$r_1 - r_0 < \frac{c}{2(f_h - f_l)} \tag{3.20}$$

where $f_h - f_l = B$ which is the measurement bandwidth. The resolution Δt of the transient response when estimated using Fourier transform techniques is

$$\Delta t = \frac{1}{B} \tag{3.21}$$

which is equivalent to range resolution

$$\delta r = \frac{c}{2B} \tag{3.22}$$

Therefore, due to this choice of blade width, the first two peaks of the transient response cannot be separated by Fourier processing because of resolution limitations. The transient response and the birange of this target are shown in Figure 3.4. The first peak in the transient response corresponds to a superposition of direct scattering from both leading and trailing edges of the thin blade. The second peak corresponds to a superposition of direct scattering from the sphere and the interaction term. Thus, due to the limited resolution of the transient response, we are unable to detect the two edges of the blade or the interaction term.

ZERO REFERENCE

x_0
x_1
x_2

100%
$\tilde{S}_1$ 10%
90%
45%
45%
23% 22% 45%
$\tilde{S}_2$
11%
11% 11%
$\tilde{S}_3$
11%
$\tilde{S}_4$

$$\tilde{S}_1 = \lambda_1 e^{-jk2x_0}$$

$$\tilde{S}_2 = \lambda_2 e^{-jk2x_1}$$

$$\tilde{S}_3 = \lambda_3 e^{-jk2x_2}$$

$$\tilde{S}_4 = \lambda_4 e^{-jk[2(x_2+(x_1-x_0))]}$$

$$\tilde{S}_r = \tilde{S}_1 + \tilde{S}_2 + \tilde{S}_3 + \tilde{S}_4$$

$\lambda_1 = 10$
$\lambda_2 = 23$
$\lambda_3 = 45$
$\lambda_4 = 11$
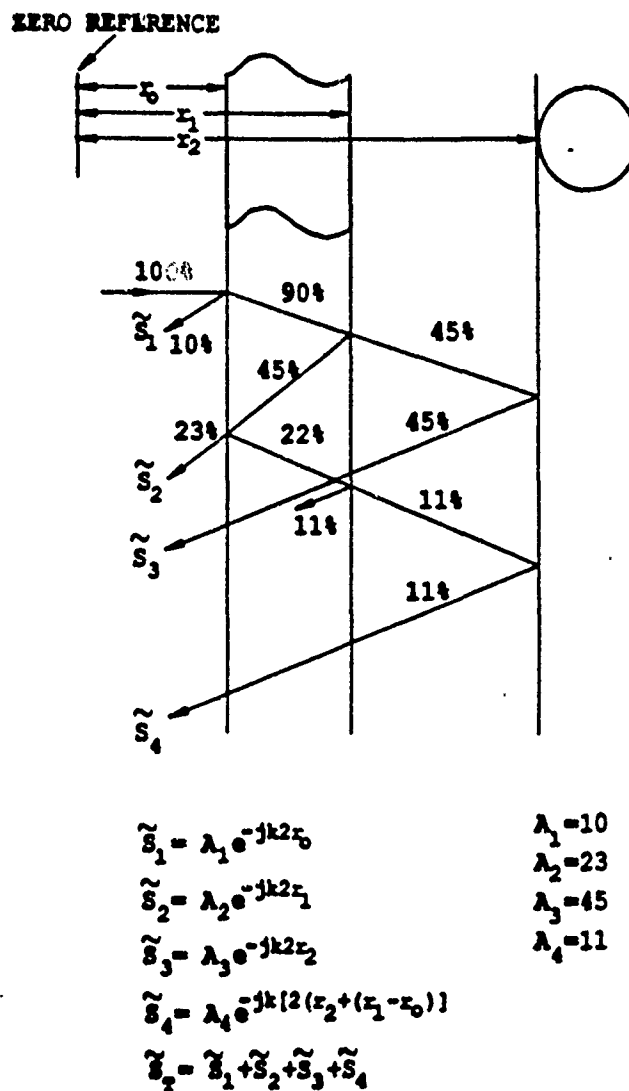
Figure 3.1: Internal bounce diagram for blade-sphere example

61
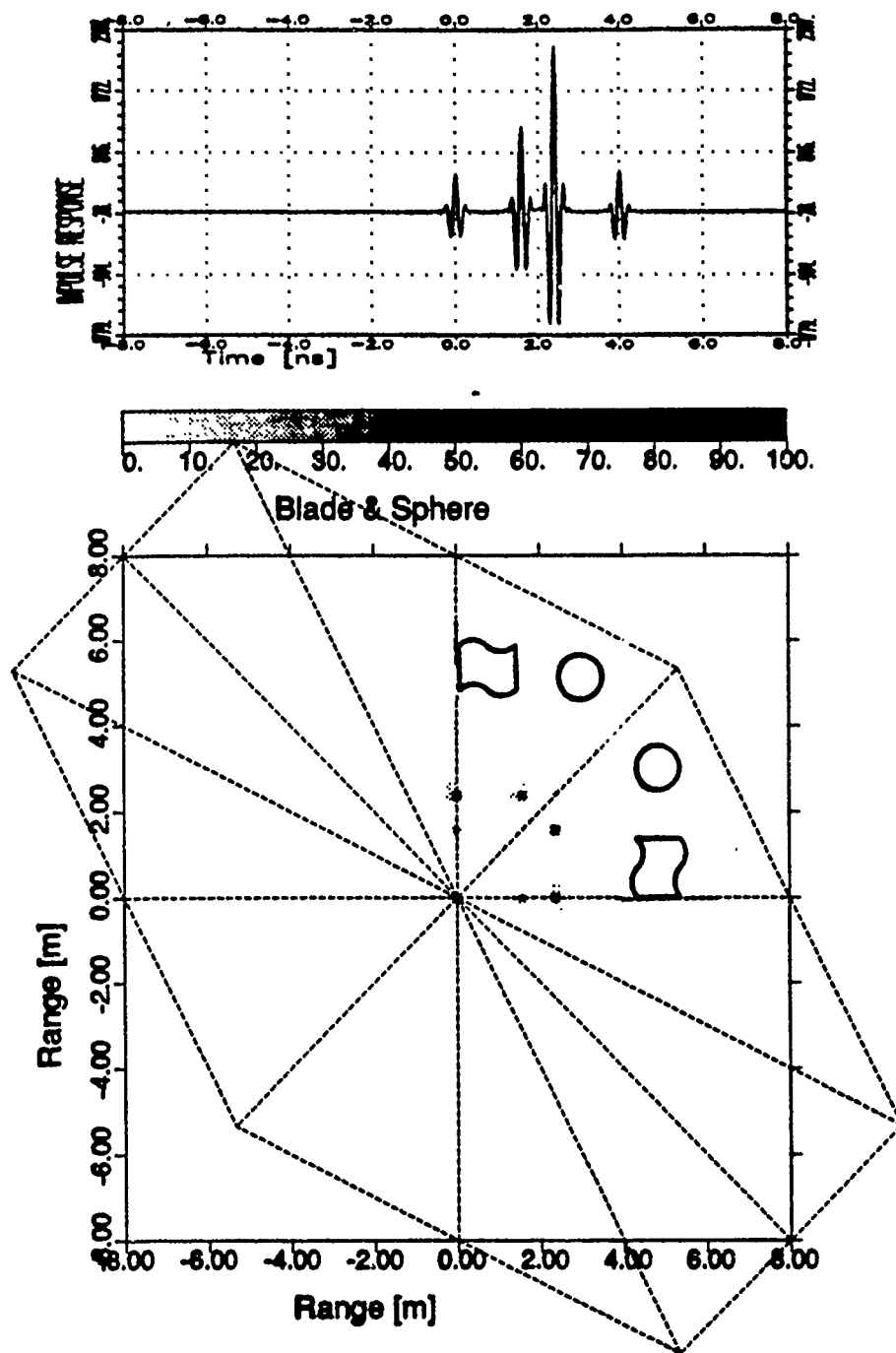
Figure 3.2: Transient response and birange profile of blade-sphere target

Now consider the birange profile of this target (see Figure 3.4). Notice that the birange exhibits a peak at (r_1, r_2) as an indication of multiple interaction. Also, notice that the magnitude square of the transient response is no longer displayed along the axes. The reason is that the magnitude of the birange at the range axis $B(0, r)$ or $B(r, 0)$ is proportional to the transient response at $t = 0$, and $h(0) = 0$.

Two conclusions can be drawn from this example: 1) the birange may detect interactions that may not be displayed in the impulse response, perhaps for resolution reasons, 2) the magnitude squared of the transient response is displayed along the range axes only if $h(0) \neq 0$ (if the data is segmented, then $h(0) \neq 0$ is not sufficient to obtain the spectral density along the axes of the birange). Hence, this example shows that neither the transient response nor the birange is sufficient to analyze scattering mechanisms. A combination of both techniques is the key to time-domain scattering analysis.

3.3.3 A Method for Detecting False Interactions

A peak at $r_1 + r_2$ in the transient response is possibly an indication of interactions between two scattering subcomponents at r_1 and r_2 along the target. An alternative scenario however, is that the peak at $r_1 + r_2$ is due to two components; one is specular which is coincidently located at $r_1 + r_2$ and the other is the result of multiple interaction between the scatterers at r_1 and r_2. The problem is, then, how to determine whether the response at $r_1 + r_2$ is specular, or is the result of an interaction, or is a combination of the two. This can be done by considering the bicoherence at the peak. The bicoherence at (r_1, r_2) is simply the birange at (r_1, r_2), normalized with

63
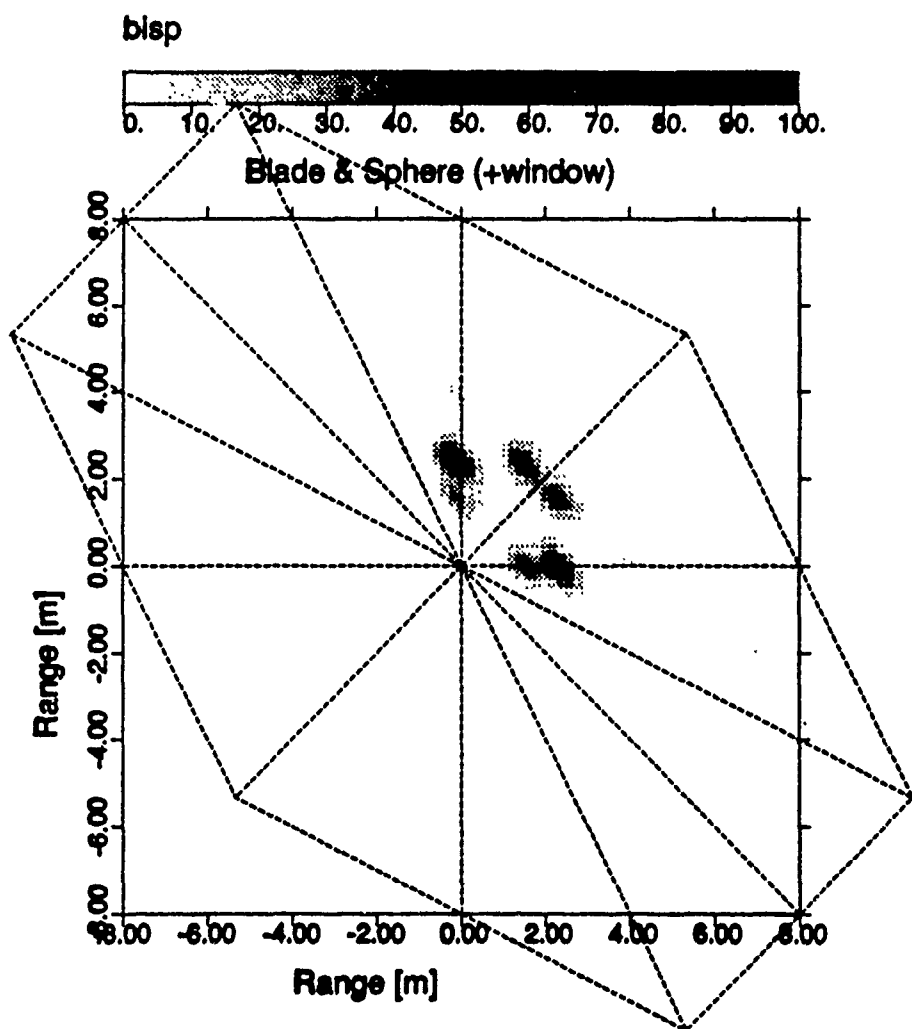
Figure 3.3: Birange profile of blade-sphere target (windowed triple correlation)
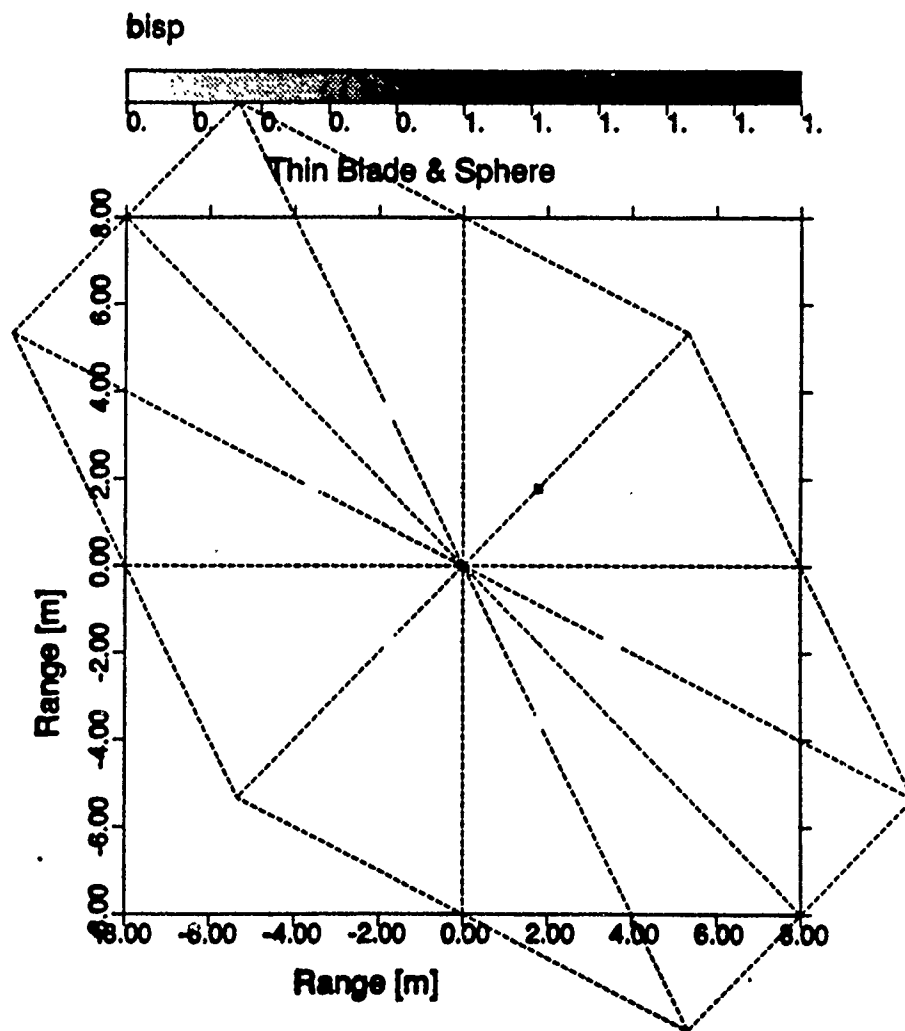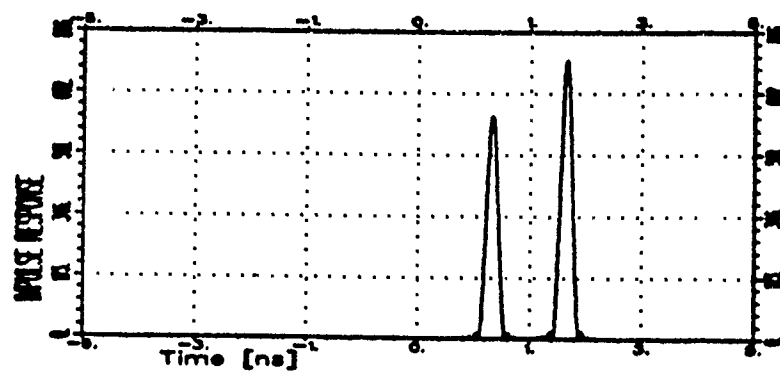
Figure 3.4: Transient response and birange profile of (thin blade)-sphere target

65

respect to the spectral density at r_1, r_2 and $r_1 + r_2$;

$$bic^H(r_1, r_2) = \frac{B^H(r_1, r_2)}{\sqrt{S^H(r_1) S^H(r_2) S^H(r_1 + r_2)}} \qquad (3.23)$$

where $S^H(r)$ is the spectral density of the target response $H(f)$ at r. If the bicoherence at (r_1, r_2) is equal to one, then the response at $r_1 + r_2$ is totally caused by an interaction. If the bicoherence is less than one, then the response at $r_1 + r_2$ is due to a partially correlated interaction, or due to both a multiple interaction and a specular scattering term. If the bicoherence is zero then there is no interaction at $r_1 + r_2$ and the response is due to specular scattering.

As an example, consider the specular scatterers at r_p, r_q and $r_p + r_q$. Assume that there is a multiple interaction between r_p and r_q that produces a response at $r_p + r_q$ in the transient response. Then, the frequency response is given as

$$
\begin{aligned}
H(\omega) \;=\; & A_p \exp\left\{-j2\frac{\omega}{c}(r_p) + \psi_p\right\} + A_q \exp\left\{-j2\frac{\omega}{c}(r_q) + \psi_q\right\} \\
& + A_{pq} \exp\left\{-j2\frac{\omega}{c}(r_p + r_q) + \psi_p + \psi_q\right\} \\
& + A_{p+q} \exp\left\{-j2\frac{\omega}{c}(r_p + r_q) + \psi_{p+q}\right\} \qquad (3.24)
\end{aligned}
$$

The bispectrum of $H(\omega)$ is then given as

$$B^H(r_1, r_2) = A_p A_q A_{pq} \left(\delta(r_1 - r_p, r_2 - r_q) + \delta(r_1 - r_q, r_2 - r_p)\right) \qquad (3.25)$$

and the spectral density of $H(f)$ is

$$
\begin{aligned}
S^H(r) \;=\; & A_p^2 \delta(r - r_p) + A_q^2 \delta(r - r_q) \\
& + (A_{pq}^2 + A_{p+q}^2) \delta(r - (r_p + r_q)) \qquad (3.26)
\end{aligned}
$$

The bicoherence of $H(\omega)$ at (r_p, r_q) and (r_q, r_p) is then given as

$$bic^H(r_1, r_2) = \frac{A_{pq}}{\sqrt{A_{pq}^2 + A_{p+q}^2}} \qquad (3.27)$$

where A_{pq} is the magnitude of the interaction between A_p and A_q, while A_{p+q} is the magnitude of direct specular scattering at $r_p + r_q$. Notice that if $A_{p+q} = 0$, then, the bicoherence is equal to one. If there is no interaction between scatterers at r_p and r_q, then $A_{pq} = 0$ and the bicoherence is equal to zero.

3.3.4 Example 3:

Consider the canonical scatterer shown in Figure 3.5. Assume that the radar returns for this target satisfy (3.15), (i.e., they can be modeled as a sum of complex exponentials). Further, assume that the backscatter signals of magnitudes A and B correspond to scattering from the first and the second edge of the arc, respectively. Also, assume that the backscatter signal of magnitude C represents an interaction term and corresponds to propagation to the first edge then to the second edge and back to the radar. The returned signal of magnitude D corresponds to specular scattering from the tip of the flat section connected to the arc. The geometry of this target is chosen such that the time of arrival of the multiple interaction coincides with the backscatter from the tip of the flat edge (see Figure 3.5 where the dimensions are given in units of propagation time). The total returned signal is given as (where $\omega = 2\pi f$, and f is in GHz)

$$
\begin{aligned}
H(\omega) &= A \exp\left\{-j(\psi_1 + 4\omega)\right\} + B \exp\left\{-j(\psi_2 + 16\omega)\right\} \\
&\quad + C \exp\left\{-j(\psi_1 + \psi_2 + 20\omega)\right\} + D \exp\left\{-j(\psi_3 + 20\omega)\right\}
\end{aligned}
$$

The transient response of this target has three peaks; the first peak at 4 ns of magnitude $|A|$, the second peak at 16 ns of magnitude $|B|$, and the third peak at 20 ns of magnitude $|C + D|$. The birange of this target shows a peak at $(4, 16)$, and $(16, 4)$ of magnitude $|ABC|$. The peak in the birange is an indication of an interaction between the two edges of the arc. This does not imply, however, that the peak at 20 ns in the transient response

67
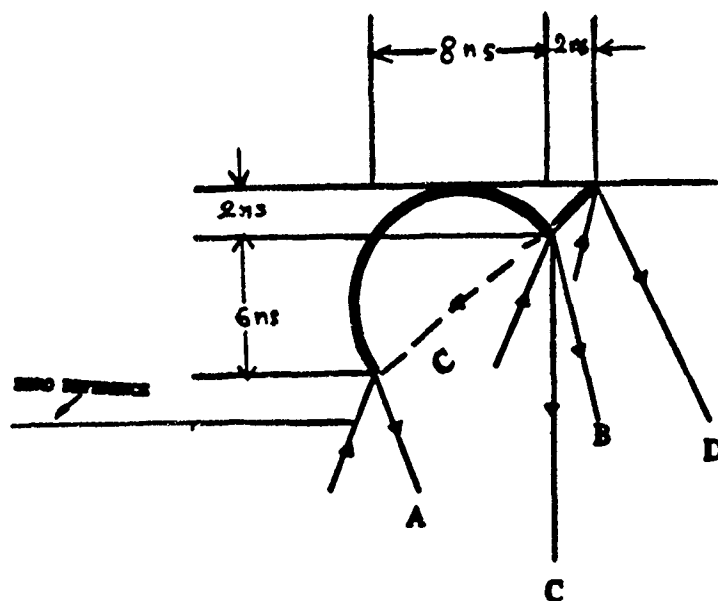
Figure 3.5: A canonical target whose specular scattering component of magnitude D is received by the radar in the same time instant as the interaction of magnitude C.

68

is totally due to multiple interactions. Moreover, the bicoherence of the peak at $(4, 16)$ ns in the birange profile is $C/\sqrt{C^2 + D^2}$ which indicates the relative magnitude of the response due to the interaction compared to the total magnitude of the response at 20 ns as displayed in the transient response. This example shows that the bicoherences of the peaks in the birange may be used to separate the responses due to multiple interactions from the responses due to specular scattering when they coincide in the transient response.

Using the bicoherence to separate between interactions and specular scattering is not as accurate as discussed above. The estimate of the bicoherence is accurate if the scattering from a radar target satisfies the model of equation (3.15). It is often the case, however, that the scattering is dispersive, so that the amplitude of specular scattering or interactions is dependent on frequency. Then the bicoherence of a pure interaction at (r_p, r_q) will not equal one. Furthermore, if neither interaction nor specular scattering occurs at (r_p, r_q), the bicoherence may not equal zero, because of residual values of the birange and spectral density at $r_p + r_q$. Nevertheless, the bicoherence of radar targets can be used to quantify the level of interactions between scatterers.

3.4   The Birange of Dispersive Scatterers

The scattering model given in (3.15), on which the interpretation of the birange is based, does not include scattering from dispersive subcomponents. In the following section we discuss the effect of scattering from dispersive targets on the interpretation of the birange.

Physically, dispersion occurs when the interrogating signal (transmitted by the radar) loses energy gradually while propagating along the target. A non-dispersive target scatters energy strongly at short time intervals rela-

tive to the propagation time along the target. A dispersive target scatters energy with lower magnitude but over longer periods of time.

An example of dispersive scattering behaviour is when the amplitude $A(\omega)$ changes with frequency as

$$A(\omega) = A_0 \exp\left\{-j\frac{\rho}{\omega}\right\} \qquad (3.28)$$

where ρ is a constant. The measured frequency response in this case is

$$
\begin{aligned}
H_d(\omega) &= \exp\left\{-j\frac{\rho}{\omega}\right\} H(\omega) \\
&= \sum_{p=1}^{m} A_p \exp\left\{-j\omega\left(\frac{\rho_p}{\omega^2} + t_p\right) - j\psi_p\right\} \qquad (3.29)
\end{aligned}
$$

by ignoring the higher order terms. Notice that, with this form of dispersion, the signal that scatters at time t_p for the non-dispersive case will scatter gradually as a function of ω. For high frequencies, scattering occurs at time t_p approximately, but as the frequency decreases the scattering center is displaced away from t_p. This corresponds to gradual energy loss along the target when illuminated by the radar. This type of dispersion has similar effects on both the transient response and the birange profile. Peaks in the transient response and the birange become less localized because of the gradual energy loss. In a special case, however, if an interaction occurs between t_p and t_q where the the dispersion coefficients are such that $\rho_p = -\rho_q$, then the positive displacement at t_p is compensated by the negative displacement at t_q, without displacing the position of the interaction term at (t_p, t_q).

Windowing the measured scattering data and the triple correlation of the data may reduce the effect of this type of dispersion on the transient response and the birange profile. By windowing the frequency response of the target, the peaks corresponding to non-dispersive scatterers are displayed over W seconds (where W is the width of the main-lobe of the

70

window used). The peaks corresponding to dispersive scatterers (of dispersion width δ seconds), however, are displayed over $W + \delta$ seconds. Thus, by choosing $W > \delta$, it is possible to reduce the disagreement between the signature of a dispersive scatterer and that of a non-dispersive one.

As another example, consider the scattering from a small conducting sphere as compared to scattering from a point scatterer. The amplitude $A(\omega)$ of the scattered signal from a sphere, when measured in the resonance region, changes with frequency as [45]

$$A(\omega) = A_0 \left(1 + \alpha \cos(\beta \omega) \right) \qquad (3.30)$$

where α, β, and A_0 are constants. Such a behaviour is a result of what is commonly known as the creeping wave. The transient response of the sphere peaks in two positions. The first peak corresponds to direct specular scattering from the sphere; the second peak is caused by the creeping wave. Therefore, the dispersive behaviour of the sphere as compared to a point target is characterized by an additional peak in the transient response.

Assume that the three-point scatterer target in Example 1 is replaced by a three-sphere target where the amplitudes $A(j\omega)$ are frequency dependent as given in (3.30). The transient response and the birange of this target are shown in Figure 3.6 for $\alpha = .6, \beta = .01$, and $A_0 = 1$. Notice that there are more peaks in the transient response due to creeping waves around each of the three spheres. The birange, however, is unaffected by such dispersive behaviour except for changes along the axes (where the magnitude squared of the transient response is displayed). Hence, while the transient response of the dispersive target has changed, the number of multiple interactions in the birange remains fixed. The reason is that, in this example, the responses corresponding to the creeping waves do not satisfy $B(t_1, t_2) - \langle h(t_1) h(t_2) h^*(t_1 + t_2) \rangle$. However, it is possible, by changing the dimensions of the target for the creeping waves to introduce, by coincidence, false

71

responses in the birange. In general, unmodeled dispersive behaviour cause changes in both the transient response and the birange profile. The birange, however, is less sensitive to these changes than the transient response.

3.5 Examples of the Birange of Experimental Targets

Examples 1 and 2 above provide an intuitive demonstration of the role of the bispectrum in identifying multiple interactions. The interpretation of the birange is also valid when scattering from a target incorporates unmodeled dynamics such as frequency dependent amplitudes and dispersive behavior. In the following, examples of the birange of experimental radar data are given. The purpose of these examples is to examine the birange of real radar signatures in terms of the interpretations given above.

This section considers some real radar targets whose frequency response is either measured experimentally or derived theoretically. The reasons for considering the following examples are: 1) To determine what can be extracted from the birange profile of canonical targets with known scattering behavior. 2) To study the effect of various parts of a generic aircraft on the birange. 3) To identify some of the scattering mechanisms from complex objects (such as commercial aircraft). 4) To consider targets whose backscattered data are measured in the S-band where the term A_{pq} in the scattering model of (3.15) has low magnitude.

The birange profiles that are displayed in the following examples only show those responses with bicoherences > 40%. The reason for displaying the birange profiles as such is to simplify the interpretation of the responses in terms of the target substructures. The triple correlations of the scattering data used to compute the birange profiles are all windowed using the Minimum Bias Supremum window function given in equation (2.45).
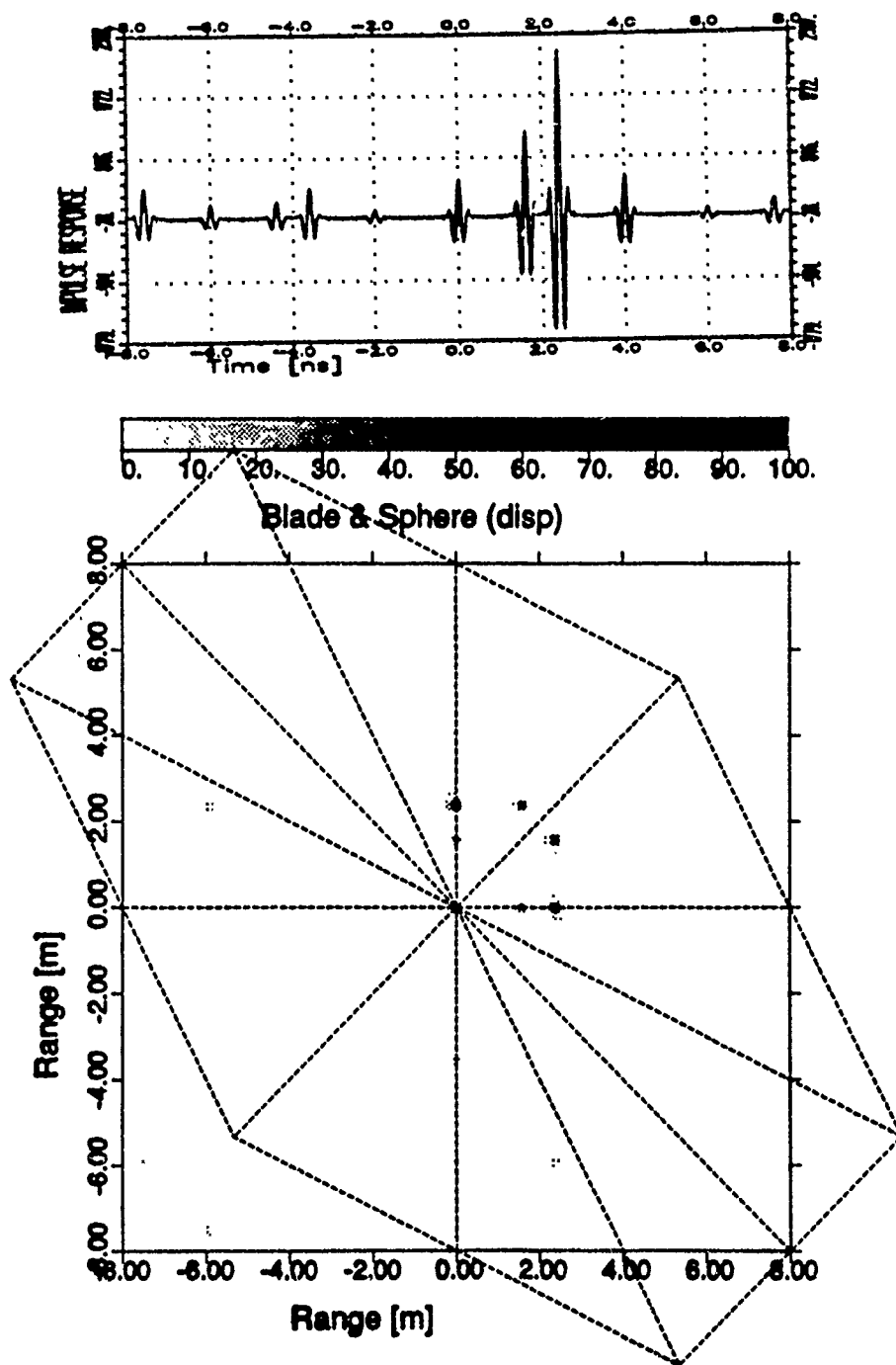
Figure 3.6: Transient response and birange profile of three-spheres target.

The following suggestions can be followed when examining the birange of real radar targets.

- Ignore any responses outside the principle triangle of each sector. The principle triangle of the first sector is defined by $r_1, r_2 \geq 0$ and $r_1 + r_2 \leq \frac{c}{2\pi\Delta f}$ where Δf is the sampling period of the measured frequency response. For properly sampled radar signals (i.e., satisfying the Nyquisit sampling criterion) no responses should appear outside the principle triangle.

- It helps to display the target along each axis and rotated according to its orientation angle with respect to the radar.

- A peak at (r_a, r_b) in the birange profile is an indication of interaction between a scattering point on the target at a distance r_a from the origin and another scattering point on the same target at a distance r_b from the origin.

3.5.1 The Birange of a Canonical Scatterer

Canonical scattering objects are usually considered for mechanism identification problems, and are useful for compact range studies. Usually, scattering from canonical objects is examined in the time domain using the transient response. Because canonical scatterers have a small number of scattering terms, their scattering responses are relatively simple and can be studied in detail.

The Tilted Flat Plate

The canonical target considered is a 2ft × 2ft flat plate whose trailing edge is tilted by 46° above the horizontal. In addition to specular scattering from the edges of the plate, a few multiple interactions are also displayed in the

74

transient response (see Figure 3.8). A possible scenario of an interaction of this flat plate is (see Figure 3.7) radar, to first corner, to second corner, to radar where the first and second corners are either on a common edge (denoted by g) or diagonally opposite (denoted by c). Another possible scenario of interactions of this plate is radar, to first edge, to second edge, to first edge, to second edge, to radar (denoted by d). Notice that the time delay of the interactions that follows scenario g will be dependent on the width of the plate and not on the delay to each of the interacting scatterers because the signal that encounters the interaction travels once along the plate. However, the time delay of the interactions that follow the second scenario is dependent on the propagation time to each of the interacting scatterers. Therefore, it is expected that the birange will detect the interactions that follow the second scenario.

The transient response and the birange profile of the flat plate at 5° azimuth are shown in Figure 3.8. The frequency band used is $2 - 18$ GHz with an increment of 20 GHz. Notice that in both figures only one interaction is detected in the birange which can be interpreted, using the second scenario, as a double bounce between the leading and trailing edges of the plate (denoted by d in Figure 3.7). This interpretation can be further justified by the fact that the birange profile of the plate at 0° azimuth shows the same interaction.

3.5.2 The Birange of a Generic Aircraft Model

We first examine the scattering from a generic aircraft model with removable parts (denoted by FWST [75] in Figure 3.9). The advantages of studying a target with removable parts are: 1) to examine the contribution of each part of the aircraft to the total number of scattering mechanisms that can be extracted, 2) to follow the changes in the transient responses or the
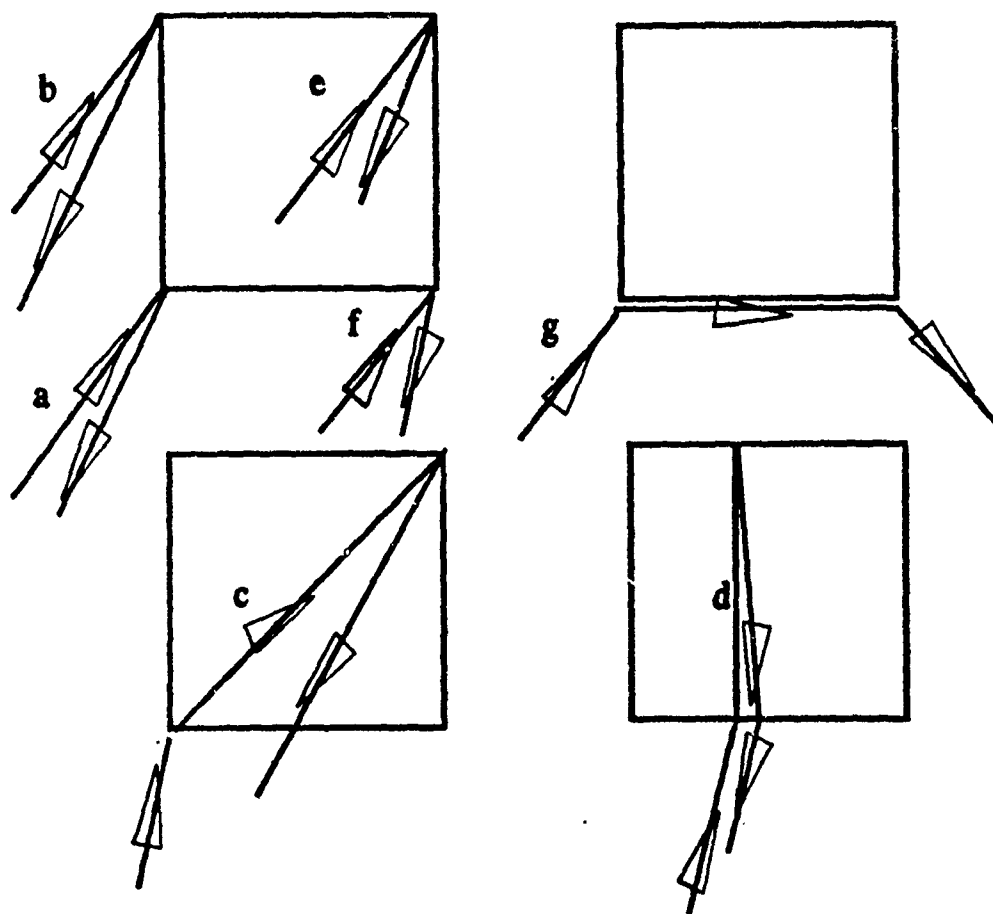
Figure 3.7: Scenarios of possible interactions for the tilted flat plate.

Figure 3.8: Transient response and birange profile for tilted flat plate at 5°
azimuth.

birange profiles as more parts are added to (or removed from) the target.

The frequency band of the data used in this example is 2 GHz to 18 GHz with a frequency increment of 100 MHz. The FWST model is 6 inches long with a wing span of 4 inches. Figures 3.10-3.12 show the birange profile of different configurations of the aircraft parts. Notice that for the case where scattering is from the fuselage only (see Figure 3.10), there is a single response in the birange which could be due to scattering from the nose and then the trailing edge of the fuselage.

If the horizontal stabilizer is added to the fuselage (see Figure 3.11), then a multiple interaction between the leading edge of the stabilizer and the nose (denoted by a in Figure 3.11) is detected. Also detected in the birange, is an interaction (denoted by b in Figure 3.11) between the leading edge of the stabilizer and the opening in the fuselage where the wing part of the aircraft is inserted. Similarly an interaction (denoted by c in the same Figure) is detected between the trailing edge of the stabilizer and the same opening in the fuselage. The responses on the diagonal are not well understood but may be due to scattering from the corners between the front edge of stabilizer and the fuselage.

Figure 3.12 shows the birange profile and the transient response when all parts of the aircraft are present. Notice that the response denoted by a is an interaction between the trailing edge of the wing and the corner between the wing leading edge and the fuselage. A similar interaction (denoted by b) between the leading edge of the stabilizer and the wing-fuselage corner is also detected. The response on the diagonal (denoted by c) is possibly due to interaction between both ends of the wing (corresponds to scattering from one end of the wing then scattering from the other end). Notice that the interactions between the stabilizer and the opening in the fuselage that are shown in Figure 3.12 (denoted by b and c) do not appear in Figure 3.12

after inserting the wing into the fuselage.

The above examples of the birange profiles of the generic FWST aircraft show that interactions between the edges of the stabilizer and the edges of the wing are likely to appear in the birange. Further, the addition of parts of large size relative to size of the fuselage (such as the stabilizer or the wing) yields significant changes in the birange profile of the generic target.

3.5.3 The Birange of Real Aircraft Models

In the following, we study the birange profiles of real aircraft models. The birange profiles of the generic aircraft model studied in the previous section may help examining the birange of real aircraft models. The major difference between scattering from the generic aircraft and a real target model is scattering from the engines. The engines are often major contributors to scattering from real radar targets [75]. Therefore, in addition to scattering from the wing and stabilizers, interactions between the engines and other scattering subcomponents of a real target are likely to be detected in the birange profile.

There are two reasons for examining the birange profile of real aircraft models: 1) such targets are likely radar targets, and 2) their structures are very complex and therefore consist of a broad spectrum of scattering mechanisms including multiple interactions. The goals of considering the birange of real aircraft models are: 1) to attempt to identify some of the scattering mechanisms in the birange, and 2) to discriminate between targets based on their birange profiles. The discrimination problem is considered in Chapter V.

The birange profiles for scale models of five commercial aircraft models are shown in Figures 3.13-3.17. Details of the radar measurements of these targets can be found in [68]. The backscattered signals are in the frequency
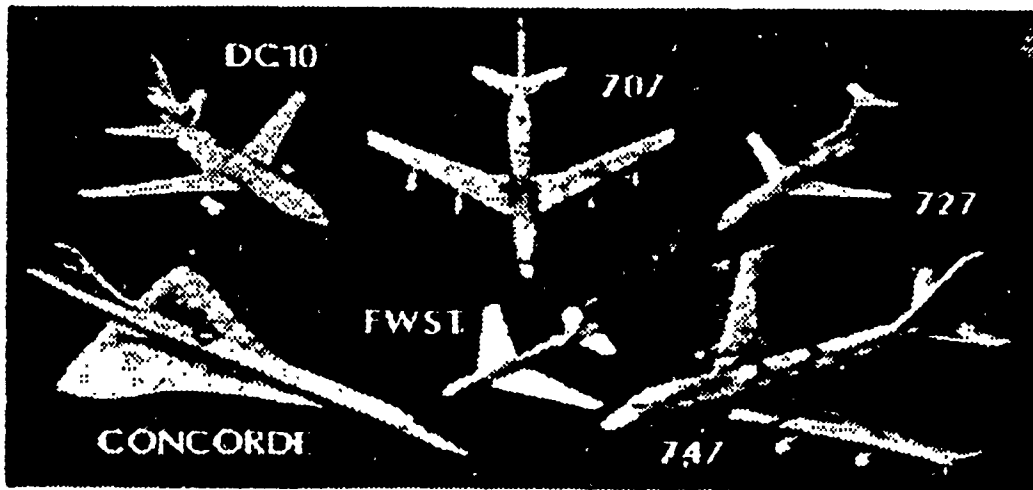
Figure 3.9: Photo of commercial aircraft used in this study.
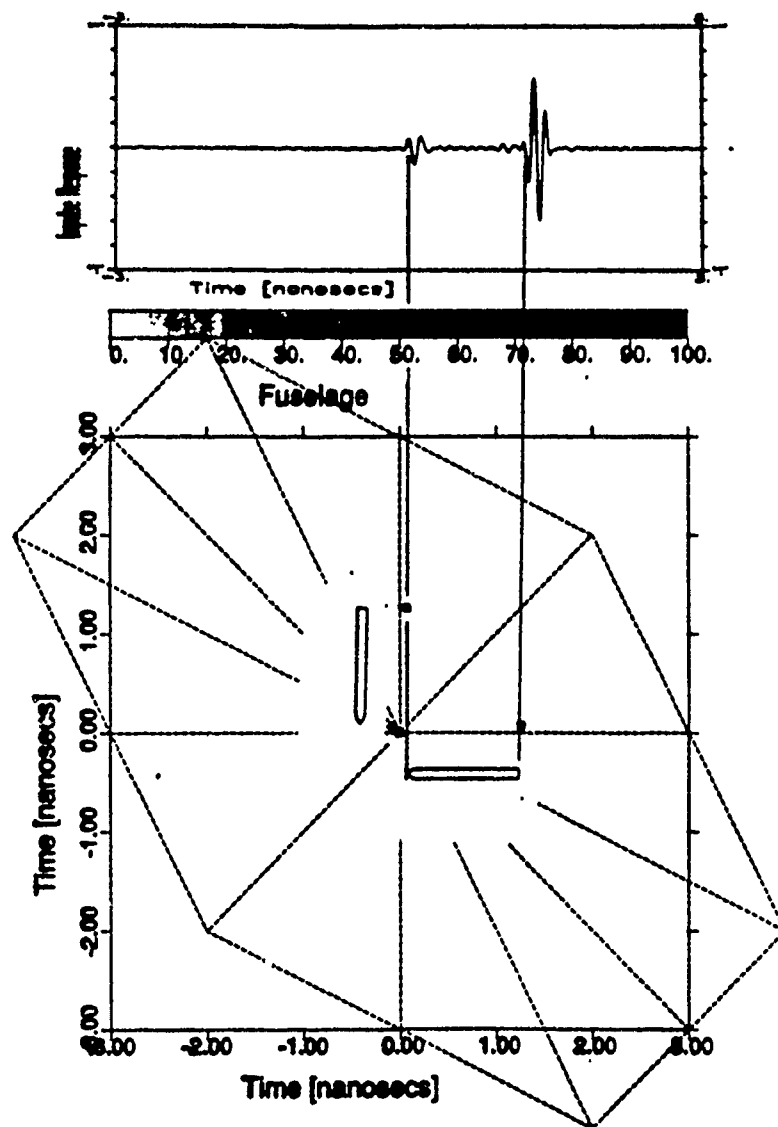
Figure 3.10: Impulse response and birange profile for generic aircraft model consisting of fuselage only
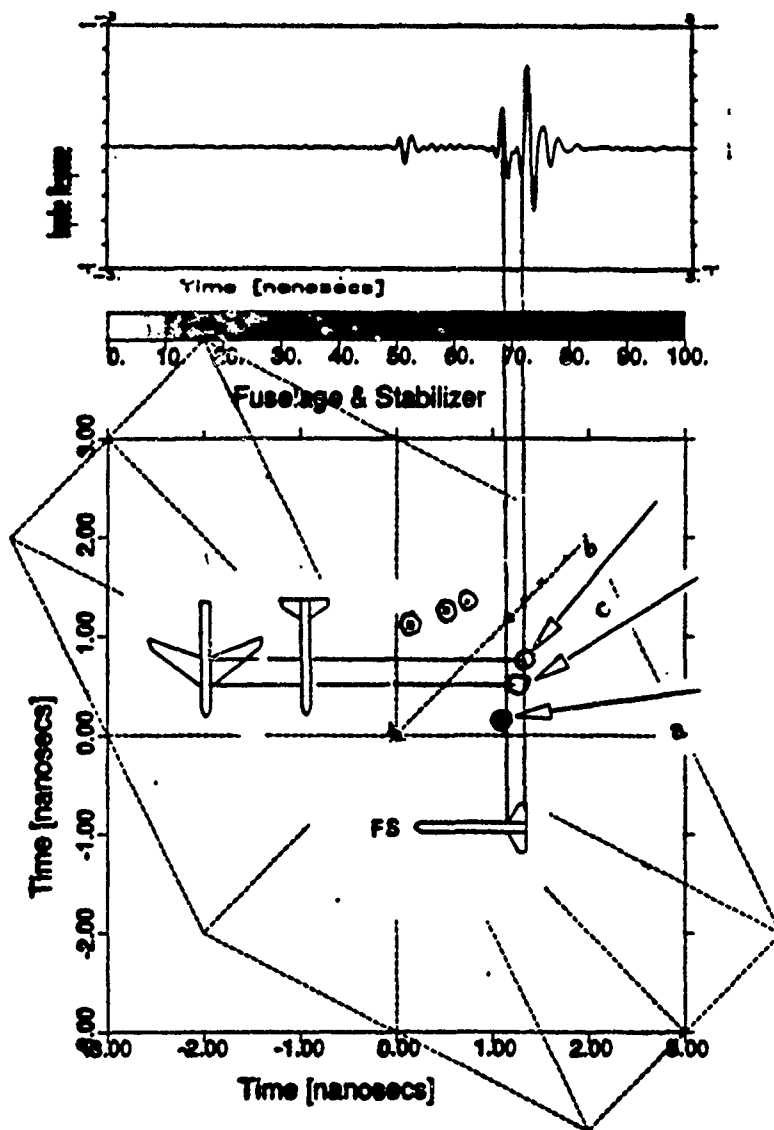
Figure 3.11: Impulse response and birange profile for generic aircraft model
consisting of fuselage and stabilizer.

82
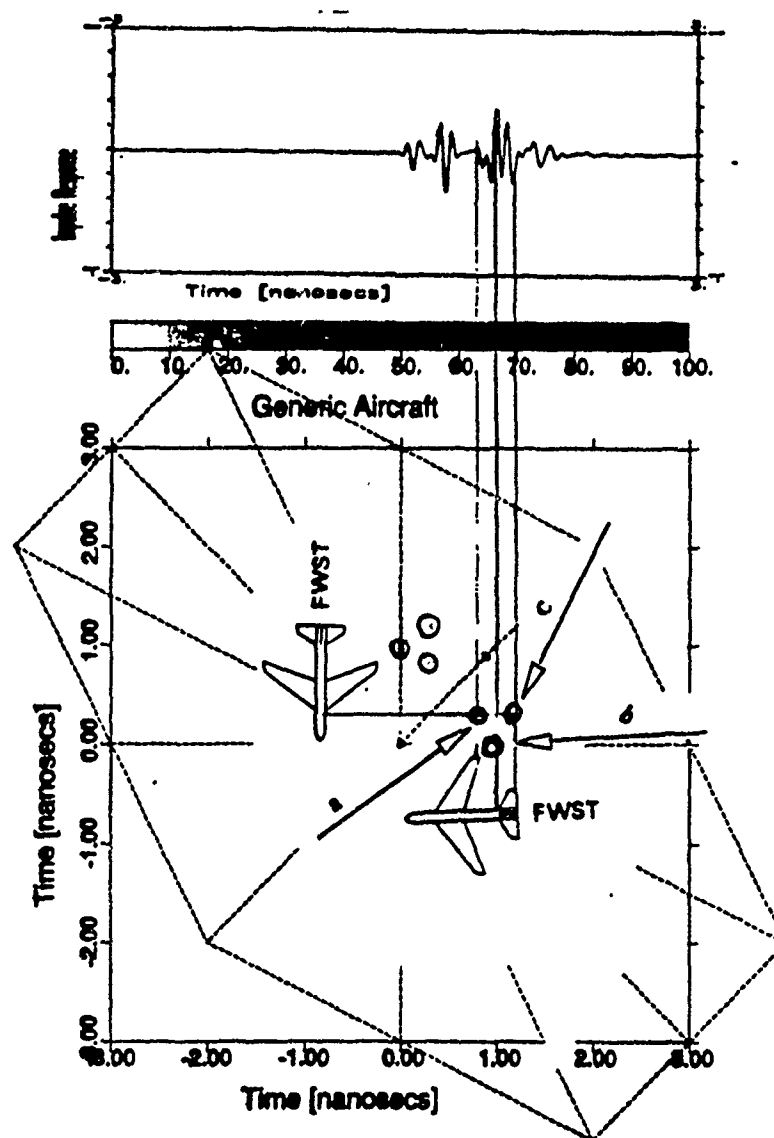
Figure 3.12: Impulse response and birange profile for generic aircraft model (complete set).

83

range (1.5 − 12) GHz which corresponds to the resonance scattering region for full scale targets. The polarization mode used is Horizontal transmit Horizontal receive (HH). Notice that the dominant responses in each figure correspond to scattering from the wing and engines. Additional responses around the stabilizer-tail region are also recovered.

Figure 3.13 shows the birange profile and the transient response for the Boeing 707 at 0°. The birange of this target shows interactions between the engines and the stabilizer (denoted by a), between both edges of the stabilizer (denoted by b), and between the fuselage-tail corner and the leading edge of the wing (denoted by c). Figure 3.13 also shows other interactions of lower magnitudes. Figure 3.14 shows the transient response and the birange profile for the Boeing 727. The interactions detected in this case are between the engines and the wing-fuselage corner (denoted by a) and between the wing tip and the front edge of the fuselage (denoted by b). Some of the responses, however, cannot be explained easily (such as the one denoted by c) and are perhaps due to interactions between the windows of the airplane and other parts of the aircraft. Figure 3.14 also shows other interactions of lower magnitudes. Figure 3.15 shows the interactions detected in the birange profile of the Concord. These interactions are between the engines and fuselage front edge (denoted by a), between the tail and the wing-fuselage corner (denoted by b), and between the tail and the wing tip (denoted by c). The birange profile of the Boeing 747 (see Figure 3.16) shows interactions between the wing tips and the engines (denoted by a) and between the stabilizer and the wing-fuselage corner (denoted by b). Figure 3.17 shows the birange and the impulse response for the DC10 target model. Three interactions are detected in the birange of this target; the first is between the engine and front edge of the fuselage (denoted by a), the second is between the stabilizer and wing-fuselage corner (denoted

by b), and the third is perhaps between a window of the airplane and the leading edge of the wing (denoted by c).

It is clear from the above figures that some aircraft models have more significant interactions than other models. Hence, the birange is more informative for some targets than others. Also, it is clear from these figures that different targets have significantly different birange signatures. Therefore, the birange profile is a potential candidate for target classification.

After detecting the interaction terms (with bicoherence ≈ 1) in the birange profiles of the above target models, the corresponding terms in the transient responses were located. By examining the relative amplitude of the interaction terms of real target models as they appear in the transient response, it is possible to conclude that these interactions have relatively low magnitude compared to the magnitude of the responses that correspond to specular scattering. To quantify this result let SIR denote the ratio of specular scattering to interactions in dB as they appear in the transient response. The specular scattering component is computed as the average of the magnitudes of the interacting scatterers $(|h(r_1)| + |h(r_2)|)/2$. The magnitude of the interaction is given as $|h(r_1+r_2)|$ provided that no specular scattering appears at $r_1 + r_2$ (bicoherence ≈ 1). SIR is then given as

$$ SIR = 20 \log \left[\frac{|h(r_1)| + |h(r_2)|}{2|h(r_1 + r_2)|} \right] \qquad (3.31) $$

After estimating SIR for several interaction terms in the above examples, we observe that

$$ 1 \text{ dB} < \text{SIR} < 20 \text{ dB}. \qquad (3.32) $$

This result indicates that the interaction terms are not always easily recognized in the transient response of real target models. Therefore, it is reasonable to assume that most responses of comparable magnitudes in the transient response of a real target model correspond to specular scattering. If the goal, however, is to search for interactions and the interest is

85

in the type of scatterers that produced these interactions, then the above result shows the importance of the birange profile in detecting multiple interactions, especially those with low magnitudes.

3.5.4 The Birange of S-Band Scattering Data

In this section we examine the birange profile of an aircraft measured with an S-band radar. The target size is about 200 times the operating wavelength. The measurement frequency band is 3.1 − 3.4 GHz for a full scale aircraft. The data consist of 64 frequency measurements corresponding to a frequency increment of 4.1 MHz. The measurements were taken while the aircraft was in operation and are therefore corrupted with noise. Details on the calibration and motion compensation of this data are given in [69].

Scattering at such high frequencies is very localized and highly specular [75]. In general, due to the large target-size to wavelength ratio, the specular part of the signal is the most dominant in the transient response [75].

Figure 3.18 shows the transient response and the birange of the A4 whose backscatter data were measured at S-band. It is clear that the birange of such a target reveals the complex scattering mechanisms between various subcomponents of the target scattering elements. Several interactions are detected particularly between the engines and the stabilizer (denoted by a), between the tail and the wing tip denoted by b), and between the fuel tank and the wing (denoted by c). A common feature of all detected interactions is that the SIR is higher than that obtained for scattering in the resonance region. The reason is that, while scattering in the S-band is more localized and can be more easily resolved, compared to scattering in the resonance region, the propagating short wave between interacting scatterers becomes weaker due to diminished electromagnetic
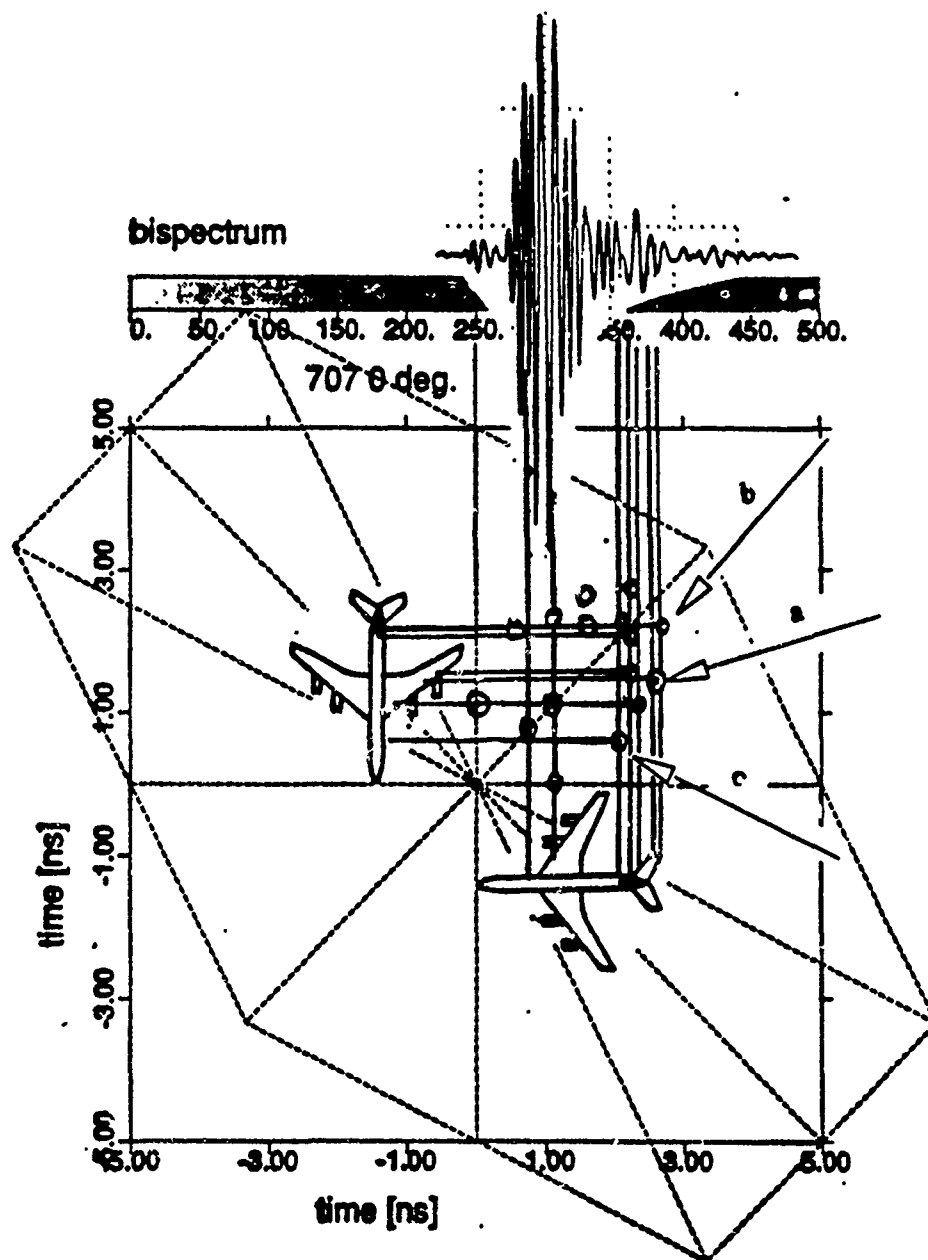
Figure 3.13: Birange profile for the Boeing 707 model at 0° azimuth

87
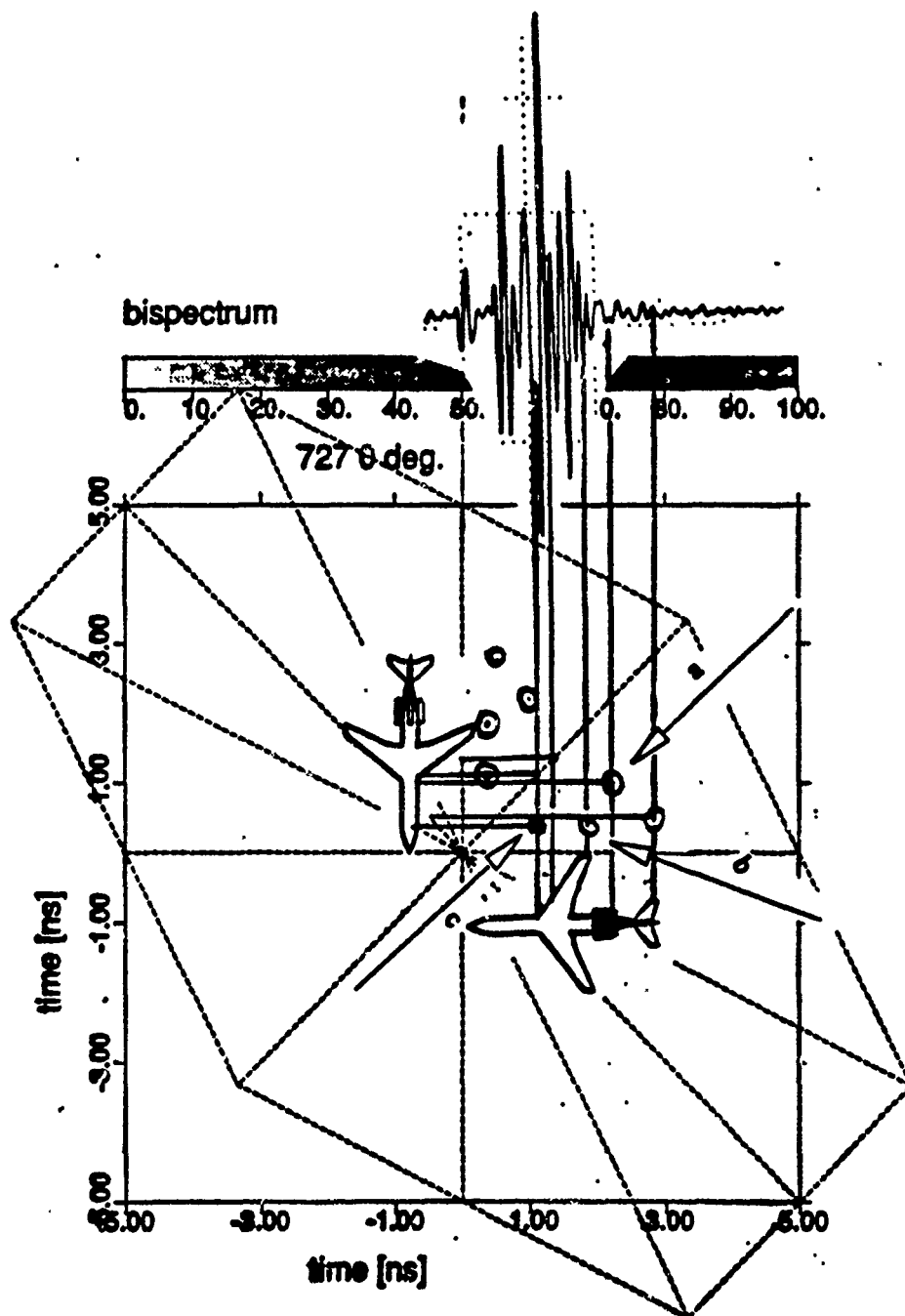
Figure 3.14: Birange profile for the Boeing 727 model at 0° azimuth
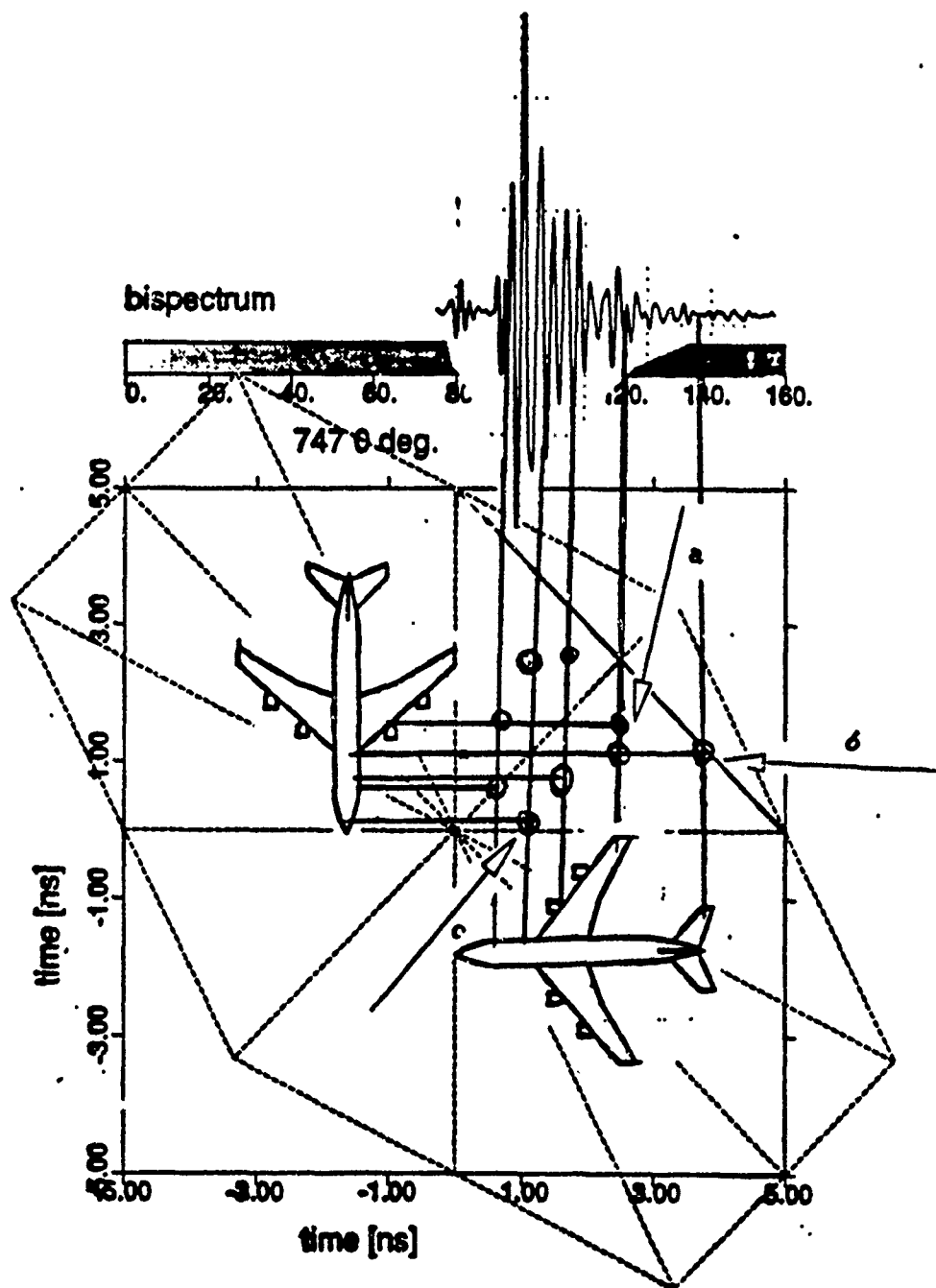
Figure 3.15: Birange profile for the Boeing 747 model at 0° azimuth
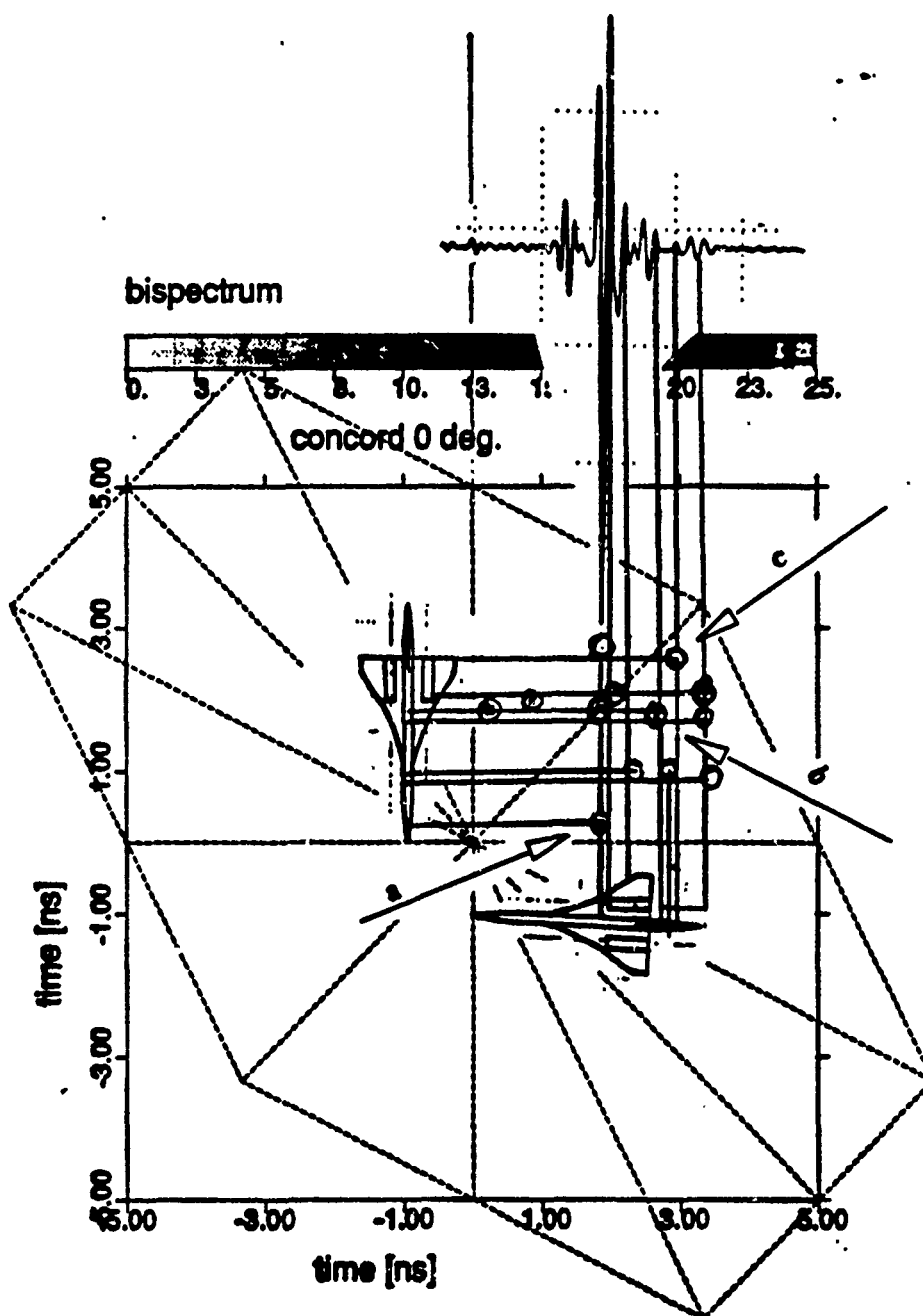
Figure 3.16: Birange profile for the Concord model at 0° azimuth

90
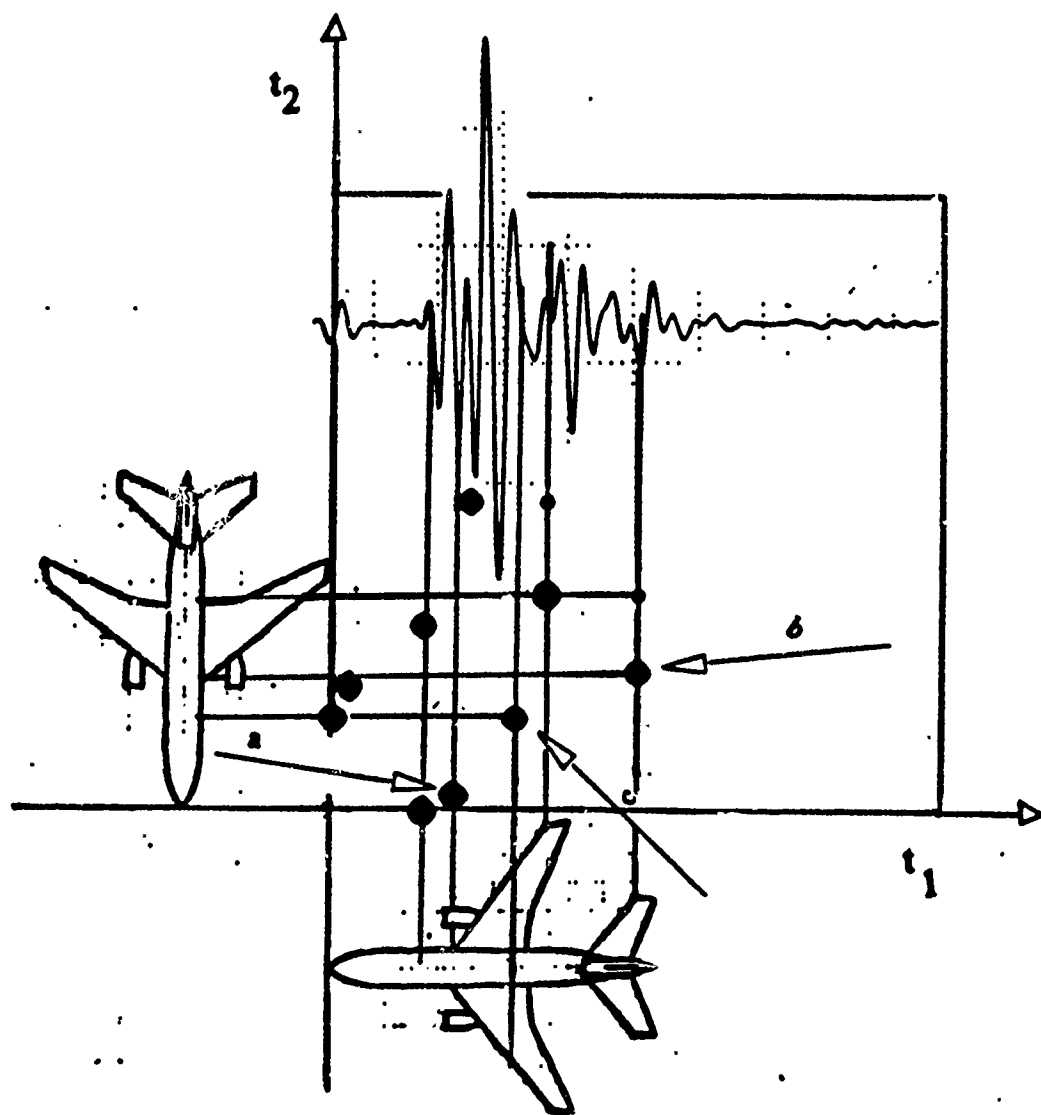
Figure 3.17: Birange profile for the DC10 model at 0° azimuth

coupling [71].

It is possible to extract many details about the target scattering behavior in the S-band frequency range from the birange profile. These interactions, however, are sensitive to changes in the target aspect angle because of the large size of the target relative to the wavelength.

3.6   Extraction of Scattering Features From The Transient Response and The Birange

The above examples of the birange of real aircraft models have shown that some of the interactions can be detected using the birange concept. The coordinates of the responses in the birange indicate the location of the interacting scattering subcomponents. The accuracy of these coordinates depends on the fast Fourier transform algorithms and the number of pixels used to display the birange profile. It is also clear from these figures that it is possible to characterize a radar target by a small number of features extracted from both the transient response and birange profile. Therefore, it is possible to reduce the data storage requirement of the birange profile if the interactions shown in these examples are extracted and labeled in terms of their coordinates and bicoherences. An algorithm for extracting scattering mechanisms from the birange profile when estimated using classical bispectral estimation techniques is given in this section.

It is possible to use the extracted features in a structural pattern recognition machine that discriminates between targets using relational graph matching techniques [76]. Also, estimates of the locations of scattering mechanisms (which are more accurate than the estimates given by the FFT algorithm) can be obtained using the following feature extraction algorithm. The following algorithm is a generalization of the peak search algorithm used in [77] for estimation the location of the peak in the tran-
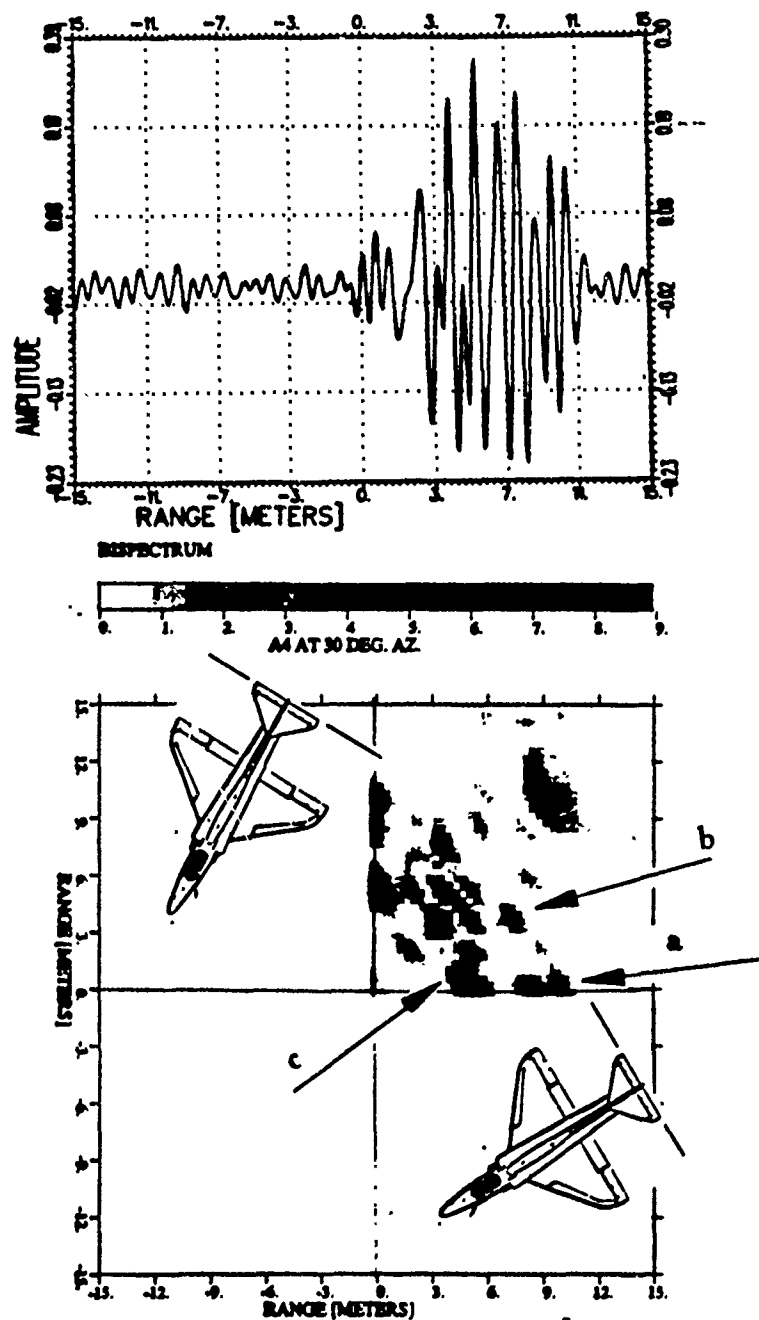
Figure 3.18: Transient response and birange profile of the A4 aircraft (S-band scattering).

sient response.

Feature Extraction Algorithm:

1- Estimate the birange profile and the transient response as given in Section 3.1. (Better results were obtained when the window function used is Gaussian [77], possibly because the Fourier transform of a Gaussian function is also Gaussian).

2- Search for local maxima in the birange where each selected peak occurs among six adjacent points as shown in Figure 3.19. If (t_{1i}, t_{2j}) indicates the location of the selected peak, then

$$|B(t_{1i}, t_{2j})| = \max\{|B(t_{1(i-1)}, t_{2(j-1)})|, |B(t_{1(i-1)}, t_{2(j+1)})|, \quad (3.33)$$

$$|B(t_{1i}, t_{2(j-1)})|, |B(t_{1i}, t_{2(j+1)})|, |B(t_{1i}, t_{2j})|$$

$$|B(t_{1(i+1)}, t_{2(j-1)})|, |B(t_{1(i+1)}, t_{2j})|\}.$$

Also, search for the peaks in the transient response using the algorithm given in [75].

3- Fit a Gaussian function to each set of data consisting of the selected peak in the birange and the neighboring six minima. Let t_{1c} and t_{2c} denote the coordinates of a local maximum. Then the Gaussian window function is given as

$$w(t_1, t_2) = A \exp\left\{-\alpha(t_1 - t_{1c})^2 - \beta(t_2 - t_{2c})^2\right\} \quad (3.34)$$

Given the coordinates and the magnitudes of seven bispectral samples (see Figure 3.20) including the maximum given using the FFT algorithm, we need to solve for α, β, t_{1c}, t_{2c}, and A. Therefore, estimates of these parameters can be obtained using local least-squares fit on all seven samples. The estimates of t_{1c} and t_{2c} in the bispectral response can then be obtained by the following

$$t_{1c} = \frac{x_1 + x_2}{2} \quad (3.35)$$

94

$$t_{2c} = \frac{x_3 + x_4}{2}$$

where

$$x_1 = \frac{(r_1 - 1)(t_{1i}^2 - t_{1(i-1)}^2)}{2r_1(t_{1(i-1)} - t_{1i}) - 2(t_{1(i-1)} - t_{1i})} \qquad (3.36)$$

$$x_2 = \frac{(r_2 - 1)(t_{1i}^2 - t_{1(i-1)}^2)}{2r_1(t_{1(i-1)} - t_{1i}) - 2(t_{1(i-1)} - t_{1i})}$$

$$x_3 = \frac{(r_3 - 1)(t_{2j}^2 - t_{2(j-1)}^2)}{2r_2(t_{2(j-1)} - t_{2j}) - 2(t_{2(j-1)} - t_{2j})}$$

$$x_4 = \frac{(r_4 - 1)(t_{1i}^2 - t_{1(i-1)}^2)}{2r_3(t_{1(i-1)} - t_{1i}) - 2(t_{1(i-1)} - t_{1i})}$$

and

$$r_1 = \frac{\ln(|B(t_{1i}, t_{2j})|) - \ln(|B(t_{1(i+1)}, t_{2j})|)}{\ln(|B(t_{1i}, t_{2j})|) - \ln(|B(t_{1(i-1)}, t_{2j})|)} \qquad (3.37)$$

$$r_3 = \frac{\ln(|B(t_{1i}, t_{2j})|) - \ln(|B(t_{1i}, t_{2(j+1)})|)}{\ln(|B(t_{1i}, t_{2j})|) - \ln(|B(t_{1i}, t_{2(j-1)})|)} \qquad (3.38)$$

$$r_4 = \frac{\ln(|B(t_{1(i-1)}, t_{2(j+1)})|) - \ln(|B(t_{1(i-1)}, t_{2j})|)}{\ln(|B(t_{1(i+1)}, t_{2j})|) - \ln(|B(t_{1(i+1)}, t_{2(j-1)})|)} \qquad (3.39)$$

$$r_2 = \frac{\ln(|B(t_{1(i-1)}, t_{2(j+1)})|) - \ln(|B(t_{1i}, t_{2(j+1)})|)}{\ln(|B(t_{1(i+1)}, t_{2(j-1)})|) - \ln(|B(t_{1i}, t_{2(j-1)})|)} \qquad (3.40)$$

4- Fit a Gaussian window to each set of data consisting of the selected peak and the neighboring minima in the transient response [77]. The location t_c of the peak in the transient response can then be estimated using

$$t_c = \frac{t_{k+1}^2 - t_k^2 + r(t_k^2 + t_{k-1}^2)}{2r(t_k - t_{k-1}) + 2t_{k+1} + 2t_k} \qquad (3.41)$$

where t_k and t_{k+1}, t_{k-1} denote the location of the selected peak as given using the Fourier transform and the location of the adjacent values. The parameter r is given as

$$r = \frac{\ln(|h(k)|) - \ln(|h(k+1)|)}{\ln(|h(k)|) - \ln(|h(k-1)|)} \qquad (3.42)$$

95

where $|h(k)|$ is the magnitude of the transient response at time k.

5-All detected maxima must satisfy the symmetry properties of the birange. This condition is needed to detect any possible failures of this peak search algorithm. If some peaks do not satisfy the symmetry properties of the bispectrum then repeat the search starting from a different corner of the bispectral hexagon.

6-If the measured data are noisy then, to eliminate noise peaks, ignore any local maximum in the birange profile where the magnitude of the birange at this maximum is such that $|B(r_1, r_2)| < K\sigma^3$ where σ is the noise standard deviation and K is a constant ($K = 1$ is used in this study). Also, ignore any local maximum in the transient response where the amplitude of the response at this maximum is such that $|h(r)| < \sigma$

Experimental Results

Table 3.1 shows two examples of the estimates of the coordinates of the interaction term of the blade-sphere target using the above algorithm. The true values of the coordinates and those given by the Fourier transform algorithm are also shown. The range resolution is $\delta r = 0.015$ meters, corresponding to 10 GHz frequency band. Notice that the estimates obtained using the above algorithm are closer to the true values compared to those given by the fast Fourier transform.

The features extracted from the birange profiles of five commercial aircraft using the above algorithms are listed in Tables 3.2-3.3. Notice that neither the number of scattering centers (extracted from the transient response) nor the number of interactions (extracted from the birange) is the same for both targets.

96
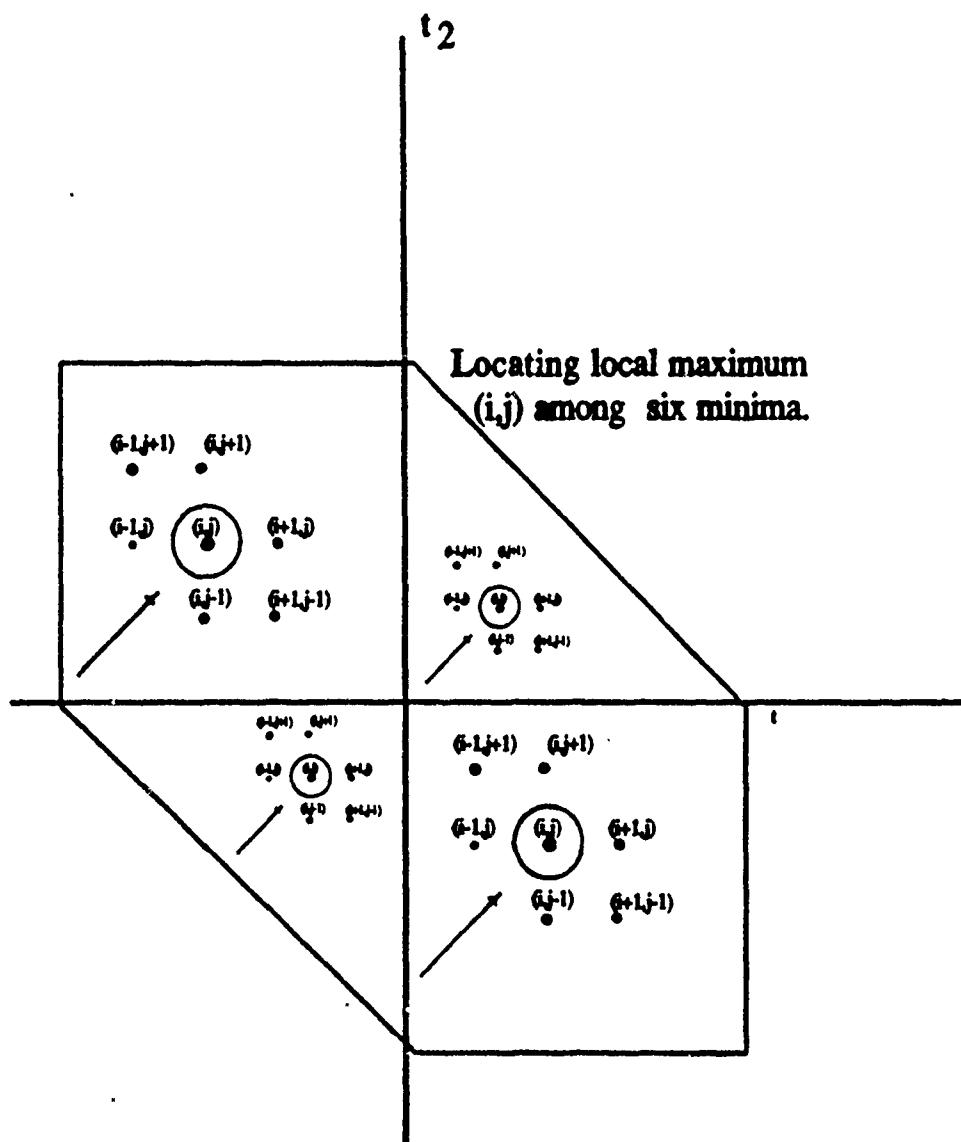
Figure 3.19: Feature extraction technique; locating a maximum surrounded by six minima

97
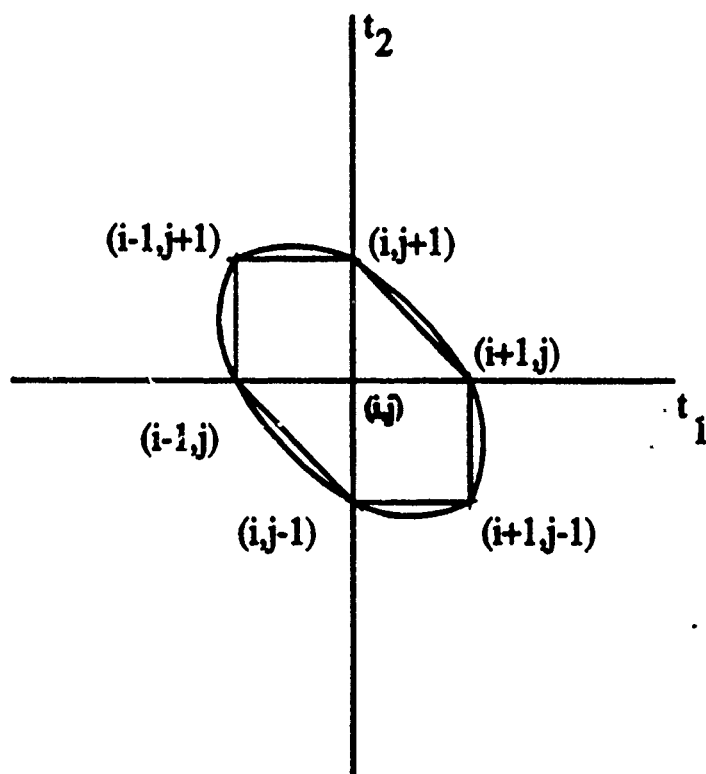
Figure 3.20: Fitting a Gaussian function to estimate the true location of the interaction using seven bispectral samples.

Table 3.1: Comparison between bi-range estimates obtained using Gaussian fitting technique, FFT algorithm and the true values.

Blade-Sphere Target $\delta r = .015$ m			
Location of Interaction Term			
Examples	True	FFT	FIT
Example #1, r_1	0.1789	0.1715	0.1745
Example #1, r_2	0.3111	0.3185	0.3168
Example #2, r_1	0.0872	0.0725	0.0726
Example #2, r_2	0.3965	0.3869	0.4105

Table 3.2: Features extracted from birange profile and transient response for a Boeing 707

B707 at SNR = 10 dB, 0 deg. Azimuth		
Model length $\approx .32$ m, $\delta r \approx .015$ m		
Scatt. Centers	Range [meters]	Amplitude [dB]
No. 1	.0165	1.15
No. 2	.1213	2.14
No. 3	.1901	2.36
No. 4	.2372	2.03
Interactions	Birange (r_1, r_2)	Bicoherence
No. 1	(.1209,.2822)	47 %
No. 2	(.1933,.3185)	53 %

Table 3.3: Features extracted from birange profile and transient response for a Boeing 727

B727 at SNR = 10 dB, 0 deg. Azimuth		
Model length ≈ .235 m, δr ≈ .015 m		
Scatt. Centers	Range [meters]	Amplitude [dB]
No. 1	.0143	1.13
No. 2	.1036	1.69
No. 3	.1775	1.94
No. 4	.2249	0.90
Interactions	Birange (r_1, r_2)	Bicoherence
No. 1	(.0673,.1106)	87 %
No. 2	(.0252,.1765)	44 %
No. 3	(.1841,.1093)	52 %

3.7 The Effect of Noise on The Birange Profile

Radar scattering signatures are usually corrupted with additive noise and clutter. In this section we investigate the effect on the birange profile of additive disturbances to the frequency domain scattering data. The disturbance model used for noise and clutter is a stochastic model [45]. The noise model is Gaussian (colored or white). Ksienski and White [22], described the noise model of a radar system as being both additive and multiplicative, where the additive part is due to thermal and shot noise, and the multiplicative part is due to measurement errors and is dependent on the signal. According to [22], if none of the noise sources is dominant and by virtue of the central limit theorem, the assumed noise model is zero mean white Gaussian. The clutter model is either Gaussian (due to migrating birds and weather, [17]) or non-Gaussian (due to ground clutter [17]). Combining the two models, it is possible to classify disturbances into two groups: Gaussian and non-Gaussian.

3.7.1 Additive Gaussian Noise

The third moment of any zero mean random variable with symmetric distribution is zero. Hence, the triple correlation of a zero mean random variable with symmetric probability density function is zero, which implies that the bispectrum of a pure noise signal is zero. Let $H'(f)$ denote the noise contaminated scattered radar signal at frequency f.

$$H'(f) = H(f) + n(f) \tag{3.43}$$

where $n(f)$ is a zero mean Gaussian random variable, and $H(f)$ is the noiseless backscattered signal. Also, assume that the sample mean is removed from both the noisy data $H'(f)$ and the noiseless catalog data $H(f)$, so that $E\{H'(f)\} = 0$. Then the third order cumulant of $H'(f)$ is

$$
\begin{aligned}
R^{H'}(f_1, f_2) &= E\{H'^{*}(f)H'(f + f_1)H'(f + f_2)\} = R^H(f_1, f_2) \tag{3.44}\\
&\Rightarrow B^{H'}(t_1, t_2) = B^H(t_1, t_2).
\end{aligned}
$$

Therefore, the birange of noisy radar signals should be unaffected by additive Gaussian noise provided that an infinite number of data samples is available. In practice, however, only a finite number of data samples is available. Hence, additive Gaussian noise is not totally suppressed in the birange profile.

Figure 3.21 shows the transient response and the birange profile of the hypothetical target of Example 1 where the simulated radar returns are corrupted with additive white Gaussian noise at -10 dB signal-to-noise ratio (SNR). Compare Figure 3.21 with the corresponding noiseless profiles shown in Figure 3.2. Notice that, while it is difficult to identify some of the scattering mechanisms in the noisy transient response, it is possible to do so in the noisy birange profile as shown in Figure 3.21. Thus, birange processing seems to more effectively suppress the additive Gaussian noise

101

than does transient response processing. This does not necessarily imply that noisy radar targets can be classified with a lower probability of error using the birange (see Chapter V).

Suppression of additive Gaussian noise is dependent on the number of data samples used to estimate the triple correlation of the data. To study the effect of noise on the birange profile when it is estimated using either finite or infinite data sequences, it is appropriate to examine the estimates of the triple correlations of noisy radar returns. The expected value of the triple correlation of noisy backscatter data $H'(f)$, denoted by $R^{H'}(f_1, f_2)$ and estimated using (3.7) is related to expected value of the triple correlation of the noiseless data $R^H(f_1, f_2)$ by the following;

$$R^{H'}(f_1, f_2) = R^H(f_1, f_2) \tag{3.45}$$

$$+ \frac{1}{N} \sum_{i=1}^{N} H^*(f_i) H(f_1 + f_i) n(f_i + f_2) + \frac{1}{N} \sum_{i=1}^{N} H^*(f_i) H(f_2 + f_i) n(f_i + f_1)$$

$$+ \frac{1}{N} \sum_{i=1}^{N} H(f_i + f_1) H(f_i + f_2) n^*(f_i) + \frac{1}{N} \sum_{i=1}^{N} H^*(f_i) n(f_i + f_1) n(f_i + f_2)$$

$$+ \frac{1}{N} \sum_{i=1}^{N} H(f_i + f_1) n^*(f_i) n(f_i + f_2) + \frac{1}{N} \sum_{i=1}^{N} H(f_2 + f_i) n^*(f_i) n(f_1 + f_i)$$

$$+ \frac{1}{N} \sum_{i=1}^{N} n^*(f_i) n(f_i + f_1) n(f_i + f_2).$$

As $N \to \infty$ the second, third, and fourth terms on the right hand side of the above equation converge to [57] $\{r^H(f_1) + r^H(f_2) + r^H(f_1 - f_2)\} E\{n\} = 0$ where $r^H(f_k) = E\{H^*(f) H(f + f_k)\}$, and $E\{n\} = 0$. Also, the fifth, sixth, and seventh terms converge to $3\sigma^2 E\{H\} = 0$, where σ^2 is the noise variance and $E\{H\} = 0$ (due to subtracting the mean from the data). The last term can be written as $E\{n^3\} = 0$. Segmentation or averaging over independent records may be needed for convergence of these terms [57]. Therefore, as $N \to \infty$ the estimate of the noisy triple correlation approaches the estimate

of the noiseless triple correlation, thus producing noise-free birange profiles.

$$\lim_{N\to\infty} R^{H'}(f_1, f_2) \to R^H(f_1, f_2) \tag{3.46}$$

An expression for the expected value of the error between the estimate of the triple correlation using a finite sequence of noisy radar data and the estimate using noiseless data is given below. This expression represents the effect of noise on the birange profile when estimated using a finite number of data samples N. Let $a = r^H(0)$. Then after algebraic manipulation of products of the terms in (3.45), the following is obtained

$$E\{R^{H'}(f_1, f_2) - R^H(f_1, f_2)\}^2 = \frac{1}{N}\left[9a^2\sigma^2 + 45a\sigma^4 + 15\sigma^6\right] \tag{3.47}$$

where σ^2 is the noise variance. This means that the mean square error between the noisy triple correlation $R^{H'}$ and the noiseless triple correlation R^H is dependent on the noise power and increases as a function of σ^6. Equation (3.47) can be regarded as a quantitative measure of the effect of noise on the birange when estimated using finite data records.

3.7.2 Additive Non-Gaussian Noise

By virtue of the central limit theorem [22], the additive noise in the radar scattering data are assumed to be Gaussian. Generally, the additive noise is not Gaussian for two reasons: 1) The noise is partially multiplicative, and so is only asymptotically Gaussian. 2) Clutter is often modeled as a non-Gaussian disturbance added to the scattering data.

In this section we study the effect of additive non-Gaussian noise on the birange. Consider the following,

$$H'(f) = H(f) + C(f) \tag{3.48}$$

where $H'(f)$ is the backscattered frequency response of a certain target and C_f represents non-Gaussian noise. The triple correlation of the above
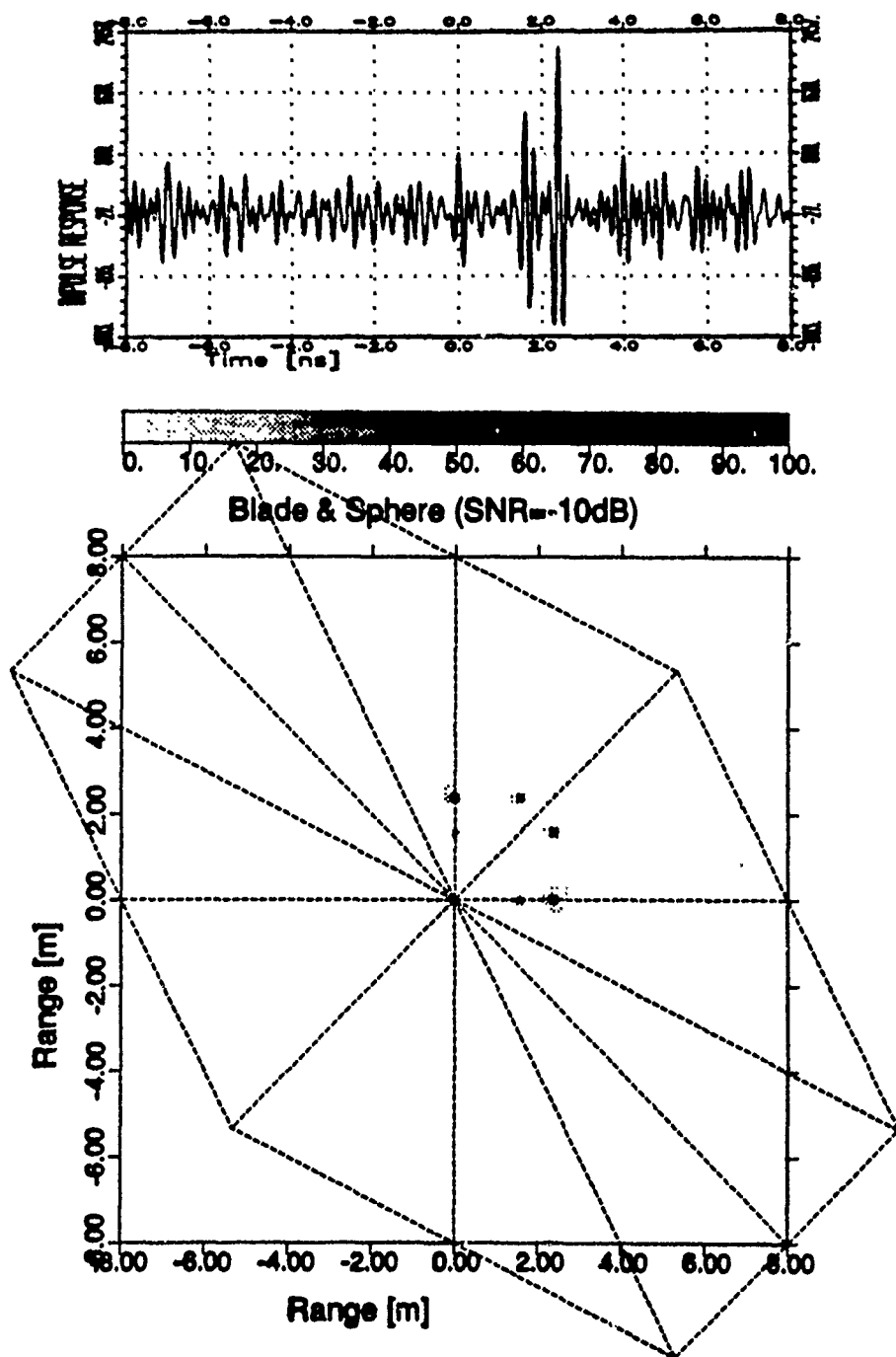
Figure 3.21: Transient response and birange profile of the three-point synthesized target of example # 1 at SNR= -10 dB.

signal (for infinite sequence of data) is given as

$$R^{H'}(f_1, f_2) = E\{H'^*(f)H'(f + f_1)H'(f + f_2)\}$$
$$= R^H(f_1, f_2) + R^C(f_1, f_2).$$

Thus, the effect of non-Gaussian noise on the bispectral response of a zero mean signal is represented by $R^C(f_1, f_2)$, which is dependent on the third moment of C. Non-Gaussian disturbances (such as ground clutter) often have non-zero first and third order moments [17]. For this reason, additive non-Gaussian noise is not suppressed in the birange even for an infinite number of samples.

For a finite data sequence, following the same derivations as in the Gaussian noise case, the effect of additive non-Gaussian noise on the triple correlation can be quantified as

$$E\{R^{H'}(f_1, f_2) - R^H(f_1, f_2)\}^2 = \qquad (3.49)$$
$$\frac{1}{N}\left[9a^2 E\{C\}^2 + 9a E\{C^4\} + 6a E\{C\}E\{C^3\} + N E\{C^6\}\right]$$

where $a = r^H(0)$. Notice that if $N \to \infty$ the mean square error between noisy and noiseless triple correlations approaches $E\{C^6\}$. Also, because $E\{C\} \neq 0$, and $E\{C^3\} \neq 0$, the term $6a E\{C\}E\{C^3\}$ contributes to the mean square error. However, this result does not imply that classification of radar targets in noisy environment (where the noise is non-Gaussian) based on features extracted from the birange produces poor performance compared to using other target representations. The reason is that non-Gaussian noise has similar effects on other types of display of target features.

3.8 Summary

The birange profile of radar signatures was introduced in this chapter. The definition of the birange as a display of target signatures in the two-

105

dimensional time domain is based on the bispectrum. The introduction of the birange to radar signature analysis is motivated by the interest in identifying multiple interactions, thus achieving a more accurate description of the target scattering subcomponents and enhancing the target identification process. The birange of radar signatures, as defined in this chapter, is based on a scattering model platform that includes specular scattering and multiple interactions. The model used is a sum of complex exponentials at frequencies related to the locations of scattering centers along the target.

The estimation of the birange is slightly different from conventional bispectral estimation techniques. Details of an estimation algorithm are given in this chapter. Also, the interpretation of the responses in the birange is presented using two examples of synthesized targets. Means for detecting false interactions in the birange profile are also discussed. Further, the effect of unmodeled dynamics in the backscattered signal on the birange is investigated.

The application of the birange profile as a radar signature analysis technique is first examined using experimental radar returns for a canonical object with somewhat known scattering behavior. Then the birange profiles of experimental radar returns from a generic aircraft model (with removable parts) are investigated. The detected responses in the birange profile of several configurations of the parts of this aircraft are associated with the geometry of the aircraft.

The birange profiles of experimental radar returns from real aircraft models at different frequency bands are also examined in terms of the detected interactions and the geometry of the targets. Also, a feature extraction algorithm to estimate the location of the interactions in the birange profile is given. This algorithm is used to provide tabulated features extracted from both the transient response and the birange. The extracted

features can be used to identify radar targets using structural pattern recognition algorithms without requiring large memory space. Finally, the effect of additive Gaussian and non-Gaussian noise on the birange, when estimated using either finite or infinite data sequences is investigated.

Chapter 4

BIRANGE ESTIMATION USING AUTOREGRESSIVE MODELING

4.1 Introduction

This chapter is con. rned with the estimation of high resolution birange profiles. The birange p. le of radar signatures as introduced in the previous chapter is estimated using classical Fourier transform techniques. The resolution of the estimated profiles is limited by the measurement bandwidth. Furthermore, the two-dimensional window function used in Chapter III has a wide mainlobe, which further limits the resolution in the birange. If the birange is estimated without windowing the triple correlation, then two-dimensional sidelobes will appear along each range axis. Therefore, with finite sets of radar scattering data, resolution problems in the birange when estimated using Fourier techniques are inevitable.

The key to solving the resolution problem is in avoiding the limitations imposed by Fourier-based processing of finite length data records. Instead, parametric modeling of the scattering data is employed. "Parametric" means that scattering as a function of frequency satisfies a certain model whose parameters are estimated from the measured data. The main

advantage of parametrization is the removal of the effect of limited resolution, thus providing higher resolution than can be obtained with Fourier transform based methods. The limitations of parametrization arise because: 1) electromagnetic scattering at frequencies outside the measurements cannot be easily predicted from the measured data, but depends on many factors such as dispersion, scattering region, etc., and 2) model parameters are often estimated using nonlinear algorithms, and thus, are sensitive to noise in the data. If the measured backscatter has a high signal-to-noise ratio and the target has a slowly varying frequency response, then these limitations are small, and significant resolution improvements over Fourier methods can be achieved.

Parametric modeling of radar signatures has been treated extensively in the literature [5,7,8]. A brief summary of the algorithms used and the results obtained is given in Chapter II. The methods used are based on AR, ARMA, MUSIC, and Prony spectral estimation techniques. While the ARMA methods ignore any prior information about the target scattering data, the MUSIC algorithm and the Prony method incorporate the *a priori* known exponential nature of the radar scattering data as modeled in (3.15). The consideration of these parametric methods is motivated by the interest in obtaining high resolution impulse responses.

There has been much recent interest in high resolution bispectral estimation [11]. The routes that are being followed to achieve high resolution bispectra can be classified into four categories: 1) maximum likelihood bispectral estimation, 2) maximum entropy bispectral estimation 3) AR, MA, and ARMA modeling, and 4) harmonic decomposition methods (MUSIC, etc..). Partial results have been obtained for the first two categories [11,24,34], but those remain open problems. It is not yet clear whether high resolution bispectral estimation methods that are based on a maxi-

mum likelihood approach or on maximizing the entropy of the data can be found. Unlike spectral estimation methods, bispectra estimated using AR modeling are not linked to either maximum entropy or maximum likelihood bispectra [11]. Hence, it is not possible to deduce one from the other. Most of the recent results on high resolution bispectral estimation are based on autoregressive (AR), moving average (MA), and autoregressive moving average (ARMA) modeling techniques, and on harmonic decomposition methods. In [30], a method based on the MUSIC algorithm and incorporating triple correlations is proposed for high resolution bispectral estimation purposes.

The estimation of the model parameters is in some cases related to the order of polyspectra under investigation. For example, when the spectral response is needed, the model parameters are estimated using autocorrelations or both triple correlations and autocorrelations. But when the bispectral response is needed the model parameters are estimated using triple correlations only.

In this chapter, an algorithm that adopts AR parametric modeling approach, where the AR parameters can be estimated using third order cumulants, is devised and tested using experimental radar data. The goals are: 1) to attempt to improve the accuracy of the extracted multiple interactions from the birange profile, and 2) to obtain encoded birange profiles of the targets of interest in terms of the model parameters. The purpose of the present investigation is to investigate whether AR modeling can be used to generate high resolution birange profiles. The quality of the obtained birange profiles is examined. The reason for discussing AR modeling in particular is that the techniques used to estimate the AR parameters depend on the order of the polyspectral response sought. Incorporating third order cumulants into the estimation procedure is a major feature of the

110

estimation algorithms.

4.2 Birange Estimation Algorithm Using AR Modeling

Autoregressive modeling of radar signatures has physical basis related to the nature of scattering data. Based on the exponential scattering model of (3.15), the measured backscatter at frequency f_k, denoted by $H(f_k)$, can be modeled as

$$H(f_k) = -\sum_{i=1}^{p} a_i H(f_{k-i}) + e(f_k) \tag{4.1}$$

where $e(f_k)$ is zero mean white noise with third order moment β, and p indicates the model order assumed to be chosen *a priori*. The AR system that models the birange is assumed to be driven by white non-Gaussian noise. The noise must be non-Gaussian noise because otherwise the bispectrum of the output is zero. The parameters $\{a_i\}$ are the AR parameters and can be estimated from second or third order cumulants of the data sequence $\{H(f_k)\}$.

The inverse Z transform of $H(f_k)$, $h(t)$ is the target impulse response. Therefore, the impulse response of a radar target whose backscatter satisfies (4.1) can be expressed as [8]

$$h(t) = \frac{1}{1 + \sum_{n=1}^{P} a_n \exp\{-jn\pi(1 - 2t/T)\}} \\ \sum_{i=1}^{P} \frac{c_i}{\exp\{j\pi(1 - 2t/T)\} - p_i} \tag{4.2}$$

where $T = 1/\Delta f$, and p_i, c_i are the partial fraction expansion coefficients.

The estimation of the birange profile using AR modeling is based on the definition of the bispectrum using the Cramer spectral representation (2.12). The birange $B(t_1, t_2)$ is given as

$$B(t_1, t_2) = h(t_1) h(t_2) h^*(t_1 + t_2) \tag{4.3}$$

111

Using (4.3), the birange is estimated as

$$B(t_1, t_2) =$$

$$\frac{\beta}{\sum_{k,l,m=0}^{P} a_k a_l a_m^* \exp\left\{j 2\pi [k(1 - \frac{2t_1}{T}) + l(1 - \frac{2t_2}{T}) - m(1 - \frac{2(t_1+t_2)}{T})]\right\}} \qquad (4.4)$$

Hence, the birange is parameterized by the AR coefficients $\{a_i\}$. These coefficients are to be estimated from the cumulants or estimates of the cumulants. The above method for estimating the birange profile using an AR model has the following disadvantage: the birange as given in (4.3) is a transformation of the impulse response from a one-dimensional profile into a two-dimensional profile. For example, a single peak at t_k in the impulse response is mapped into three straight lines in the birange profile where these straight lines satisfy $\{t_1 + t_2 = t_k, \ t_1 - t_2 = t_k, \ t_2 - t_1 = t_k\}$ because by substituting the magnitude of the impulse response at these points in (4.3) a birange peak of large magnitude (approaches infinity) is obtained. A true peak in the birange profile, however, is the result of three peaks in the impulse response at t_i, t_j, and $t_k = t_i + t_j$, and all three peaks have relatively large magnitudes.

AR Parameters Estimation Methods

There are several methods that can be used for the estimation of the AR parameters from the cumulants of the data [27,28]. The following relation is the basis for estimation,

$$\sum_{i=0}^{p} a_i R(i-m, i-n) = 0 \quad \forall \ m, n \qquad (4.5)$$

where the triple correlation is defined as

$$R(m, n) = E\{H^*(k)H(k+m)H(k+n)\}. \qquad (4.6)$$

The above relation is easily derived [42] by multiplying both sides of (4.1) by $H^*(f_k - f_m)H^*(f_k - f_n)$, and taking the expected values. The relation

112

given by (4.5) defines an overdetermined set of equations that can be used to solve for the $\{a_i\}$ coefficients.

The estimation of the AR coefficients $\{a_i\}$ is a prerequisite for estimating the birange profile. The algorithms used in this study for estimating the birange (based on the methods given in [27,28,32,42]) are the following:

Algorithm # 1: Estimate the triple correlation $R(m,n)$, $m, n = 0, \ldots$, of the measured data $H(f_k)$ then substitute in

$$\begin{bmatrix} R(0,0) & R(1,1) & \cdots & R(p,p) \\ R(-1,-1) & R(0,0) & \cdots & R(p-1,p-1) \\ \cdot & & \cdot & \cdot \\ \cdot & \cdot & \cdot & \cdot \\ R(-p,-p) & R(-p+1,-p+1) & \cdots & R(0,0) \end{bmatrix} \begin{bmatrix} 1 \\ a_1 \\ \cdot \\ \cdot \\ a_p \end{bmatrix} = 0 \quad (4.7)$$

which can be denoted as,

$$\Re a = 0. \quad (4.8)$$

Notice that the entries in the matrix $\Re$ are chosen from only one slice ($R(m,m)$, $m = n$) of the cumulant plane.

Algorithm # 2: It is possible to choose entries that belong to many slices of the cumulant plane as given below

$$\begin{bmatrix} R(0,0) & R(1,1) & \cdots & R(p,p) \\ R(0,-1) & R(1,0) & \cdots & R(p,p-1) \\ \cdot & \cdot & \cdot & \cdot \\ R(0,-p) & R(1,1-p) & \cdots & R(p,0) \\ R(-1,0) & R(0,1) & \cdots & R(p-1,p) \\ \cdot & \cdot & \cdot & \cdot \\ R(-p,-p) & R(-p+1,-p+1) & \cdots & R(0,0) \end{bmatrix} \begin{bmatrix} 1 \\ a_1 \\ \cdot \\ \cdot \\ a_p \end{bmatrix} = 0 \quad (4.9)$$

where the $\{a_i\}_{i=1}^{p}$ are obtained by solving an overdetermined set of linear equations. In both algorithms the estimates of the birange at (t_1, t_2) are computed using (4.5).

Unlike using Yule-Walker equations to solve for the AR parameters (where the autocorrelation matrix is always full rank), the triple correlation matrix is not necessarily full rank, particularly for algorithm #1.

Estimates of the birange profile using AR modeling techniques exist if a full rank triple correlation matrix can be found. However, if a full rank triple correlation matrix exists under certain conditions, it is not guaranteed to remain full rank if the data conditions are changed (e.g., if the data are contaminated by noise) [11].

4.2.1 Difference Between Modeling Using Triple Correlations and Using Autocorrelations

In the previous section we developed algorithms which estimate the AR coefficients using third order cumulants. Alternatively, there are algorithms which estimate the AR coefficients of the same model (4.1) using second order cumulants only [8]. These two approaches represent different modeling philosophies, and below we discuss the differences between the two.

If the goal of the modeling procedure is to obtain parametric bispectral estimates then only the third order cumulants should be used to estimate the AR coefficients. The reason for not including second order cumulants is to avoid any responses that are not bicorrelated even when the wavenumber of one component is the sum of wavenumbers of two other components. If only second order cumulants are used to estimate the AR parameters, estimates of the target impulse response will be obtained, but the bicorrelation terms in the birange profile cannot be obtained. If the goal is to model the system including all time components (bicorrelated or not) then one can use both second and third order cumulants to estimate the AR parameters. Therefore, the system model that is derived using third order cumulants exhibits time components that are engaged only in bicorrelation, whereas the system model derived using second and third order cumulants combined exhibits all time components of the signal. In this chapter, we are concerned with modeling the birange profile, therefore we will use third order cumulants only.

114

As an example, let $h(t)$ be the inverse Fourier transform of $H(\omega)$ where $h(t)$ has eight responses only, i.e., $h(t) = \{h(t_i), \quad i = 1, \ldots, 8\}$, where $t_5 = t_3 + t_4$, and $t_8 = t_6 + t_7$. Assume also that the responses $\{h(t_3), h(t_4), h(t_5)\}$ are bicorrelated. If $H(\omega)$ is modeled using only third order cumulants then only the time components $h(t_3), h(t_4)$, and $h(t_5)$ are detected. Thus, the birange profile will have a peak at (t_3, t_4) and (t_4, t_3), and be zero elsewhere. However, if $H(\omega)$ is modeled using second order cumulants then all time components are detected. If the parametric bispectrum is generated using second and third order cumulants then it will include peaks at both (t_6, t_7) and at (t_3, t_4).

Notice that, while second order cumulants cannot be used to model the bispectrum, third order cumulants may be used to model the spectrum (Lii and Rosenblatt [78]) given that full rank cumulant slices exist.

4.2.2 Experimental Results

Blade-Sphere Example:

Algorithm # 1 of Section 4.2 was used to estimate the birange profile of the blade sphere target example of Chapter III. In this example, as in Chapter III, 1000 data points were used to estimate the birange profile. Specifically, from these 1000 data points we estimated the triple correlation $R(k, k)$ for $k = 0, \ldots, p$ using (4.6). We solved for the AR coefficients using (4.7). Finally, the birange profile was obtained using (4.4). Figure 4.1 shows the birange of the blade sphere target when estimated using an AR filter with complex coefficients of orders 10 and 12. This figure shows that the birange, as estimated using the above algorithm is sensitive to model order as indicated by the presence of spurious peaks (denoted by a, b, and c) in the birange when the model is increased from 10 to 12. The estimates of the coordinates of the interaction (see Table 4.1), however, are more accurate

115

when the birange is estimated using the above algorithm than using Fourier transform or even using Gaussian function fitting on the Fourier transform (compare Table 4.1 with Table 3.1). For this example, using more than a single slice (as in Algorithm # 2) to estimate the AR parameters has an insignificant effect on the birange estimate of this target.

Figure 4.2 shows both the impulse response and the birange profile of the blade sphere target using AR model of order 12. The purpose of Figure 4.2 is to show the correspondence between the impulse response and the birange of the blade-sphere target when both are obtained using AR modeling. Note that all the responses of the target are modeled in the impulse response.

Scaled Model Target Examples:

The triple correlation matrix given in Algorithm # 2 was used (in a least squares sense) to estimate the AR parameters and the birange profile for each of the five model aircraft discussed in Section 3.6.5. The data were decimated so that an unambiguous window of 6 nanoseconds is obtained, and the triple correlations used to obtain the AR parameters were estimated from the decimated data. The decimation rule followed is

$$H_d(f_k) = \frac{1}{4}(H(f_{k-1}) + 2H(f_k) + H(f_{k+1}))$$

where $H_d(f_k)$ is the decimated response at frequency f_k. A triple correlation lag of 21 data points was used. The data belong to the $1.5 - 12$ GHz frequency band with a frequency increment of 50 MHz. Algorithm # 1 was also used but found to give inferior results, and are not presented.

Figures 4.3-4.5 show the birange profiles for three commercial aircraft obtained using AR models of order 14 and using the Fourier transform; Figure 4.6 shows the impulse responses for three aircraft obtained using Fourier transform; and AR modeling. Notice that both the impulse responses and

116

the birange profiles obtained using AR models do not correlate well with those obtained using Fourier transform.

The difference in the impulse responses may be due to the fact that AR parameters estimated using triple correlations model the bispectrum (or birange) of the target and not its spectrum (or impulse response). We have tried several experiments using different model orders and using different triple correlation lags; we have also tried incorporating singular value decomposition into the AR parameter estimation process. The results in 4.3-4.5 represent the best results we could obtain using this algorithm. Figure 4.5 represents the most compatible and Figure 4.4 the least compatible fit between AR and Fourier birange profiles of the five targets. It is also clear from Figures 4.1-4.5 that the AR modeling algorithm given in this chapter can reproduce the Fourier-based birange profiles using synthesized data but has difficulty resolving closely spaced birange peaks using real radar data.

Figures 4.7 shows how the impulse response, that models the birange profile of the DC-10 aircraft, changes as a function of model order. Notice that, as the model order is increased, spurious peaks are obtained as shown in Figure 4.7. However, a spurious peak at time t_i in the impulse response does not always produce a spurious peak in the birange profile unless there are two other peaks (not necessarily spurious) at t_j, $t_i - t_j$, and $t_j - t_i$. Figure 4.8 shows the birange profile of the DC-10 aircraft using the same model orders as in Figure 4.7. Notice that, unlike the impulse response shown in Figure 4.7, increasing the model order does not always introduce spurious birange peaks (see the upper left plot in Figure 4.8 for AR(20)).

The parametric birange profiles obtained using third order cumulants assume that the data sequence is random with hidden bicorrelations. If we assume that the data is deterministic, then it is possible to model the signal

117

using second order cumulants or autocorrelations. In this case the Fourier-based birange profile can be obtained using $B(t_1, t_2) = h(t_1)h(t_2)h^*(t_1 + t_2)$ and the AR-based birange profiles can be obtained using Yule-Walker equations [60]. Figures 4.9-4.10 show the birange profile and the impulse response for the aircraft DC-10 obtained using Fourier transform and AR modeling and using the same data and the same decimation procedure as in the above experiments. These Figures show that when the data is assumed to be deterministic, the birange profiles obtained using the Fourier transform can be matched with higher resolution fidelity by AR based estimates using second order cumulants. The reason for the agreement between the Fourier-based birange profile and the AR birange profile is that both are directly estimated from from the impulse responses using (4.3) and there is an agreement between the impulse response obtained using Fourier transform and using the AR parameters. This experiment suggests that the difficulty in modeling the birange may be related to the fact that we are using the triple correlation of complex-valued data to estimate the AR parameters.

4.3   Discussion

The results obtained on modeling scaled model aircraft using the AR-based algorithm proposed in Section 4.2 are not encouraging in the sense that no closely spaced peaks in the birange are resolved and little compatibility between Fourier-based birange profiles and AR-based birange profiles is observed. This lead us to investigate certain modeling aspects related to the type of scattering data that we are trying to model.

One of the key issues of the AR modeling procedure adopted in this Chapter is that the radar scattering data are complex-valued. Unlike modeling the spectral responses of complex-valued signals, there seems to be

a significant difference between modeling real-valued and complex-valued data. This difference is explained by the following theorems where complex exponential signals with implicit bicorrelations are used as examples of complex-valued data. The following theorems show that parameters of an AR model of a certain order can be found such that they uniquely satisfy equation (4.8) and yet they cannot be used to model the true bispectrum of the complex-valued signal. Thus, these theorems suggest other possible reasons for discouraging AR modeling results.

4.3.1 On AR Modeling of Complex-Valued Signals

The estimation of the bispectrum using AR modeling requires the choice of the model order. The model order is dependent on the number of peaks in the bispectral response. If real-valued data is used and the birange has I peaks in one symmetry sector, then the number of peaks in the impulse response that models the birange is upper bounded by $3I$, which corresponds to a model order of $6I$ (assuming real AR coefficients). This result has been shown in [42] when modeling real-valued sinusoids with implicit bicorrelations.

Modeling complex-valued signals requires a different approach from that used to model real-valued signals. The following theorems explain the modeling aspect of complex-valued signals (complex exponentials used as an example of complex-valued signals) and the model order needed. These theorems show a fundamental difference between modeling real-valued signals and complex-valued signals.

Theorem 4.1: *Let $H(\omega)$ be of the following form*

$$H(\omega) = \sum_{i=1}^{I} [\exp\{j(\omega t_{ai} + \theta_{ai})\}$$
$$+ \exp\{j(\omega t_{bi} + \theta_{bi})\} + \exp\{j(\omega(t_{ai} + t_{bi}) + \theta_{ai} + \theta_{bi})\}] \quad (4.10)$$

where θ_{ai}, θ_{bi} are uniformly distributed random variables over $[0, 2\pi]$. Note

that $H(\omega)$ includes I implicit couplings as indicated by the third component of (4.10). There is a unique set of complex AR coefficients $\{a_n\}_{n=0}^{I}$, with $a_0 = 1$, such that

$$\sum_{n=0}^{I} a_n R_H(n - k, n - l) = 0. \tag{4.11}$$

However, when this set of AR coefficients is used in (4.2) and (4.3), the result is in general not the true birange profile.

Proof: The triple correlation of $H(\omega)$ is given as (replacing ω_1, and ω_2 by k and l respectively.

$$R_H(k, l) = \sum_{i=1}^{I} [\exp\{j(kt_{ai} + lt_{bi})\} + \exp\{j(kt_{bi} + lt_{ai})\}]. \tag{4.12}$$

and the birange profile is

$$B_H(t_1, t_2) = \sum_{i=1}^{I} [\delta(t_1 - t_{ai}, t_2 - t_{bi}) + \delta(t_1 - t_{bi}, t_2 - t_{ai})] \tag{4.13}$$

Then,

$$\sum_{n=0}^{I} a_n R_H(n - k, n - l) =$$

$$\sum_{n=0}^{I} \sum_{i=1}^{I} [a_n \{\exp\{j(t_{ai}(n - k) + t_{bi}(n - l))\}$$

$$+ \exp\{j(t_{bi}(n - k) + t_{ai}(n - l))\}\}] \tag{4.14}$$

$$= \sum_{i=1}^{I} [(\exp\{-j(t_{ai}k + t_{bi}l)\}$$

$$+ \exp\{-j(t_{ai}l + t_{bi}k)\}) \sum_{n=0}^{I} a_n \exp\{j(t_{ai} + t_{bi})n\}]$$

This expression is zero if and only if (see [60]) the AR parameters $\{a_i\}$ satisfy

$$\sum_{n=1}^{I} a_n z^n = \prod_{i=1}^{I} (z - \exp\{j(t_{ai} + t_{bi})\}) \tag{4.15}$$

Therefore, it is sufficient to choose a model of order I to model I responses in the bispectrum. The impulse response obtained using these AR parameters

has I peaks at $t_{ai} + t_{bi}$, $i = 1, \ldots, I$, and is given as (using equation (4.2))

$$h(t) = \sum_{i=1}^{I} \frac{c_i}{\exp\{j\pi(1 - 2t/T)\} - \exp\{j\pi(1 - 2(t_{ai} + t_{bi}))/T\}} \tag{4.16}$$

Then the birange is obtained using (4.3) as

$$B(t_1, t_2) = \left(\sum_{i=1}^{I} \frac{c_i}{\exp\{j\pi(1 - 2t_1/T)\} - \exp\{j\pi(1 - 2(t_{ai} + t_{bi}))/T\}} \right)$$

$$\left(\sum_{i=1}^{I} \frac{c_i}{\exp\{j\pi(1 - 2t_2/T)\} - \exp\{j\pi(1 - 2(t_{ai} + t_{bi}))/T\}} \right)$$

$$\left(\sum_{i=1}^{I} \frac{c_i^*}{\exp\{-j\pi(1 - 2(t_1 + t_2)/T)\} - \exp\{-j\pi(1 - 2(t_{ai} + t_{bi}))/T\}} \right)$$

The birange shows a peak at (t_j, t_k) when either t_j, t_k, or $t_j + t_k$ is equal to $t_{ai} + t_{bi}$. For example, if $h(t_j) = \alpha$, $h(t_k) = \beta$, (where $\alpha, \beta \neq 0$, for an all-pole model) and $h(t_j + t_k) = \gamma$ where $\lim_{t_j + t_k \to t_{ai} + t_{bi}}\{\gamma\} \to \infty$, and $(t_j + t_k = t_{ai} + t_{bi}), i = 1, \ldots, I$, then the birange at (t_j, t_k) is given as such

$$\lim_{t_j + t_k \to t_{ai} + t_{bi}} \{B(t_j, t_k)\} \to \infty \tag{4.17}$$

Similarly, (4.17) holds $\forall t_j, t_k \ni t_j + t_k = t_{ai} + t_{bi}$, $t_j - t_k = t_{ai} + t_{bi}$, or $t_k - t_j = t_{ai} + t_{bi}$. Note that the true birange peak at (t_{ai}, t_{bi}) belongs to the straight line defined by $\{t_1 + t_2 = t_{ai} + t_{bi}\}$, however the magnitude of this peak is comparable to the other peaks along the same line and cannot be distinguished from the others. The only birange profile that can be modeled correctly corresponds to the case where $t_{ai} = t_{bi} = 0$, since in this case $\lim_{t_1, t_2 \to 0}\{B(t_1, t_2)\} \to (\infty)(\infty)(\infty)$.

Q.E.D.

Theorem 4.2: *Let $H(\omega)$ be of the following form*

$$H(\omega) = \sum_{i=1}^{I} [\exp\{j(\omega t_{ai} + \theta_{ai})\}$$
$$+ \exp\{j(\omega t_{bi} + \theta_{bi})\} + \exp\{j(\omega(t_{ai} + t_{bi}) + \theta_{ai} + \theta_{bi})\}] \tag{4.18}$$

where θ_{ai}, θ_{bi} are uniformly distributed random variables over $[0, 2\pi]$. Then, there is a unique set of complex AR coefficients $\{a_n\}_{n=0}^{3I}$, with $a_0 = 1$, such

121

that

$$\sum_{n=0}^{3I} a_n R_H^c(n-k, n-l) = 0. \tag{4.19}$$

where

$$
\begin{aligned}
R_H^c(k,l) = \ & E\{H^*(n)H(n+k)H(n+l) \\
& + H(n)H^*(n+k)H(n+l) + H(n)H(n+k)H^*(n+l) \} \tag{4.20}
\end{aligned}
$$

These parameters uniquely model the true birange profile.

Proof: Using (4.20), the third order cumulant of the signal in (4.18) is

$$
\begin{aligned}
R_H^c(k,l) = \ & \sum_{i=1}^{3I} [\exp\{j(kt_{ai} + lt_{bi})\} + \exp\{j(kt_{bi} + lt_{ai})\} \\
& + \exp\{j(k(t_{ai}+t_{bi}) + lt_{bi})\} + \exp\{j(kt_{bi} + l(t_{ai}+t_{bi}))\} \\
& + \exp\{j(k(t_{ai}+t_{bi}) + lt_{ai})\} + \exp\{j(kt_{ai} + l(t_{ai}+t_{bi}))\}] \tag{4.21}
\end{aligned}
$$

The proof then follows similar to that in [42] for real sinusoidal signals with I couplings. The impulse response is then given as

$$
\begin{aligned}
h(t) = \sum_{i=1}^{I} \Big[& \frac{c_{i1}}{\exp\{j\pi(1-2t/T)\} - \exp\{j\pi(1-2(t_{ai}+t_{bi})/T\}} + \\
& \frac{c_{i2}}{\exp\{j\pi(1-2t/T)\} - \exp\{j\pi(1-2(t_{ai})/T\}} + \\
& \frac{c_{i3}}{\exp\{j\pi(1-2t/T)\} - \exp\{j\pi(1-2(t_{bi})/T\}} \Big]
\end{aligned}
$$

where $c_{ij} \neq 0$, $j = 1,2,3$. The birange is then obtained using (4.3). Using this model, all responses at t_{ai}, t_{bi}, and $t_{ai}+t_{bi}$, $i = 1,\ldots,I$ are modeled in the impulse response and each set of $\{t_{ai}, t_{bi}, t_{ai}+t_{bi}\}$ in the impulse response produces a single peak in the birange such as

$$\lim_{t_1, t_2 \to t_{ai}, t_{bi}} \{B(t_1, t_2)\} \to (\infty)(\infty)(\infty) \tag{4.22}$$

This peak can be easily distinguished from other peaks that are obtained because of the transformation of (4.3). Q.E.D.

We have shown in Theorem 4.1 (using AR modeling of complex exponentials) that although it is possible to obtain AR parameters that satisfy

(4.8), the derived system does not necessarily model the the true bispectrum. Theorem 4.2 presents an alternative approach to modeling complex exponentials. The parameters obtained as described in Theorem 4.2 model uniquely the true bispectrum of complex exponentials. Theorem 4.2, however, cannot be used to model all types of complex-valued signals, including radar signals, but suggests that modeling complex-valued time series, using third order cumulants, may differ significantly from modeling real time series. The reason that we cannot use (4.20) to model radar signals is twofold: 1) the electric phase ψ modeled in (3.15) is not uniformly distributed over $[0, 2\pi]$ (however, we may assume so for mathematical reasons), and 2) the model of (3.15) corresponds to point target scatterers and may not be appropriate to model real aircraft targets. The reason that the birange of the blade-sphere target model was recovered using third order cumulants-based AR modeling is because scattering from the model is deterministic with a response at zero time.

Another aspect of modeling radar target responses is related to the estimation procedure adopted in this study. Modeling the bicorrelated responses in the impulse response and then transforming the obtained impulse response into a two-dimensional profile (the birange profile) produces ridges that are formed by straight lines in the birange profile. These straight lines do not belong to the birange profile but are the consequence of transformation from an all-pole impulse response into the birange profile. From the outcomes of the experimental study and using such an argument, we conclude that modeling the birange profiles of radar scattering data may benefit by using a two-dimensional AR model that models third order cumulants directly instead of the one-dimensional modeling procedure (also based on third order cumulants) adopted in this study.

123

4.4 Summary

The purpose of this chapter is to devise and test an algorithm that can be used to obtain high resolution birange profiles by modeling the measured frequency response using AR models. It is shown that the AR model needed to estimate the birange may differ from the AR model needed to estimate the impulse response. Algorithms based on third order cumulants of the measured data were used to obtain experimental birange profiles for different model orders. The AR birange profiles were then compared to the Fourier transform based birange estimates. The results obtained are not encouraging as indicated by the incompatability of Fourier-based birange profiles and the AR-based birange profiles. This lead us to further investigate the properties of (triple correlation)-based AR modeling of complex-valued radar signals. The results of this investigation indicate that modeling complex-valued exponential signals using third order cumulants does not result in the true birange profile and a slightly different modeling strategy is required. Even when the birange is modeled correctly, the estimated birange profile from the impulse response exhibits false birange peaks that belong to straight lines in the two-dimensional birange plane. Such a disadvantage may be avoided by using a two-dimensional AR model that is based directly on the third order cumulants. Henceforth, the modeling aspect of the two-dimensional birange profiles that are estimated from complex-valued signals remains an open research area.
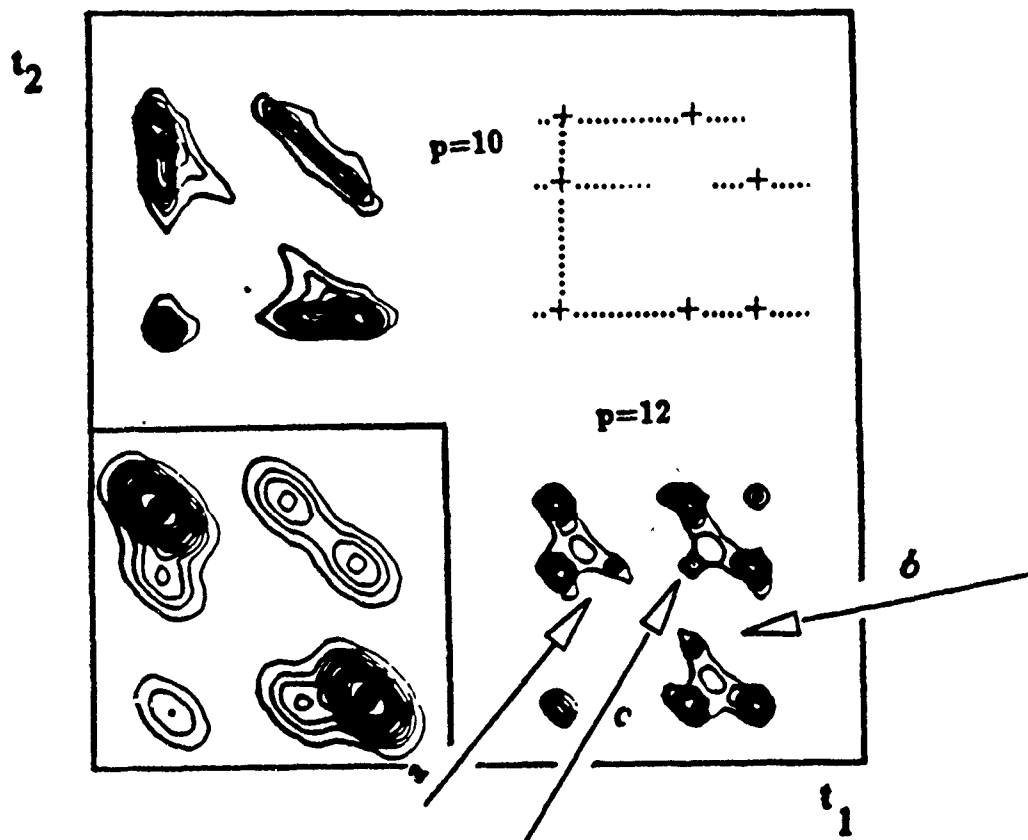
Figure 4.1: Birange profile for the blade-sphere target using AR modeling based on third order cumulants for models of order 10 and 12 (for comparison, the box in the lower left shows the birange profile generated by Fourier transform, and the box in the upper right corner shows the true location of birange responses).

125
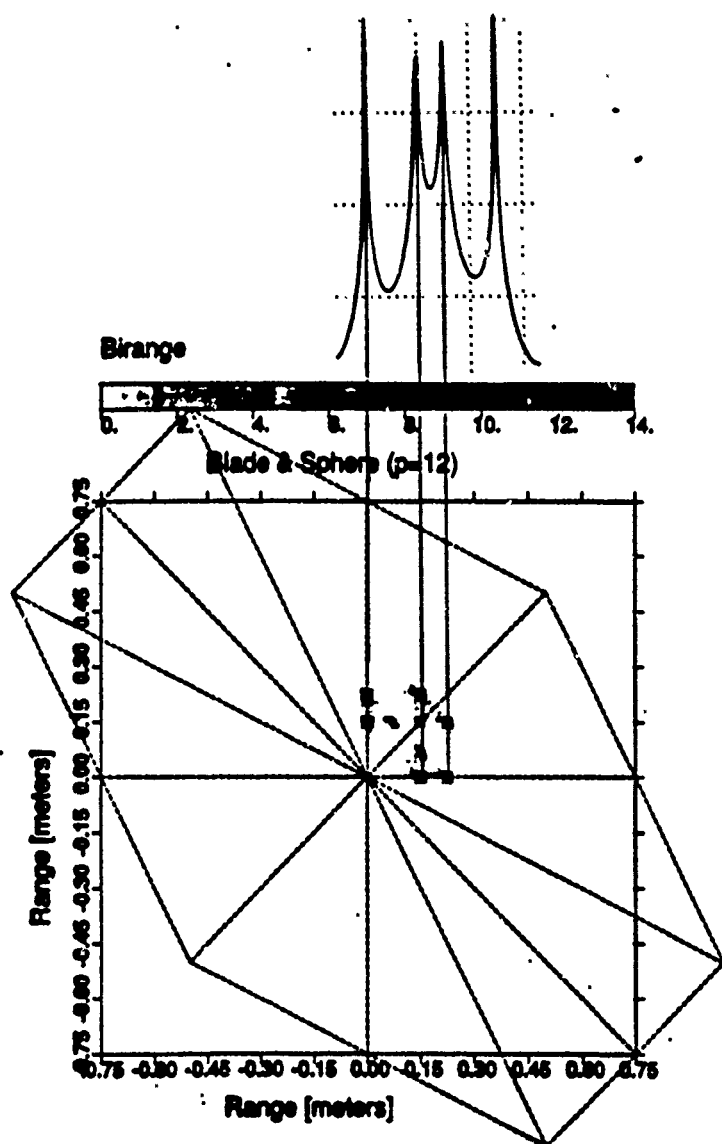
Figure 4.2: Impulse Response and Birange profile for the blade-sphere target using an AR model of order 12 (based on third order cumulants).
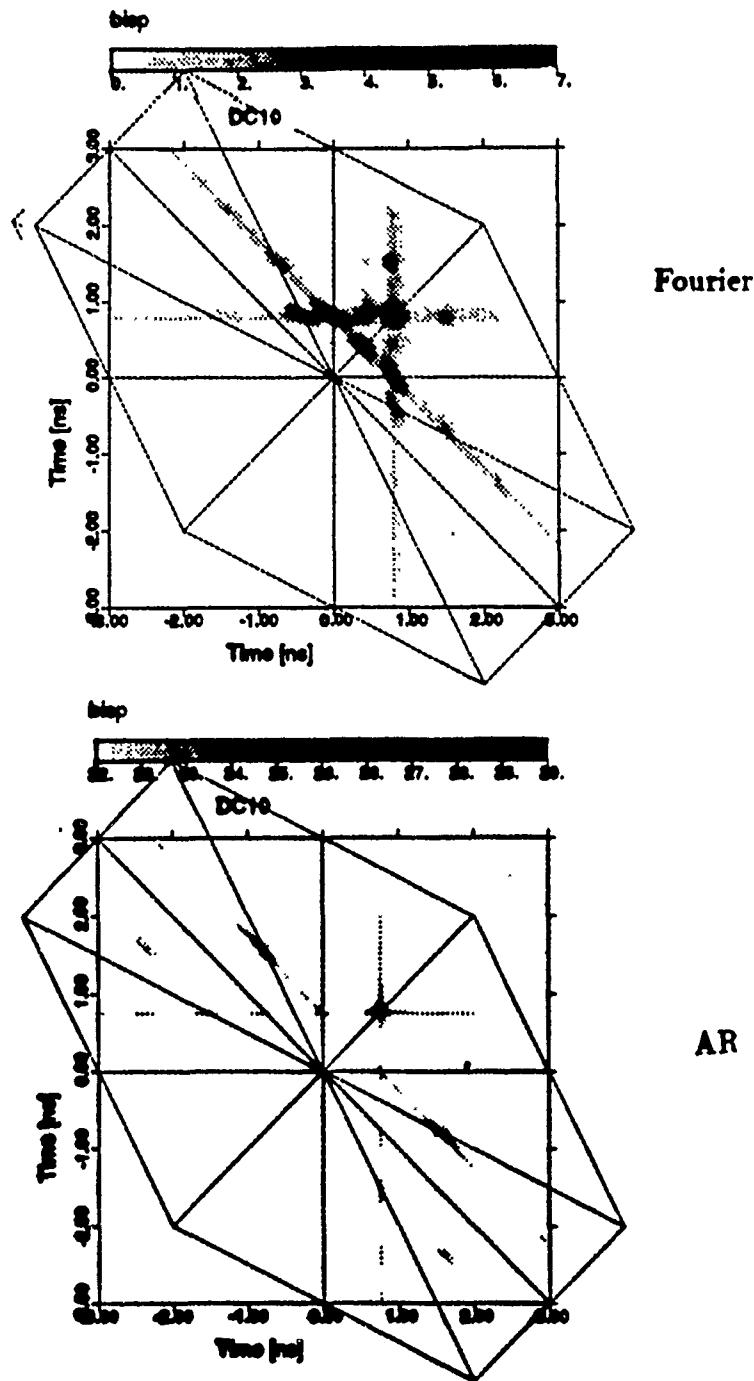
Figure 4.3: Birange profile for DC-10 using Fourier transform and AR model of order 14 (based on third order cumulants).

127
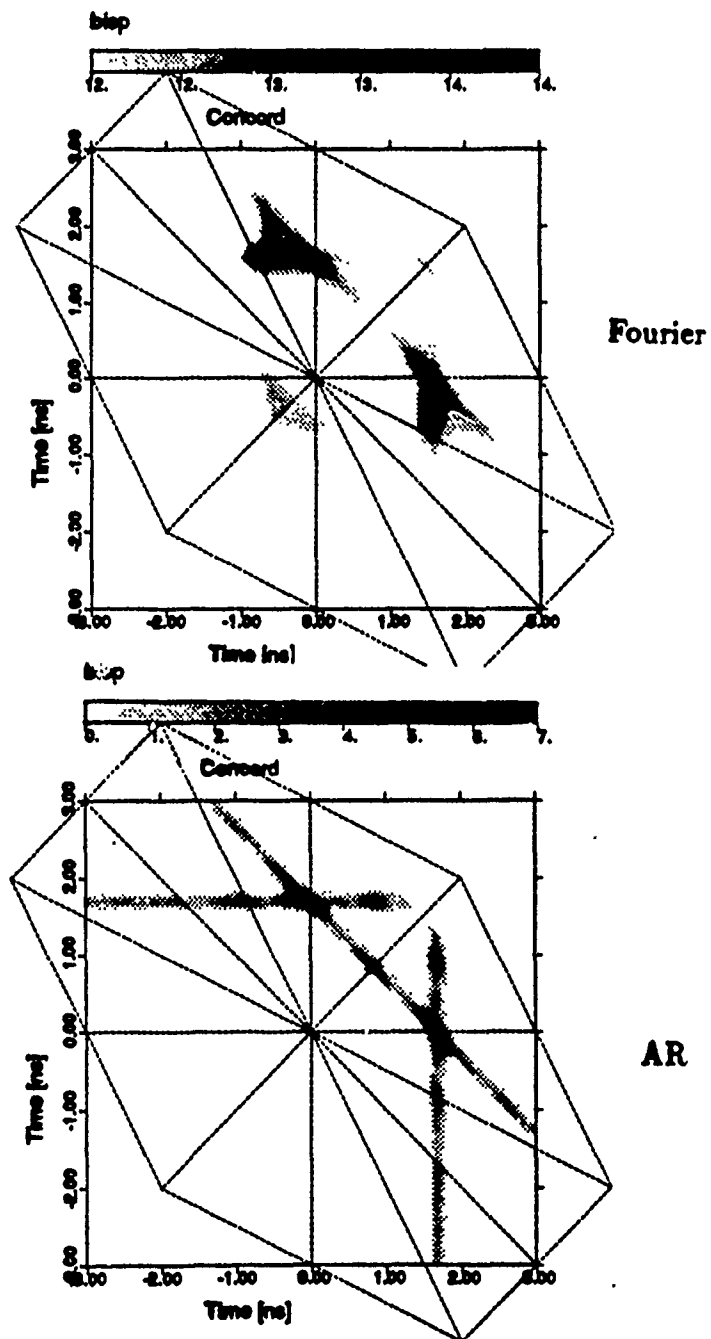
Figure 4.4: Birange profile for the Concord aircraft using Fourier transform and AR model of order 14 (based on third order cumulants).

128
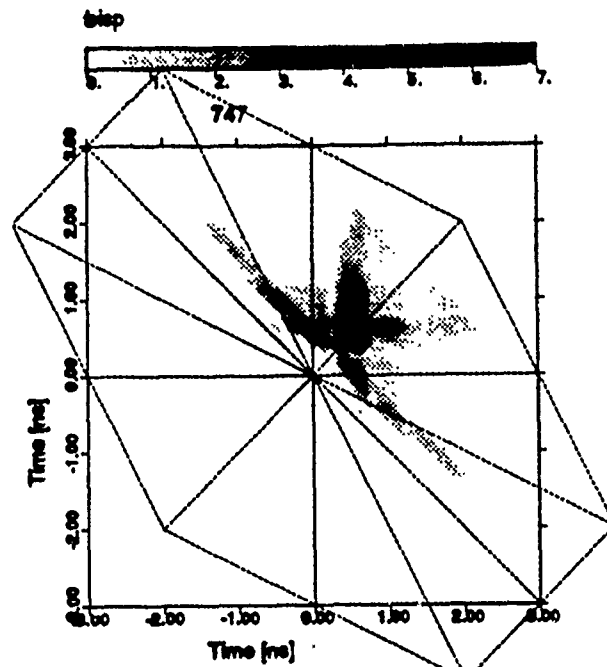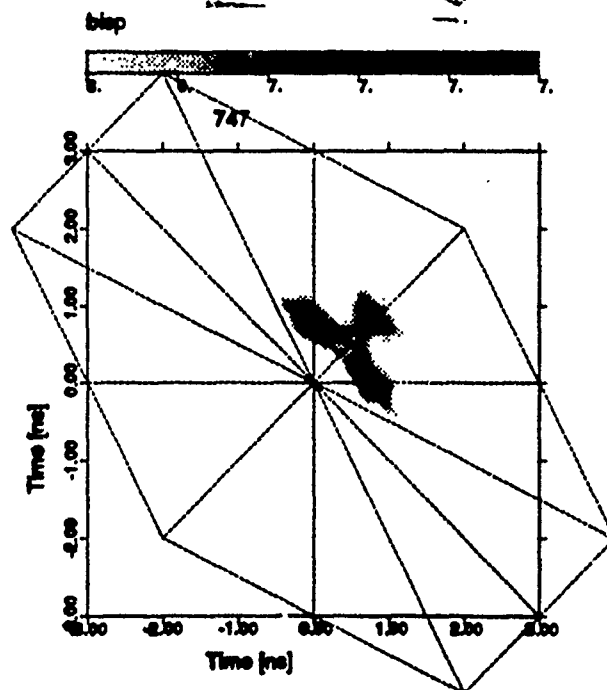
Figure 4.5: Birange profile for Boeing 747 using Fourier transform and AR model of order 14 (based on third order cumulants).
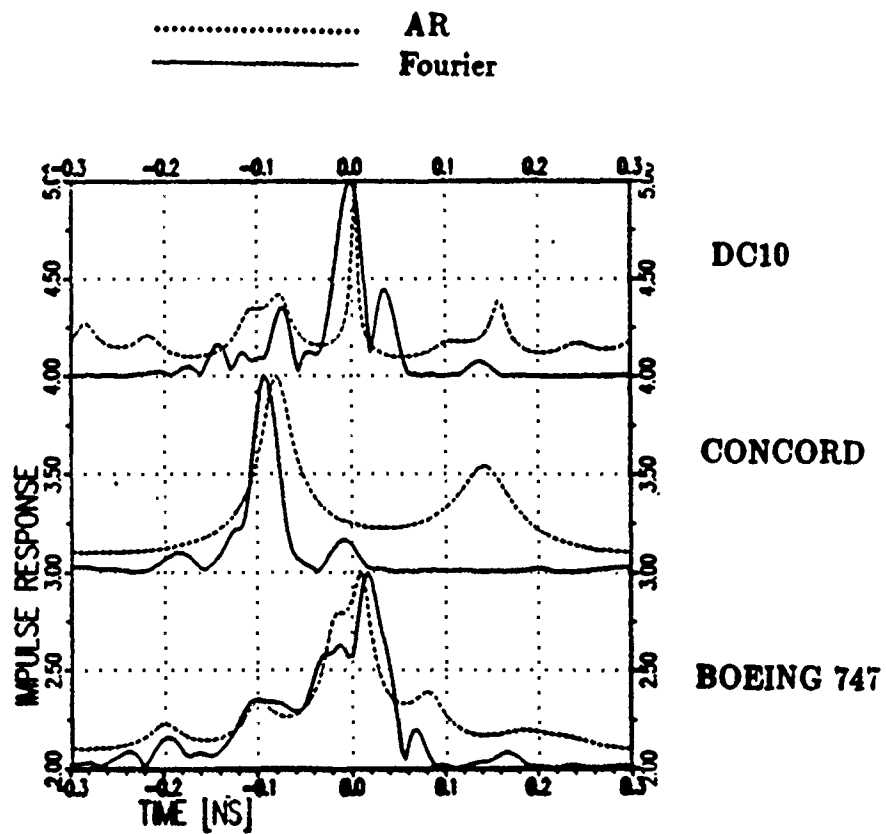
Figure 4.6: Impulse response for three commercial aircraft using Fourier transform and AR model of order 14 (based on third order cumulants).

130

AR(20)

AR(16)

AR(12)

AR(8)
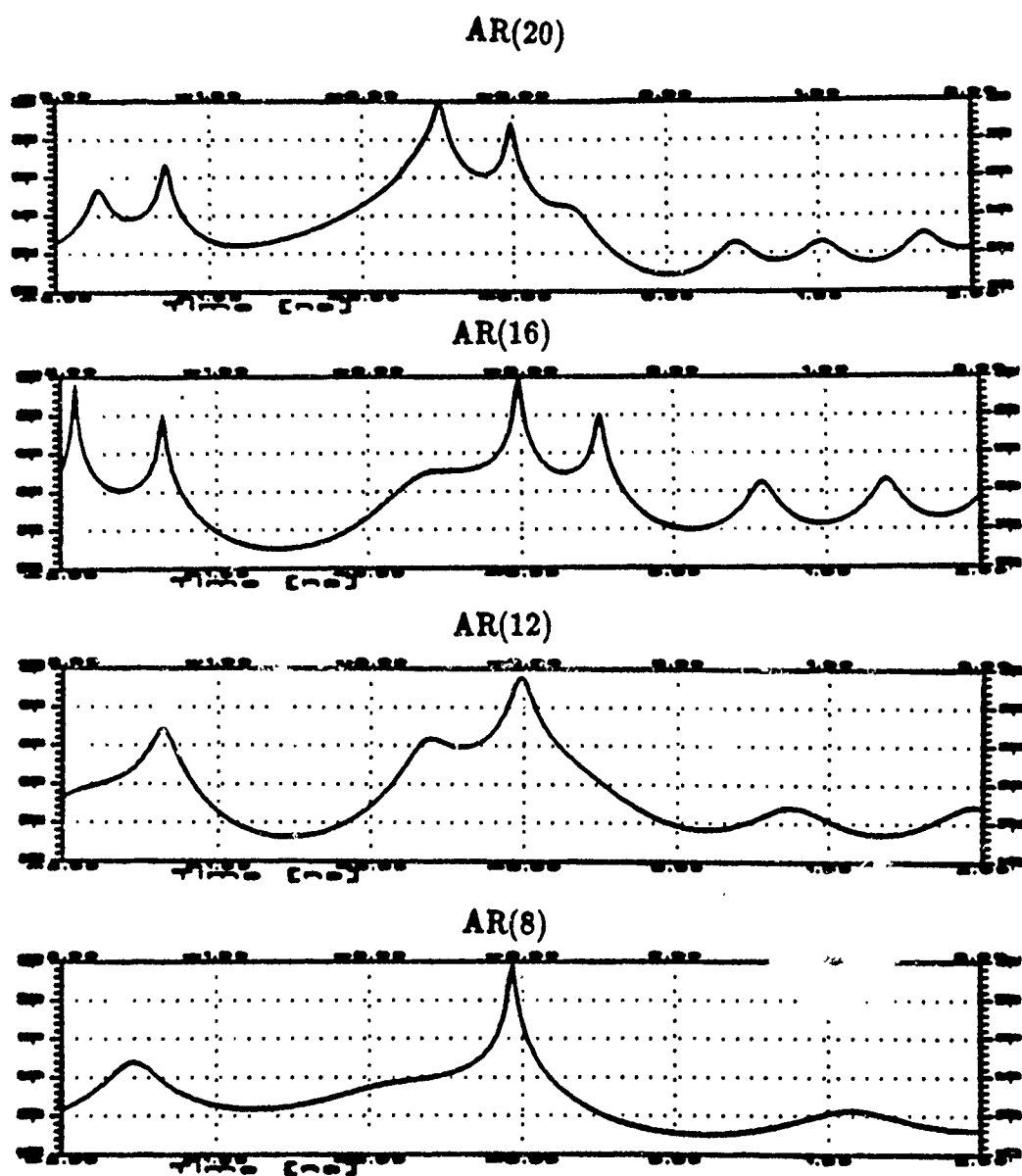
Figure 4.7: Impulse response for DC-10 aircraft using AR models (based on third order cumulants) of different orders.

131
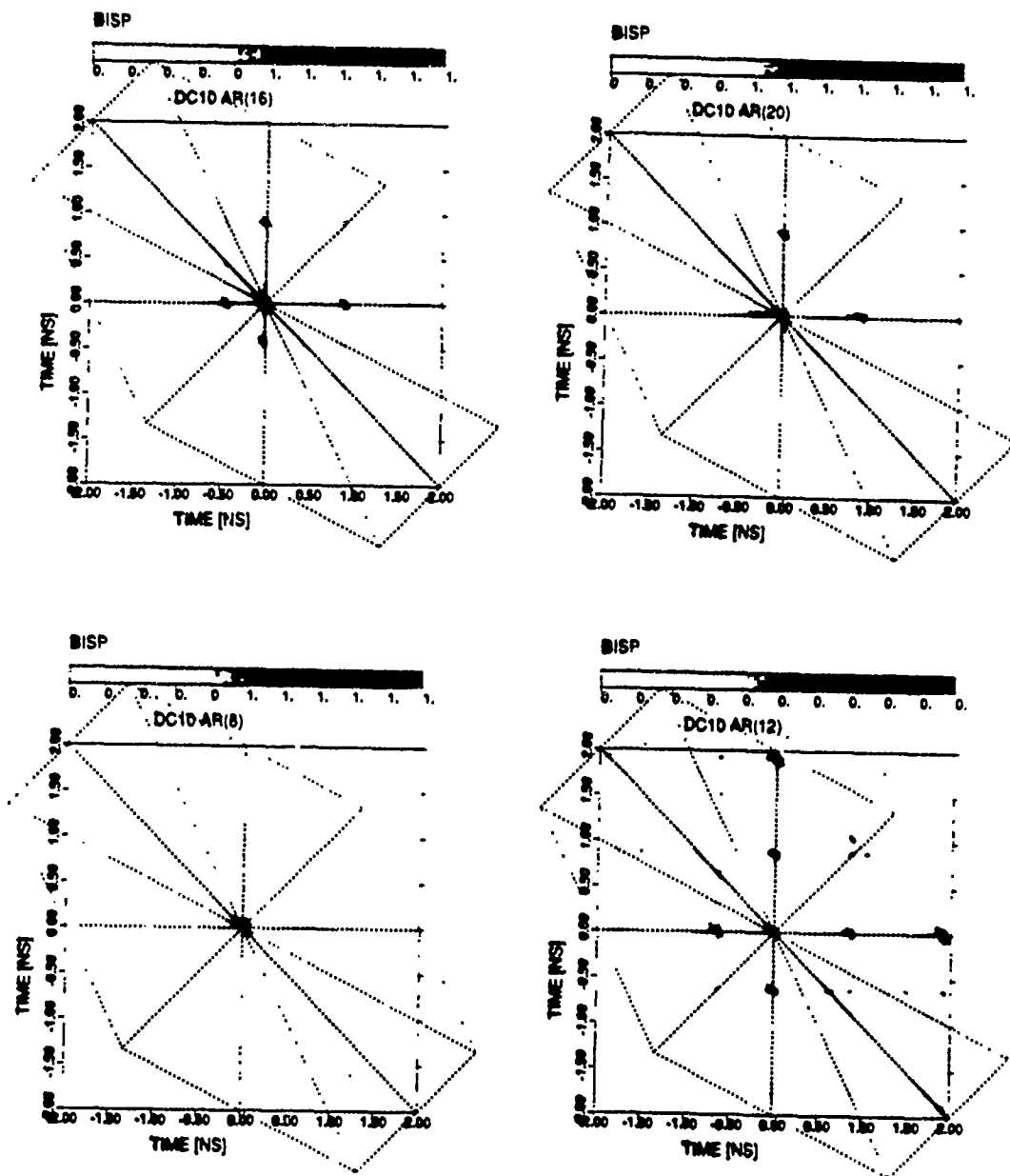
Figure 4.8: Birange profiles for DC-10 aircraft using AR models (based on third order cumulants) of different orders.
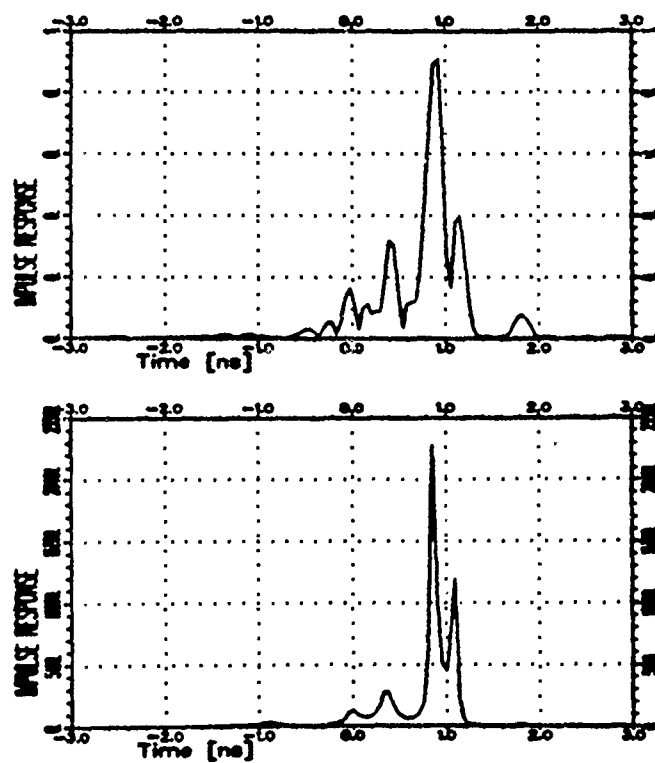
Figure 4.9: Impulse response for the DC-10 obtained using Fourier transform and AR modeling (based on second order cumulants).
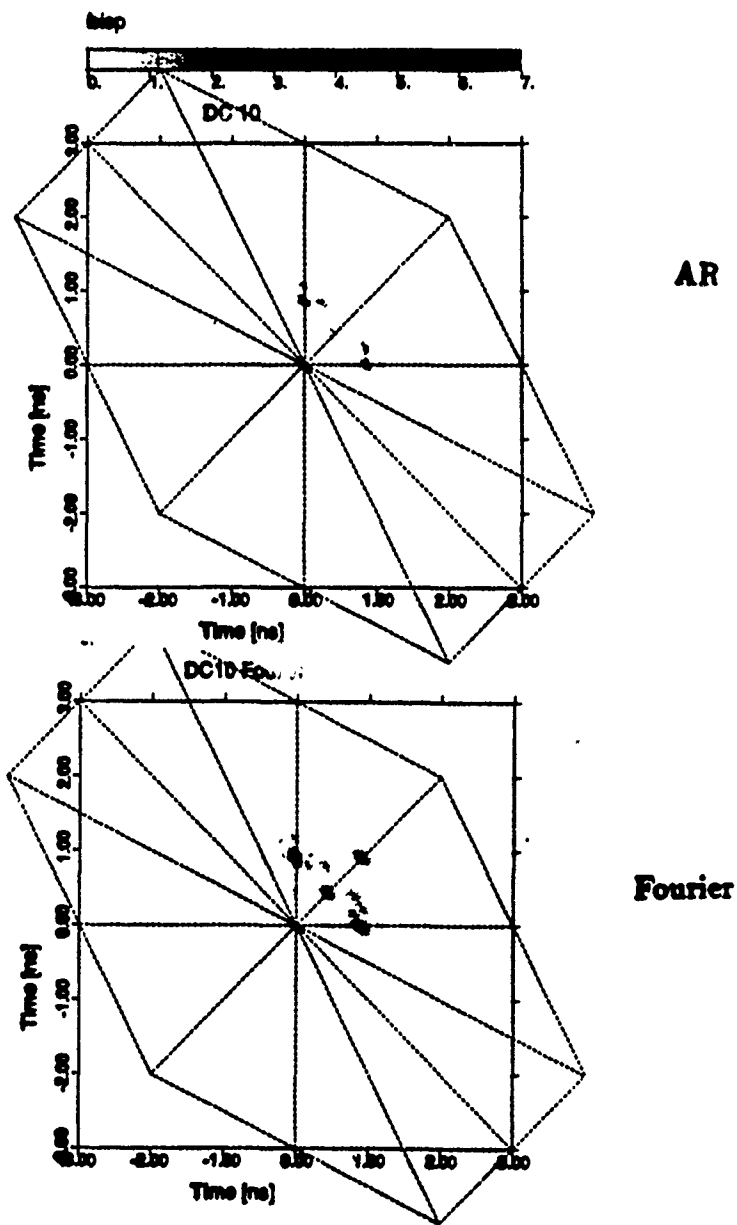
Figure 4.10: Birange profile for the DC-10 obtained using Fourier transform
and AR modeling (based on second order cumulants).

Table 4.1: Comparison between AR and Fourier birange features of the synthesized target example.

Three-point target $\delta r = .015$ m			
Peaks	AR	Fourier	True
r_1	.1752	.1715	.1789
r_2	.3161	.3185	.3111

Chapter 5

CLASSIFICATION OF RADAR SIGNATURES

5.1 Introduction

The focus in this chapter is on using the birange profile as a basis for discriminating between target signatures and for classifying unknown airborne radar targets. A radar target identification system is designed to distinguish birange profiles of unknown objects as belonging to one of a set of M classes, with each class corresponding to a particular target. The goal is to devise and test efficient algorithms that can be employed for classification purposes.

Bispectral processing of radar signals has an inherent advantage over spectral processing; namely the suppression of additive Gaussian noise or any additive unwanted random signal with symmetric probability density function. This advantage motivates our interest in using the birange profile for target recognition purposes, particularly if the backscatter waveforms are corrupted with disturbances that can be modeled as zero mean additive Gaussian noise [22]. Therefore it is of interest to assess the reliability of target identification when using the birange profile as a feature source.

Although total suppression of Gaussian noise is possible when the scattering measurements are recorded over an infinite frequency range, in prac-

136

tice the radar measurement frequency range is limited. Therefore, some noise components remain in the birange profile. Consequently, the percentage of correct classification of radar targets, using the birange as a feature source, is expected to decrease as the additive noise power is increased or the signal-to-noise ratio (SNR) is decreased. To analytically study the effect of the noise on classification performance, we need to know the underlying distribution of the birange as a function of noise power σ^2. This distribution is derived in Section 5.2.

The process of target classification is approached in two ways; parametric and nonparametric. The parametric approach requires the knowledge of the underlying distribution of the birange profile and the *a priori* probability of occurence of each target. Such an approach is useful for estimating the optimal classification performance that could be achieved using the birange as a feature. Due to the lack of knowledge of the *a priori* probabilities of possible targets, and due to the computational burden imposed by parametric classification, it is often more appropriate to use simpler nonparametric classifiers.

Using the birange or other time domain profile in target classification may be rewarding when nonparametric recognition methods are required. If the underlying distribution of the scattered waveform is not known or if the target probability of occurence is not known *a priori*, then one might consider classification using processed radar signatures such as the birange profile or the transient response. Target classification under these conditions may lack optimality. Therefore, if parametric classification is not possible due to certain conditions imposed on the data then both frequency-domain and time-domain features should be considered. Hence, the birange profile can be considered as a feature source for nonparametric classifiers. The focus in this chapter is on devising and testing the performance of

some non-parametric classifiers. Such classifiers include cross-correlation and nearest neighbor methods.

5.2   The Underlying Distribution of a Single Response in the Birange

The underlying distribution of the birange profile of noisy radar signals is an indication of the effect of additive Gaussian noise on the estimate of the birange. The derivation of the likelihood function of birange estimates is the first step in parametric classification studies. The likelihood function of the estimate of the birange profile at a point (r_k, r_l) given that this birange profile corresponds to a target of class i is denoted as

$$p(B(k,l)/i) \quad \forall k, l \in \{1, \ldots, N\} \tag{5.1}$$

where N^2 is the number of pixels in the birange profile, where about $.75N^2$ pixels are used to display the birange (the birange hexagon is displayed inside the square defined by N^2 pixels). Therefore, the likelihood function of the birange profile is simply the joint likelihood function for all pixels.

Assume that the estimate of the birange is obtained using the direct approach without segmenting the data. Then,

$$B_i(r_k, r_l) = K h'_{ik} h'_{il} h'_{i(k+l)} \tag{5.2}$$

where $h'_{ik} = h_{ik} + n_{ik}$ is the real-valued noisy impulse response of target i evaluated using a discrete Fourier transform of the band-limited target frequency response and K is a constant. If the impulse response h'_{ik} is computed without zero-padding the measured frequency response, then it can be shown [75] that the transient response at range r_k has a Gaussian distribution with mean h_{ik} and variance σ^2. Note that $\{h_{ik}\}_{k=1}^N$ are independent identically distributed (i.i.d.) random variables. Therefore, the likelihood

138

function of the pixel (r_k, r_l) of the birange profile is just the likelihood function of the product of three independent identically distributed (iid) samples of the transient response (as given in (5.2)). This can be done in two ways; using a transformation of random variables, or using the Mellin transform. Unfortunately, in either case it is difficult to derive a closed form expression of the underlying distribution. These two approaches are investigated below.

A-Transformation of random variables:

It is possible, using the following transformation of the random variables $\{h_{ik}\}$ (where h_{ik} is the impulse response of target i at range r_k) to a new set of random variables $\{z_k\}$, to derive the likelihood function of the product in (5.2) as the marginal distribution of the new random variable $z_3 = h_{ik}h_{il}h_{i(k+l)}$.

$$h_{ik} = z_1 \qquad (5.3)$$

$$h_{il} = z_2$$

$$h_{i(k+l)}h_{il}h_{ik} = z_3$$

The Jacobian for the transformation from h_{ik} to z_k is $|J| = \frac{1}{z_1 z_2}$. Then, the likelihood function of the birange at (r_k, r_l) is simply the marginal distribution of z_3 given as:

$$p(B(k,l)/i) = \int_{-\infty}^{\infty} \int_{-\infty}^{\infty} \frac{1}{(2\pi)^{3/2}\sigma^3} \frac{1}{z_2 z_1} \qquad (5.4)$$

$$\exp\left[\frac{-(z_1 - h_{ik})^2 - (z_2 - h_{il})^2 - \left(\frac{B(k,l)}{z_2 z_1} - h_{i(k+l)}^2\right)}{2\sigma^2} \right] dz_1 dz_2$$

where $h_{ik}, h_{il}, h_{i(k+l)}$ are samples from the noise free transient response at ranges

$r_k, r_l, r_k + r_l$ for a target of class i. It is possible to solve numerically for $p(B(k,l)/i)$.

B-Using the Mellin transform

The distribution for the product of n independent nonstandardized random variables can be found as an infinite summation using the Mellin transform and the complex residue theorem [19]. For $n = 3$, the likelihood function of a single pixel in the birange is

$$p(B(k,l)/i) = A_1 \sum_{p=0}^{\infty} \sum_{q=0}^{2} c_{pq} \left[\frac{B^2}{8\sigma^6}\right]^p \left[-\ln\frac{B^2}{8\sigma^6}\right]^{2-q} \frac{B}{4\sigma^3} \qquad (5.5)$$

$$\pm A_2 \sum_{k=1/2}^{\infty} \sum_{q=0}^{2} d_{kq} \left[\frac{B^2}{8\sigma^6}\right]^k \left[-\ln\frac{B^2}{8\sigma^6}\right]^{2-q} \frac{B}{4\sigma^3}$$

where $\pm$ corresponds to $\mp B > 0$, and where

$$A_1 = \frac{\exp\left[\frac{1}{2}\sum_j \left(\frac{h_{ij}}{\sigma}\right)^2\right]}{(2\pi)^{3/2}\sigma^3} \qquad (5.6)$$

$$A_2 = 2^{3/2}\frac{A_1}{\sigma^3} \prod_{j=1}^{3} h_{ij}. \qquad (5.7)$$

The coefficients c_{jq}, d_{kq} can be obtained using

$$c_{pq} = \sum_{m=0}^{q} \binom{q}{m} U_1^{(m)}(s,p) \left(\prod_{j=1}^{3} \Phi_1(j)\right)^{(q-m)} \qquad (5.8)$$

$$d_{kq} = \sum_{m=0}^{q} \binom{q}{m} U_{3/2}^{(m)}(s+p+\frac{1}{2}) \left(\prod_{j=1}^{3} \Phi_2(j)\right)^{(q-m)} \qquad (5.9)$$

$$U_b^{(q)} = \frac{d^q}{ds^q} \left(\frac{\Gamma(s+b+p)}{(s+b-1)(s+b)\ldots(s+b-2+p)}\right)^3 \qquad (5.10)$$

$$s = -p, \quad p = 0,1,2,\ldots \qquad (5.11)$$

$$s = -k, \quad k = \frac{1}{2},\frac{3}{2},\frac{5}{2},\ldots$$

where

$$\Phi_1(j) = \Phi\left(s;\frac{1}{2};\frac{h_{ij}^2}{2\sigma^2}\right) \qquad (5.12)$$

$$\bar{\Phi}_2(j) = \bar{\Phi}\left(\frac{2s+1}{2};\frac{3}{2};\frac{h_{ij}^2}{2\sigma^2}\right) \qquad (5.13)$$

$$\Phi(a;c;z) = 1 + \frac{a}{c}\frac{z}{1!} + \frac{a(a+1)}{c(c+1)}\frac{z^2}{2!} + \ldots \qquad (5.14)$$

where h_{ij} is the noise free transient response at range r_j, $1 \leq j \leq N$ for target i. Also, the $(q-m)^{th}$ derivative of the function Φ can be evaluated using Leibnitz's rule as

$$\left[\prod_{i=1}^{n} \Phi_a(i)\right]^{(q-m)} \tag{5.15}$$

$$= \sum_{j_1=0}^{q-m} \sum_{j_2=0}^{j_1} \cdots \sum_{j_n=0}^{j_{n-1}} \binom{q-m}{j_1} \cdots \binom{j_{n-1}}{j_n} \Phi_a^{(r-j_1)}(i) \cdots \Phi_a^{(j_{n-1}-j_n)}(n)$$

where j_c, $c = 1, 2, \ldots, n$ must satisfy $j_1 + j_2 + \ldots + j_n = q - m$.

The derivative of the function $U_b^{(m)}$ can be obtained using the following

$$U_b^{(q+1)}(s) = \sum_{l=0}^{q} \binom{q}{l} U_b^{(q-l)}(s) V_b^{(l)}(s) \tag{5.16}$$

where

$$V_b^{(l)}(s) = 3\Psi^{(l)}(s+b+p) + \sum_{i=0}^{p-1} (-1)^{l+1} \tag{5.17}$$
$$\times (l+1)!(s+b-1+i)^{-l-1}$$

and where $\Psi^{(1)}(s+b+p)$ is the digamma function, and $\Psi^{(l)}(s+b+p)$ is the polygamma function given as for $l > 1$

$$\Psi^{(l)}(s+b+p) = (-1)^{l+1} l! \sum_{\alpha=0}^{\infty} (l+1+\alpha)^{-(s+b+p)} \tag{5.18}$$

The above is the likelihood function for the birange profile at a point $(k, l), 1 \leq k, l, \leq N$. In order to obtain the likelihood function for all points k, l we need to compute the joint distribution for all pixels in the birange domain. The birange pixels, however, are correlated (along vertical and horizontal lines) i.e.,

$$E\{B_i(k, l) B_i(k, n)\} = E\{h_{ik}^2 h_{il} h_{in} h_{i(k+l)} h_{i(k+n)}\} \tag{5.19}$$

$$\neq E\{B_i(k, l)\} E\{B_i(k, n)\} \tag{5.20}$$

where $B_i(k, l)$ denotes the birange of target i at (r_k, r_l). Also notice that the variance of a single response in the birange is

$$\mathrm{var}(B_i(k, l)) = \sigma^6 + \sigma^4 \left[h_{ik}^2 + h_{il}^2 + h_{i(k+l)}^2\right] \tag{5.21}$$

141

$$+ \quad \sigma^2 \left[h_{ik}^2 h_{i2}^2 + h_{il}^2 h_{i(k+l)}^2 + h_{ik}^2 h_{i(k+l)}^2 \right]$$

This indicates that the variance is proportional to the third power of the noise variance and is also dependent on the data.

Figure 5.1 shows an example of the likelihood function (or conditional probability density function) of one pixel in the birange profile of noisy radar signals. In this figure, the values h_{ij} for the noise free impulse response of target i at ranges r_j, $j = 1, 2, 3$ are given as $h_{i1} = 1$, $h_{i2} = 1$, $h_{i3} = .4$.

Notice, that the distribution is not symmetric, and its skewness depends on the noise free values of the transient response at r_1, r_2, and $r_1 + r_2$. The distribution in Figure 5.1 corresponds to $\sigma = 1$; therefore, $\sigma^4 = \sigma^6 = 1$. If $\sigma > 1$ then the variance of the above distribution will increase rapidly with σ.

Using the above likelihood function, it is possible to redefine the birange as a deterministic component, determined by the expected value of B, added to a random variable with a probability density function as given in (5.4). This definition of the birange may be helpful in experimental target recognition studies where it is possible to obtain an estimate of the noisy birange by adding a randomly generated number whose probability density function is as shown in Figure 5.1 to the triple product of transient response samples. It is also possible, by assuming that the birange pixels are uncorrelated, to obtain an approximate evaluation of a parametric target classification algorithm based on the birange. Furthermore, a more accurate expression of the probability of detection using the bispectrum can be obtained by using the above distribution instead of the normal (asymptotic approximation) distribution used in [56,57].

Likelihood function for one bispectral sample
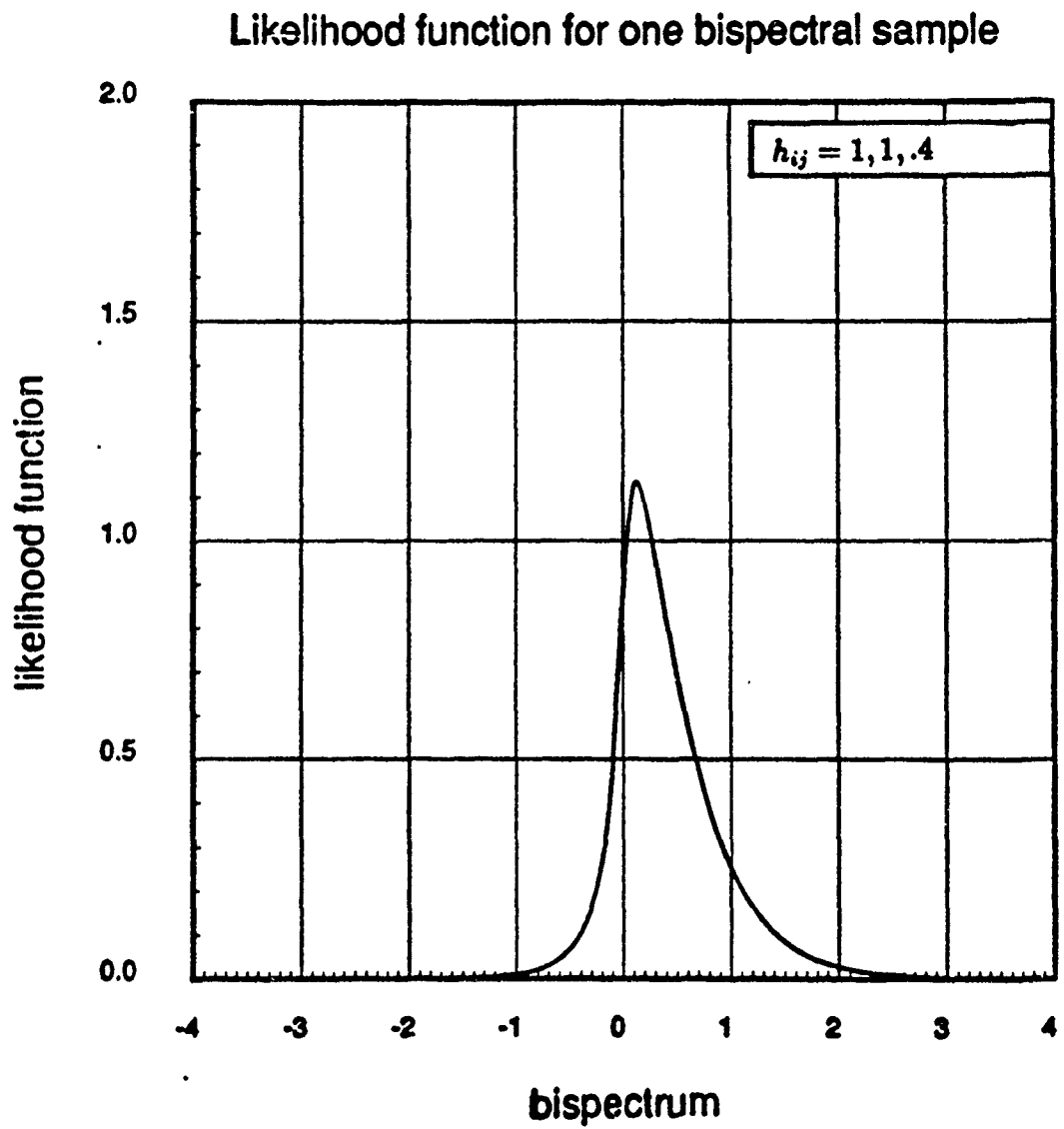
Figure 5.1: Likelihood function of a single response in the birange

5.3 Classification Techniques

The classification of radar signals using the birange profile as a feature source is developed in this section. The focus is on nonparametric classification methods. Although it is possible to design a parametric classifier such as Bayesian classifier using the likelihood function derived in the previous section, it is very computationally inefficient to do so. Further, there seems to be no significant reasons for classifying targets parametrically using processed radar data since optimal parametric classification performance can be achieved using the measured data directly.

Three non-parametric birange-based classification methods are discussed in this section. These classifiers are: the birange nearest neighbor classifier, and the birange cross-correlation classifier. Employing any of these classification methods is dependent on the available information about the target, and in particular on the zero-time reference.

5.3.1 The Birange Nearest-Neighbor Classifier

The distribution of birange N^2-tuples in the feature space indicates that the classes are distributed on convolved non-planer surfaces which cannot be separated by hyperplanes except possibly in very localized regions. Therefore, linear discriminants cannot be used to separate classes of radar targets in terms of birange profiles. The nearest neighbor (NN) decision rule is a less constrained classification method that can be easily employed to discriminate between targets based on the birange profile. The NN rule has performed satisfactorily when used for classification of frequency-domain target signatures [26,37].

The nearest neighbor decision rule can be used to classify unknown radar targets if the zero-time reference of the target with respect to the radar is known *a priori*. Thus, the NN rule is used when absolute phase

144

information is available (zero-time reference is known). The NN rule in this case is given as,

Assign the unknown target u to class (i) if

$$d_i = \min_j \{d_j\}, \quad j = 1, \ldots, M \quad \text{where}$$

$$d_j = \sqrt{\sum_{t_1} \sum_{t_2} (B_u(t_1, t_2) - B_j(t_1, t_2))^2} \qquad (5.22)$$

where $B_x(t_1, t_2)$ is the birange profile of target x. Notice that this decision rule is based on selecting the class whose Euclidean distance to the unknown target prototype is the smallest. Therefore, it is necessary for the birange profile of both, the unknown target and the catalog target to be displayed exactly in the same position in the (t_1, t_2) plane.

The lack of information about the target zero-time reference suggests the use of a classification algorithm that takes into consideration all possible positions of the target in the time domain. An alternative to using NN rule as discussed above is to include birange profiles of all possible positions of the target in the catalog of each class. The decision rule, then, is based on the nearest neighbor among all targets and among all possible positions of each target. Thus, this algorithm assigns the unknown target to class i if

$$d_i = \min_j \{\min_\tau \{d_{j\tau}\}\} \quad j = 1, \ldots, M, \quad 0 \le \tau \le \frac{1}{\Delta f} \qquad (5.23)$$

where Δf is the frequency increment of the measured scattering data. The birange of each target catalog must be known at all possible choices of τ. This classification algorithm is computationally inefficient because it requires the computation of the birange profile of the catalog (or the unknown) for each possible τ.

When the target zero-time reference is unknown, an alternative approach to NN classification is to apply a linear shift τ to the transient response. This can be done either by shifting the transient response of the

145

unknown target, or by applying a ramp shift (as a function of frequency) with slope τ to the phase of the measured frequency response $H(f)$ as

$$H'(f) = H(f)\exp\{2\pi f\tau\} \quad \forall \tau \leq \frac{1}{\Delta f} \qquad (5.24)$$

Which corresponds to shifting the birange profile along the $t_1 = t_2$ axis. In fact, applying a linear phase shift to the data corresponds to uni-directional correlation between the two-dimensional birange profile and the catalog. This form of cross-correlation considers all possible positions the zero-time reference along the radar-target axis. Computationally, however, it is inefficient to compute the birange profile of the unknown target and the catalog targets and then correlate in the time domain.

5.3.2   Cross-correlation Classifier

The classification of birange profiles using cross-correlation is developed in this section. This classifier assumes that the target zero-phase reference is known *a priori*. The focus in this section is on the definition of the cross-correlation classifier. The goal of this algorithm is to find a catalog element (i) that matches the bispectral response of an unknown target $B_u(r_1, r_2)$. That is one wishes to minimize

$$\min_{i}\left\{\int_{r_1}\int_{r_2}\left(B_i(r_1, r_2) - B_u(r_1, r_2)\right)^2 dr_1 dr_2\right\} = \qquad (5.25)$$

$$\min_{i}\left\{\int\int B_i^2(r_1, r_2)dr_1 dr_2 + \int\int B_u^2(r_1, r_2)dr_1 dr_2\right. \qquad (5.26)$$

$$\left. - \int\int B_i(r_1, r_2)B_u(r_1, r_2)dr_1 dr_2\right\}$$

If the first two terms in (5.29) are fixed, this entails maximizing

$$\int_{r_1}\int_{r_2}B_i(r_1, r_2)B_u(r_1, r_2)dr_1 dr_2 \qquad (5.27)$$

and since the target zero-phase reference is assumed to be known, then this is equivalent to maximizing

$$\Gamma_{iu}(0, 0) = \qquad (5.28)$$

146

$$\frac{\int_{r_1}\int_{r_2} B_i(r_1,r_2)B_u(r_1,r_2)\ dr_1\ dr_2}{\left[\int_{r_1}\int_{r_2}|B_u(r_1,r_2)|^2 dr_1 dr_2\right]^{\frac{1}{2}}\left[\int_{r_1}\int_{r_2}|B_i(r_1,r_2)|^2 dr_1 dr_2\right]^{\frac{1}{2}}}$$

where $\Gamma_{iu}(0,0)$ is the normalized cross correlation of the catalog target birange profiles for $i=1,2,\ldots,M$ and the test target response u. Using Fourier transform identities and Parseval's theorem, we find that the cross-correlation can be written for the discrete frequency case as

$$\Gamma_{iu}(0,0)=\frac{I2FFT\{R_i(f_1,f_2)R_u^*(f_1,f_2)\}}{\left[\sum_{f_1}\sum_{f_2}|R_i(f_1,f_2)|^2\right]^{\frac{1}{2}}\left[\sum_{f_1}\sum_{f_2}|R_u(f_1,f_2)|^2\right]^{\frac{1}{2}}} \qquad (5.29)$$

The test target is classified as target c if

$$\Gamma_{cu}(0,0)=\max_i\{\Gamma_{iu}(0,0)\}\quad i=1,\ldots,M. \qquad (5.30)$$

5.4 Experimental Study

A comparison between the performance of the cross-correlation classifier using the birange and the performance of other optimal and suboptimal classifiers is given below. The comparison includes classification in additive white Gaussian noise, additive colored Gaussian noise, and additive non-Gaussian noise. Classification with azimuth ambiguity is also investigated. Also, the effect of extraneous uncatalogued scatterers on the classification performance is examined.

The probabilities of target misclassification at different signal-to-noise ratios are estimated using Monte-Carlo simulations. When the *a priori* probability of a target hypothesis is not known, then N test samples are drawn randomly and then used to determine whether the classifier gives the correct decisions for these samples or not. If the a priori probabilities P_i, $i=1,\ldots,M$ (M is the number of hypotheses) are known then $n_i = P_iN$ samples are drawn from class (i), to which noise is added and then these samples are tested by the classifier.

147

The classifiers simulated in this study are the following:

1- Nearest Neighbor rule based on the backscatter data without employing any signal processing. Given that the measured backscatter is $H_u = [H_u(\omega_1), \ldots, H_u(\omega_K)]$ (where K is the number of frequencies used) then the NN rule classify the unknown as target i if

$$(H_u - H_i)^T(H_u - H_i) = \min_j\{(H_u - H_j)^T(H_u - H_j)\} \quad j = 1, \ldots, M. \quad (5.31)$$

2- Cross-correlation based on its one-dimensional time-domain response. For this algorithm, target $\{i\}$ is chosen such that

$$\Gamma_{iu}^I = \max_j \left[\left| \frac{\sum_k h_u(k)h_j(k)}{\sqrt{\sum_m |h_u(m)|^2 \sum_n |h_j(n)|^2}} \right| \right], j = 1, \ldots, M \quad (5.32)$$

Note that this is equivalent to maximizing the down-range cross-correlation between the unknown target impulse response and the catalog impulse response.

3- Cross-correlation of birange profiles as discussed in Section 5.3.3.

The performance of the cross-correlation classifier using the birange is dependent on the birange estimation procedure (or the estimation of triple correlation). The amount of segmentation used in computing the triple correlation had a significant effect on the performance of the classifier. Oversegmenting the data may result in a degraded classification performance. The triple correlation lag used and the number of data points also influence the performance of the classifier. Finally, removing the average from both the unknown and the catalog improves the classifier performance.

A Monte-Carlo simulation was performed to evaluate the performance of the classifiers mentioned above. The data base used in these examples has been frequently used in radar target identification studies [6,7,8]. The data base consists of experimental measurements in the frequency band from $1 - 12$ GHz of scale models of commercial aircraft. A photo with

148

corresponding names of these aircraft is shown in Figure 3.9. The scaled data corresponds to measurements of the radar cross section (RCS) of full scale aircraft in the HF/VHF frequency band (8-58 MHz). Details of these measurements can be found in [64].

Decision statistics for each target are computed at a fixed noise level, and total statistics of classification error for all targets are obtained. One hundred experiments were performed for each test target (for a total of 500 experiments). The entire test is repeated at different noise levels. Finally the misclassification (error) percentage is plotted versus signal to noise ratio. When classifying with the birange, the best performance was obtained when the data is segmented into $K = 5$ records of $M = 21$ samples each with a correlation lag $L = 10$ (see Section 2.3.4).

Figure 5.2 shows the classification performance for five commercial aircraft with complete azimuth information using additive white Gaussian noise. The catalog consists of scattering data for five commercial aircraft at $0°, 10°$, and $20°$ azimuth. The performance of the nearest neighbor (NN) algorithm is optimal for this case. The birange classifier is outperformed by the impulse response classifier. We also re-iterate that the performance of the birange classifier is very sensitive to the triple correlation estimation procedure. The performance of the birange classifier may degrade if the number of correlation lags is altered or if the window function is changed (the window used in this study is given in (2.60)). This performance figure shows that birange profile estimates can be used effectively in radar target identification. Increasing the number of data samples and employing an optimized classification scheme may improve the performance of the birange classifier and reduce its sensitivity to the triple correlation estimation procedure.

Figures 5.3 and 5.4 show the classification performance when additive

colored noise generated by passing white Gaussian noise through an AR or MA filter respectively. The AR filter coefficients $\{a_i\}_{i=0}^{15}$ are [.5, .6, .7, .8, .7, .6, .5, 0, 0, .5, .6, .7, .8, .7, .6, .5] (see [61] for the autocorrelation of the noise generated using this filter), and the MA filter has coefficients [1, .8]. The target azimuth is assumed to be completely known. The NN rule (which may be suboptimal in this case) applied to the frequency-domain data outperforms the time-domain classifiers. Also, the performance of the birange classifier compares favorably with the performance of the impulse response classifier. The degradation of the time-domain classifiers compared to the nearest neighbor rule is slightly less for the additive white noise case, which may suggest a comparable performance of all classifiers under other colored noise conditions.

Figure 5.5 shows the classification performance when additive non-Gaussian noise is used (the square root of a Weibull distributed random variable added to both the in-phase and quadrature components of the data). The azimuth is assumed to be completely known. The performance of the birange classifier is improved and is comparable to the other classifiers, which may indicate a significant role for the birange in classification of unknown targets in a non-Gaussian noise environment.

Figures 5.6 and 5.7 show the classification performance when the azimuth is known only to within $\pm 10°$ (Figure 5.6) and $\pm 20°$ (Figure 5.7). Although the nearest neighbor rule is not optimal in this case, it outperforms the time-domain classifiers. Further, the performance of the birange classifier degrades compared to the impulse response classifier when the azimuth ambiguity range increases. In fact, if the target is assumed to be known within $\pm 30°$ (not shown in the Figures) then the performance of the birange classifier degrades significantly compared to the impulse response classifier. These figures show that the birange is sensitive to changes in

target azimuth position. This sensitivity may be explained by the fact that changing the azimuth may introduce additional multiple interactions and delete others. Although these interactions also affect the impulse response, they more strongly affect the birange.

Figure 5.8 shows the classification performance when the classifier is mis-informed about the target azimuth position with an error of $\pm 10°$. That is, a target at azimuth $A°$ is compared with the catalog targets at azimuth $A° \pm 10°$. This type of mismatch in design specifications affects the classification performance of all classifiers including the birange classifier. It is clear from Figure 5.8 that time-domain classification techniques outperform the nearest neighbor classifier in this case. Although the birange classifier is sensitive to change 'n target azimuth, Figure 5.8 shows that the birange is less affected by inaccurate azimuth information than the nearest neighbor classifier.

5.4.1 Effect of Extraneous Scatterers

In the following, we discuss the effect of adding extraneous scatterers to the unknown target frequency response (scatterers not included in the catalog) on the performance of the classifiers under investigation. This type of classification problem may occur when clutter (in the form of point scatterers with or without interactions) is detected, or when the catalog target model is inaccurate or incomplete.

The effect of this type of disturbance is simulated as a set of additive point scatterers with variable scattering magnitude located at different positions with respect to the target. The ratio of scattering from the target plus extraneous scatterers to scattering from the extraneous scatterers only is denoted by SER (Signal-to-Extraneous signal Ratio).

Tables 5.1-5.10 show classification results obtained for different scenar-

151

Figure 5.2: Classification performance of five commercial aircraft with known azimuth and additive white Gaussian noise

152
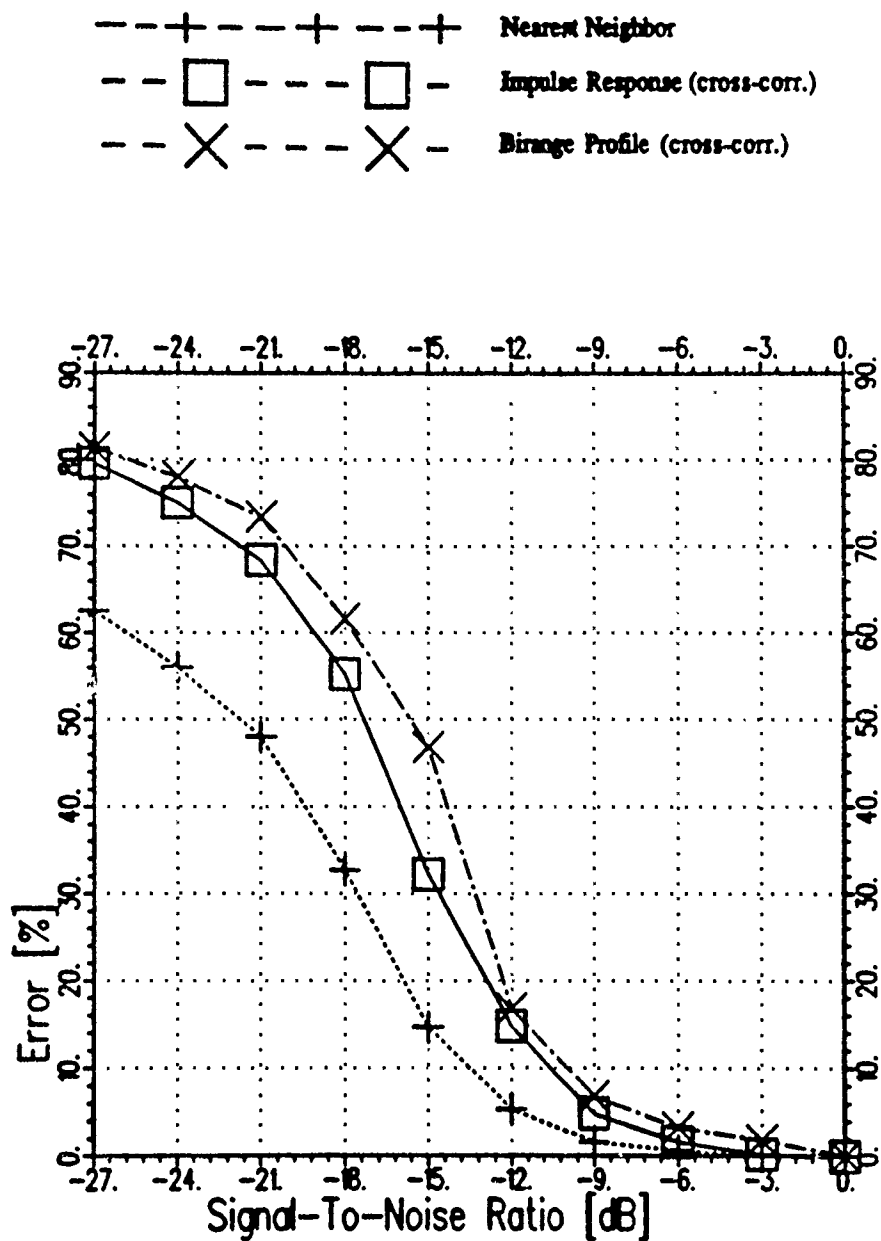
Figure 5.3: Classification performance of five commercial aircraft with known azimuth and additive colored Gaussian noise generated by an AR filter

153
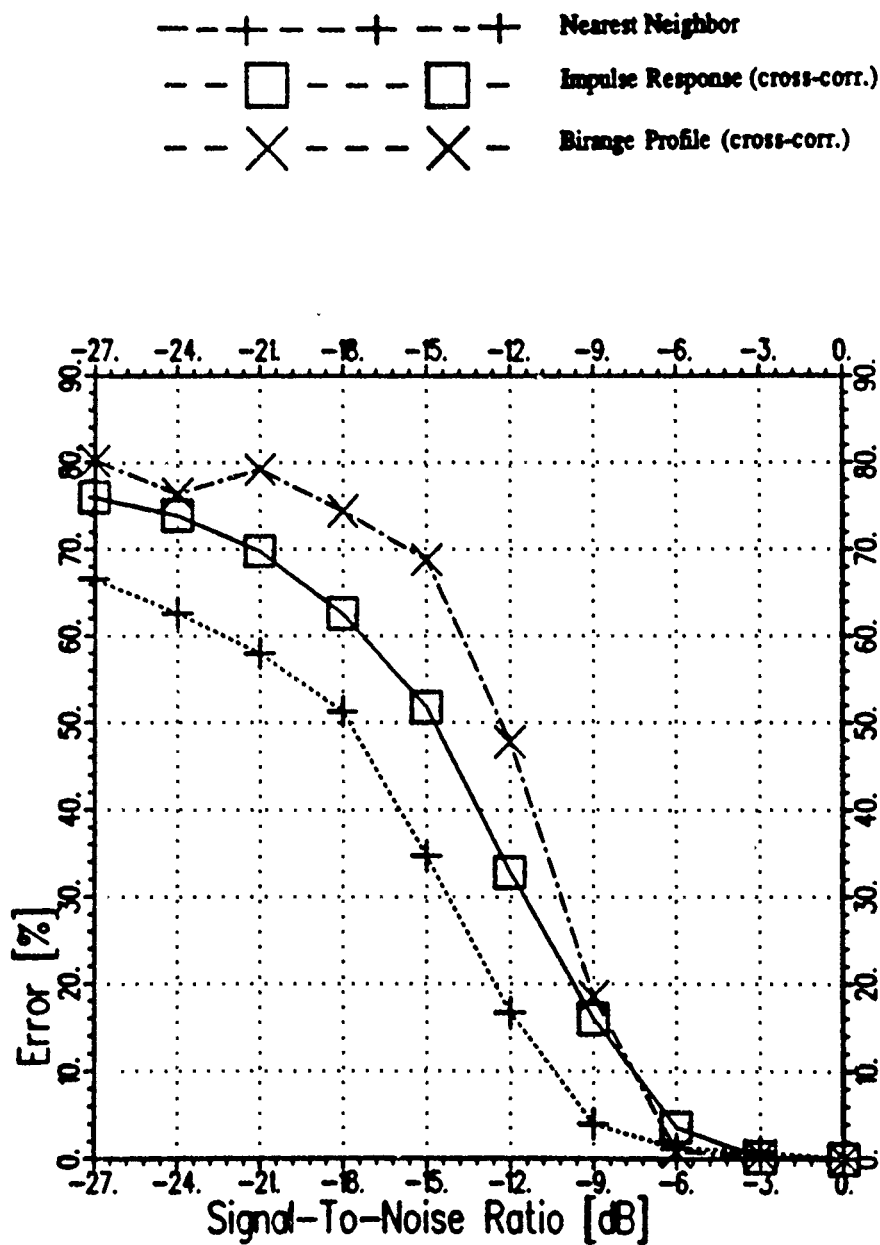
Figure 5.4: Classification performance of five commercial aircraft with known azimuth and additive colored Gaussian noise generated by an MA filter

154
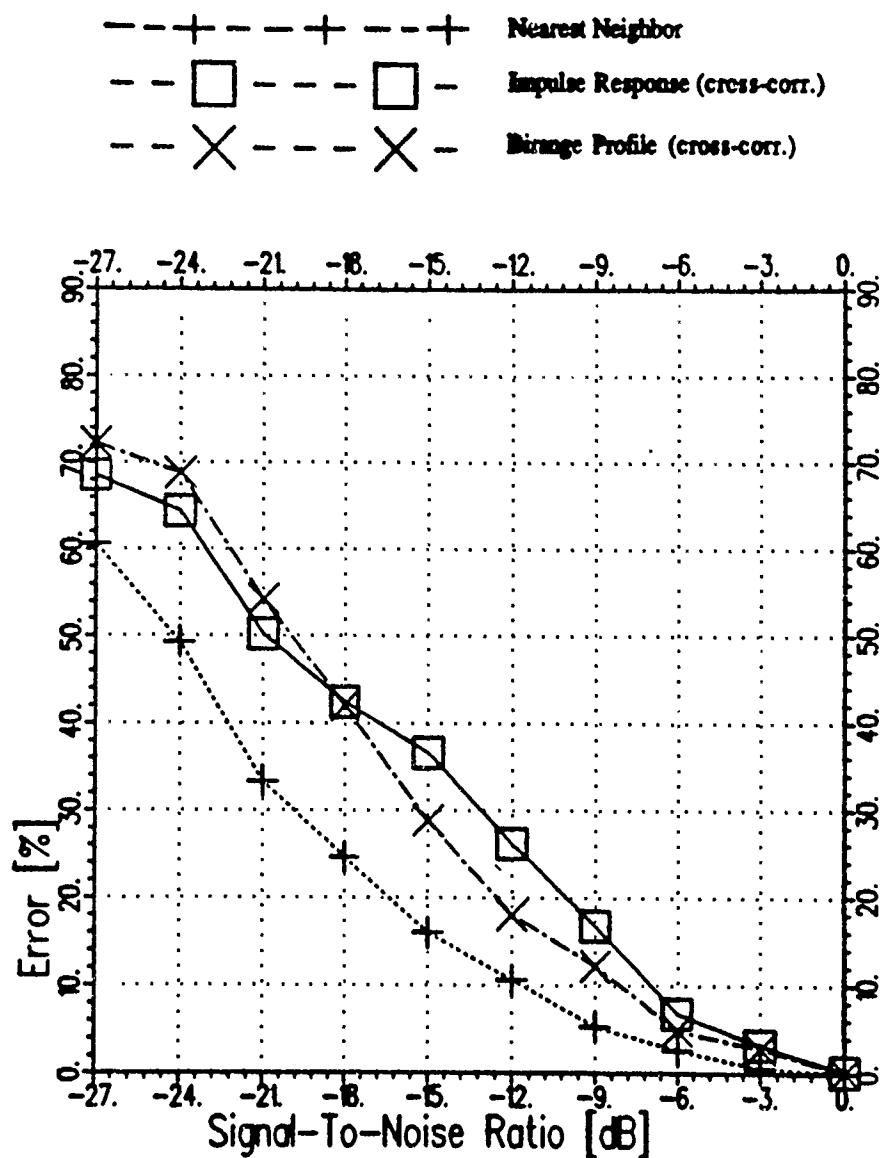
Figure 5.5: Classification performance of five commercial aircraft with known azimuth and additive non-Gaussian noise

155

Figure 5.6: Classification performance of five commercial aircraft with known azimuth within ±10° and additive white Gaussian noise
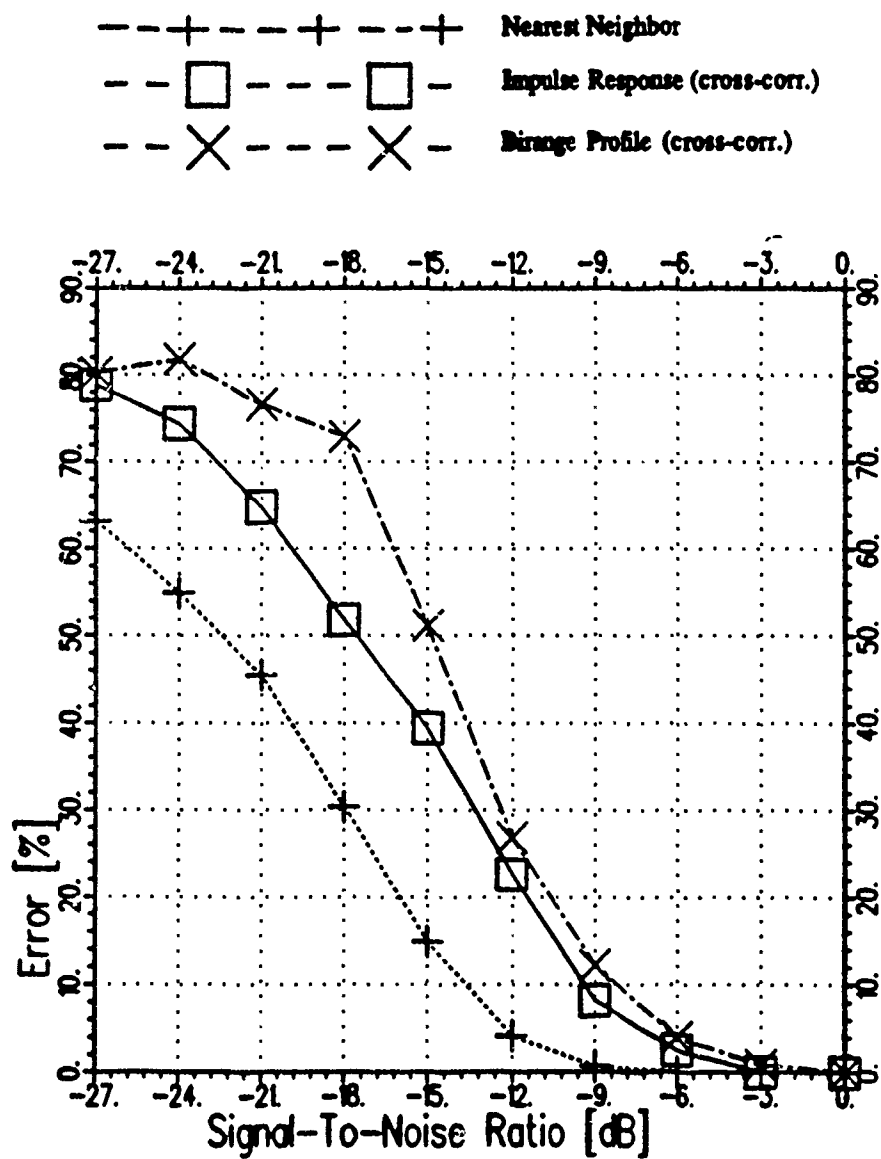
156
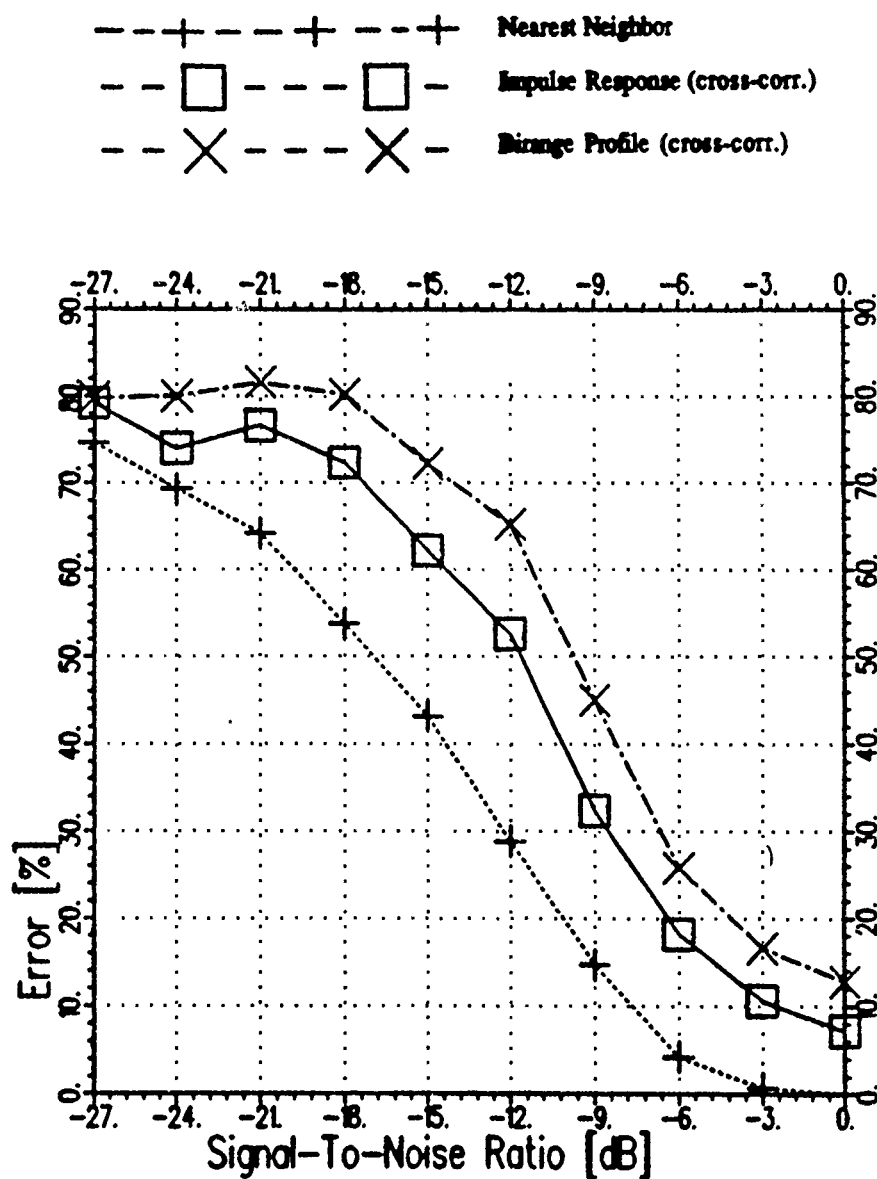
Figure 5.7: Classification performance of five commercial aircraft with known azimuth within ±20° and additive white Gaussian noise
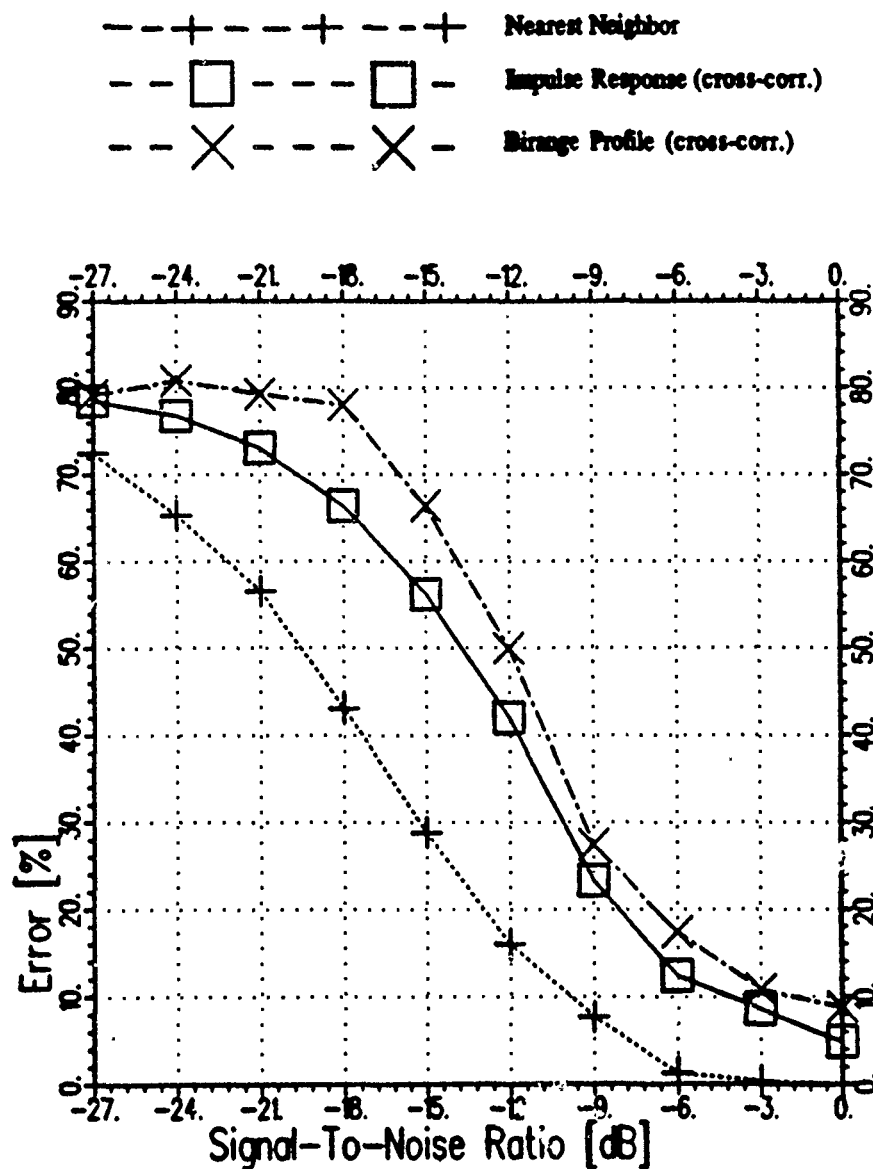
157
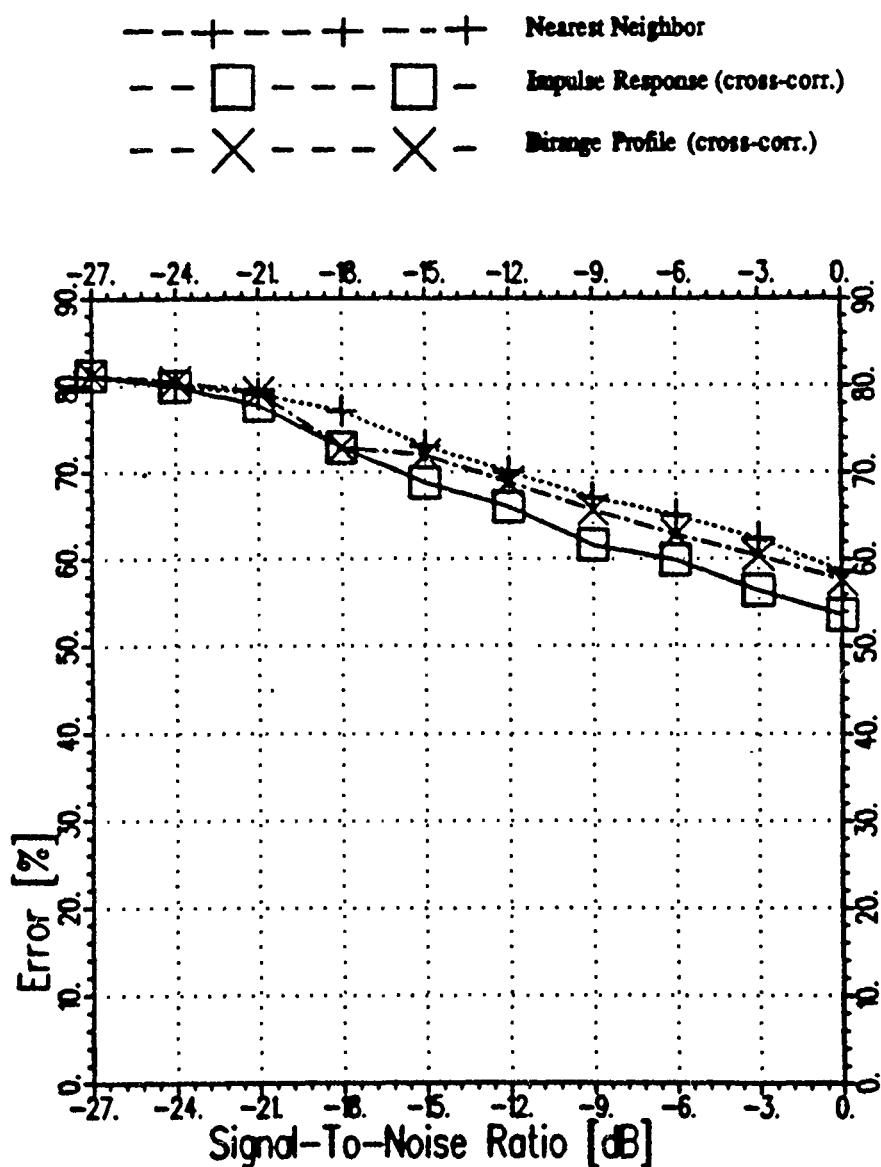
Figure 5.8: Classification performance of five commercial aircraft when inaccurate azimuth information (within ±10°) is given to the classifier with additive white Gaussian noise

ios of extraneous scatterers added at different positions with respect to the target. The error rates shown in these tables represent the percentage of misclassification when scattering from extraneous point scatterers (these scatterers are described in the captions) is added to the frequency response of all five targets. Also, scattering from unknown targets is assumed noise-free since the purpose of these experiments is to evaluate the performance of the birange classifier when backscattered signals include uncatalogued responses. The extraneous scatterers used to generate the results in Tables 5.7 and 5.9 include an interaction whose response appears at −.8 ns, and those used to generate the results in Tables 5.8 and 5.10 include an interaction whose response appears at 0 ns. The bicoherences for both interactions are assumed fixed with a value of 40%.

The following conclusions can be drawn from those experimental results: First, classification with nearest neighbor rule is the most sensitive to the presence of extraneous uncatalogued scatterers. Second, classification with impulse response is less sensitive to extraneous scatterers than the NN classifier but unaffected by changing the position of extraneous scatterers. Finally, we see that the birange is less sensitive to the presence of extraneous scatterers than the nearest neighbor classifiers. The birange classifier is even less sensitive to uncatalogued scatterers if the responses from such extraneous scatterers do not coincide with the response of the unknown target. This insensitivity may be due to the fact that while the presence of extraneous scatterers produces additional peaks in the impulse response, it takes three extraneous scatterers with interaction to produce a peak in the birange profile of the unknown target.

Figures 5.9-5.10 show a comparison between classification results (plotted as probability of misclassification versus the SER). It is clear from these figures that classification using the birange profiles outperforms classifica-

159

tion using the radar cross section measurements (using nearest neighbor) even when the azimuth of the unknown target is partially known (or known within a certain azimuth range). The extraneous signatures used in these figures are three point scatterers where the location of the response due to each scatterer is random and uniformly distributed over $[-\frac{T}{2}, \frac{T}{2}]$, where $T = \frac{1}{\Delta f}$, (where Δf is the frequency increment of the measured data). The locations of the responses of the extraneous scatterers are independent identically distributed. Two hundred experiments including five targets (a total of 1000 experiments) are simulated for each SER ratio.

Figure 5.11 shows classification results obtained when the frequency responses of nine extraneous scatterers is added to the frequency responses of the five aircraft. The location of the response due to each scatterer is random and uniformly distributed over $[-\frac{T}{2}, \frac{T}{2}]$. Figures 5.9 and 5.11 show that classification using the impulse response outperforms classification using the birange when the number of extraneous scatterers is increased to nine. This result can be explained since by adding the responses of nine extraneous scatterers to the data, the likelihood of having a birange peak due to extraneous scatterers is higher than that when only three extraneous scatterers are present. Further, each of the five targets has less than nine scattering centers, which indicates that if the number of the extraneous scatterers exceeds the number of scattering centers then the impulse response classifier outperforms the birange classifier by a significant margin. Figures 5.9 and 5.11 also show that the performance of the nearest neighbor classifier is inadequate whether the number of extraneous scatterers exceeds the number of scattering centers or not.

5.5 Summary

This chapter is concerned with studying the classification aspect of the birange profile when used as a target recognition tool. The purpose of this study is to investigate the feasibility of employing the birange as a feature source in target recognition systems and to examine the conditions under which the birange classifier performs satisfactorily. The classification schemes suggested in this chapter are suboptimal in the sense of minimizing classification error. However, using these classification schemes, it is possible to identify a framework of application for the birange classifier in terms of noise conditions and availability of *a priori* information about aspect angle. The comparisons made in this study include the performance of the nearest neighbor classifier, the impulse response cross-correlation classifier, the birange cross-correlation classifier. The conditions investigated include additive white Gaussian noise, additive colored Gaussian noise, additive non-Gaussian noise, additive uncatalogued scatterers, and error in aspect information.

The classification results in this chapter can be summarized as follows: The nearest neighbor classifier outperforms both the impulse response and the birange classifiers except for the case where the unknown target is misrepresented in the catalog. An unknown target is misrepresented in the catalog if the response due to extraneous scatterers is added to its frequency response or if its aspect angle is not included in the catalog. The impulse response classifier outperforms the birange classifier except for the case of non-Gaussian additive noise. When scattering from extraneous uncatalogued scatterers is added to the frequency response of the unknown target then classification with the birange outperforms classification with impulse response if the signal-to-extraneous scatterers ratio is low and if the number of extraneous scatterers does not exceed the number of scatter-

ing centers along the target. Finally, by considering the outcomes of this study, we conclude that classification with the impulse response is more reliable than other classifiers (all circumstances combined). However, it may be rewarding to use a joint decision rule that combines both the impulse response and the birange classifiers.

Table 5.1: Classification error rate when a single extraneous point target is placed at -2 ns (within the nose area).

SER [dB]	NN	TIME	BIRANGE
1	0	0	0
-4	20	0	20
-9	40	20	40
-12	40	20	40
-15	60	40	40

Table 5.2: Classification error rate when a single extraneous point target is placed at 0 ns (within the wing area).

SER [dB]	NN	TIME	BIRANGE
1	0	0	0
-4	0	0	0
-9	0	20	20
-12	20	60	20
-15	40	60	40

Table 5.3: Classification error rate when a single extraneous point target is placed at 1.2 ns (within the tail area).

SER [dB]	NN	TIME	BIRANGE
1	0	0	0
-4	0	0	0
-9	40	40	0
-12	40	40	0
-15	60	40	20

Figure 5.9: Comparison between classification using measured data (using nearest neighbor), impulse response, and birange profile as the signal-to-extraneous scatterers ratio (SER) changes with complete azimuth information (three extraneous scatterers used).

164
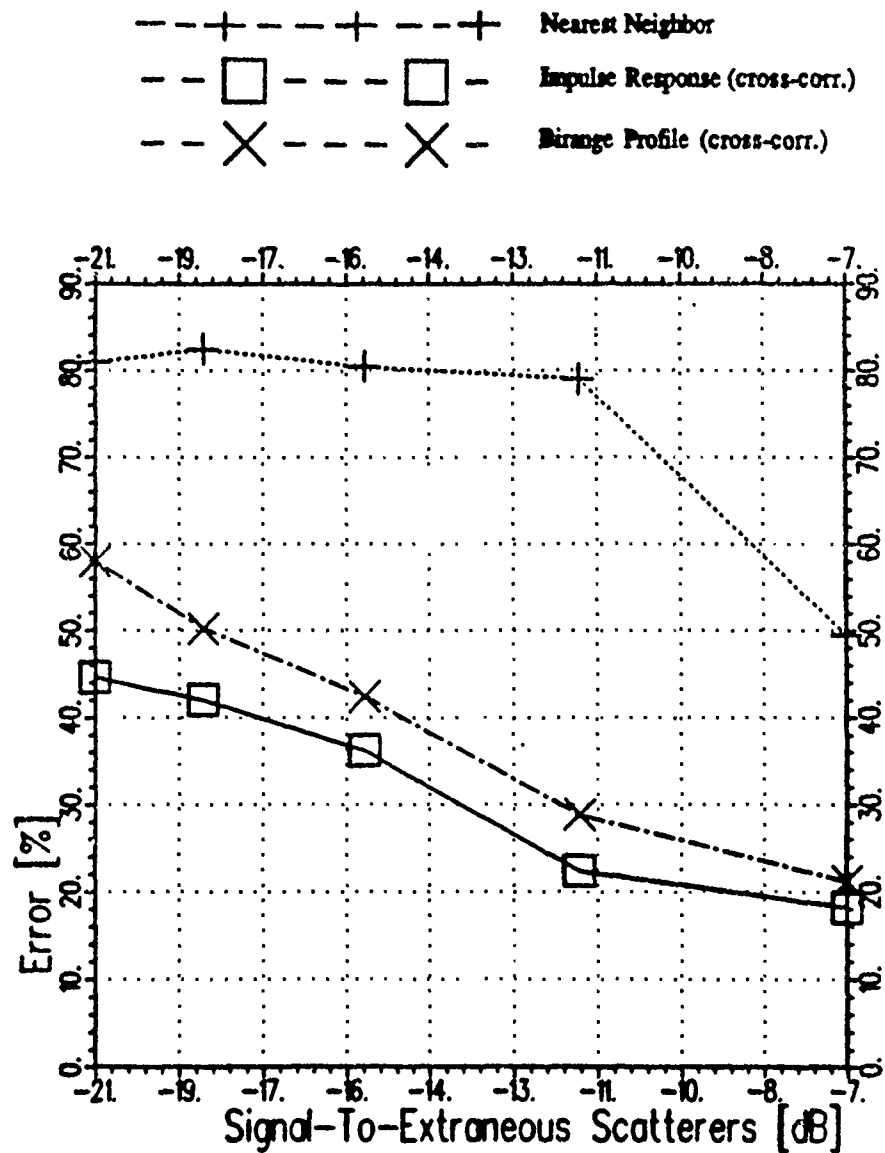
Figure 5.10: Comparison between classification using measured data (using nearest neighbor), impulse response, and birange profile as the signal-to-extraneous scatterers ratio (SER) changes with partial azimuth information ±10° (three extraneous scatterers used).
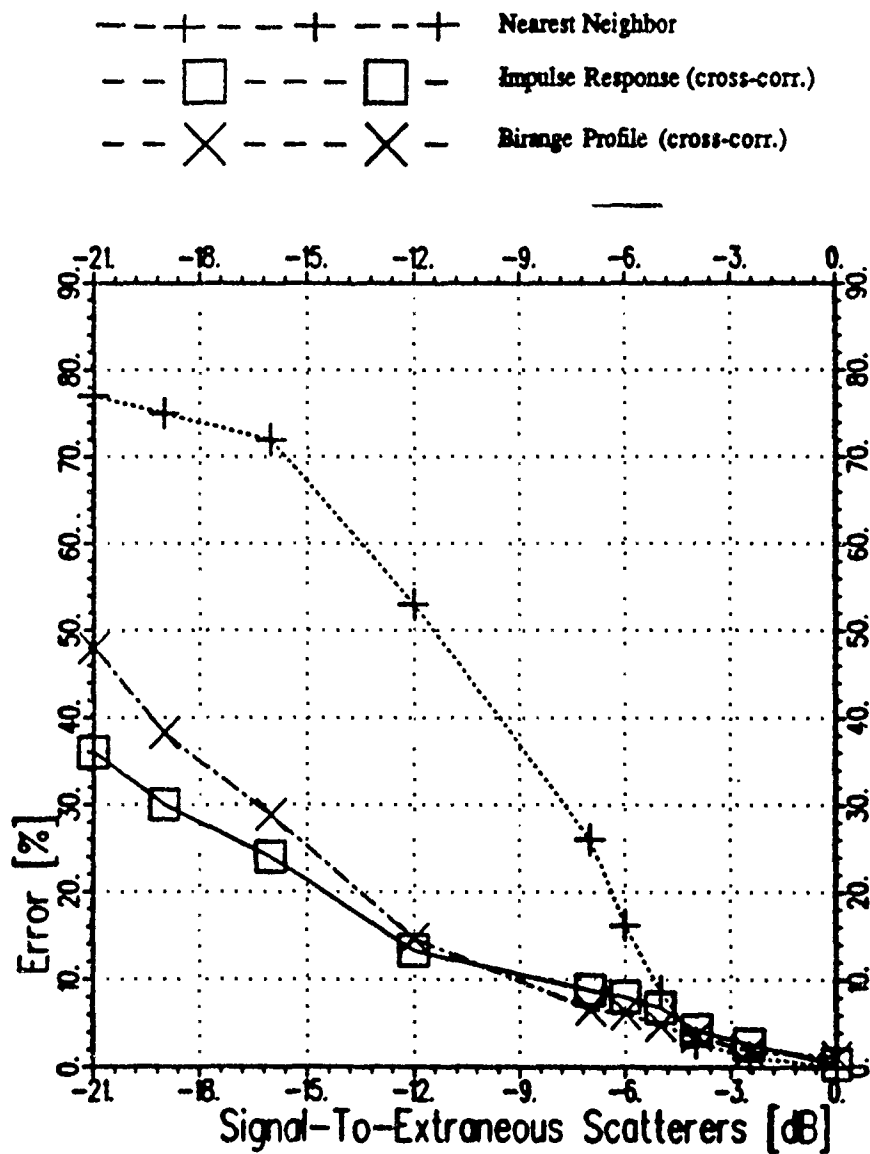
165
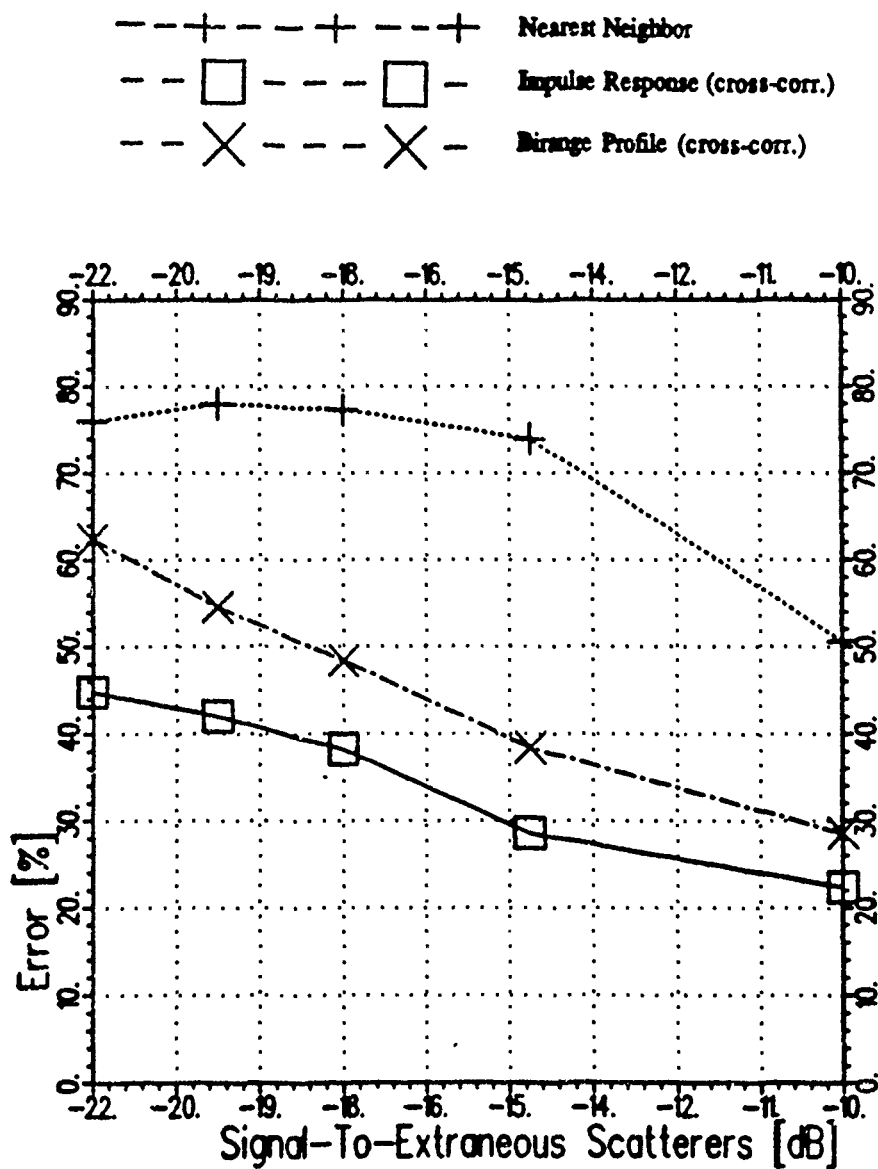
Figure 5.11: Comparison between classification using measured data (using nearest neighbor), impulse response, and birange profile as the signal-to-extraneous scatterers ratio (SER) changes with complete azimuth information (nine extraneous scatterers used).

Table 5.4: Classification error rate when two extraneous point targets are placed at -2 ns and 0 ns respectively.

SER [dB]	NN	TIME	BIRANGE
-2	0	0	0
-8	0	20	20
-12	40	40	40
-14	40	60	40
-16	60	40	60

Table 5.5: Classification error rate when two extraneous point targets are placed at -2 ns and 1.2 ns respectively.

SER [dB]	NN	TIME	BIRANGE
-2	0	0	0
-8	40	20	20
-12	60	20	20
-14	80	40	40
-16	80	40	40

Table 5.6: Classification error rate when two extraneous point targets are placed at 0 ns and 1.2 ns respectively.

SER [dB]	NN	TIME	BIRANGE
-2	0	0	0
-8	0	20	20
-12	40	60	40
-14	40	80	40
-16	40	80	40

Table 5.7: Classification error rate when three extraneous point targets are placed at -2 ns, 0 ns, and 1.2 ns respectively.

SER [dB]	NN	TIME	BIRANGE
-4	0	0	0
-10	60	20	20
-13	60	20	20
-16	80	40	60
-18	80	60	60

Table 5.8: Classification error rate when three extraneous point targets are placed at -3 ns, 2 ns, and 3 ns respectively.

SER [dB]	NN	TIME	BIRANGE
-4	0	0	0
-10	20	20	20
-13	20	40	20
-16	40	60	40
-18	60	60	40

Table 5.9: Classification error rate when three extraneous point targets are placed at -2 ns, 0 ns, and 1.2 ns respectively with partial azimuth information (within 20°).

SER [dB]	NN	TIME	BIRANGE
-4	0	0	0
-10	20	30	20
-13	40	60	40
-16	60	60	60
-18	60	60	80

Table 5.10: Classification error rate when three extraneous point targets are placed at -3 ns, 2 ns, and 3 ns respectively with partial azimuth information (within 20°).

SER [dB]	NN	TIME	BIRANGE
-4	0	10	0
-10	40	20	0
-13	60	30	20
-16	60	40	40
-18	60	40	40

Chapter 6

CONCLUSIONS

6.1 Summary of Results

This report has investigated the use of bispectral processing methods for radar backscatter processing and for radar target identification. Bispectral processing methods were adapted to the radar signature analysis problem, and resulted in the so-called birange profile. Analysis of the birange profile showed that it was able to detect interactive scattering terms in the backscattered signal. This result led us to investigate whether this additional information could be effectively used as a discriminant for target identification.

The state of the art in time-domain radar signal processing was briefly described in Chapter II. Research on time-domain signature analysis is focused on the extraction of the major scattering components from the impulse response of a radar target. High resolution spectral estimation techniques are also being employed to realize this goal. The focus in these studies is on extracting important scattering characteristics from the impulse response. The present consideration of the bispectrum serves as a tool that enhances the feature extraction process.

In Chapter III we studied the birange profile as a tool for detecting multiple interactions. A definition for the bispectrum of complex radar signals

169

was introduced. Also, a birange estimation technique based on the "indirect bispectral estimation method" with slight modifications and suitable for radar signals was proposed and used in this report. An interpretation of the birange based on a specified scattering model which is basically a sum of complex exponentials with implicit couplings, is presented. Examples on the birange of hypothetical targets were also given. The concept of birange processing was tested using experimental measurements of scattering from a tilted flat plate and a generic aircraft model with removable parts, then using real aircraft models such as Boeing 707, 727, 747, DC 10, and the Concord. Finally, a feature extraction algorithm based on Gaussian fitting was used to locate the interactions in the birange profiles.

The extracted features were compared with the physical structure of the corresponding target model and they support the claim that the bispectrum may be used to detect multiple interactions. It is shown that it is possible to detect many responses in the birange profile using scattering data at the resonance and the optical scattering regions. Also, it is possible to detect responses in the birange that are undetectable in the transient response. However, not all interactions can be recovered from the bispectrum. It was also shown that by using the "bicoherence", one may obtain an estimate of the magnitude of interactions; thus the bicoherence is useful to separate interactions from specular responses in the impulse response.

A birange profile estimation algorithm based on AR modeling of radar signatures was introduced in Chapter IV. This algorithm was tested using both synthesized scattering data and real data. The Fourier-based birange profile of the synthesized target was reproduced using this algorithm, but the Fourier-based birange profiles of real data were slightly incompatible with those obtained using this algorithm. The reasons for incompatability of the AR-based birange estimates with the Fourier-based estimates were

investigated. It was shown that AR modeling of complex-valued signals may produce birange estimates that are entirely different from those obtained using Fourier transform. Furthermore, the transformation involved in the birange estimation procedure (from a one-dimensional all-pole response to a two-dimensional profile), produces ridges that do not belong to the birange of the target in the birange plane. Therefore, we conclude that parametric modeling of the birange may benefit from a two-dimensional AR modeling approach.

Chapter V considered the effectiveness of birange profiles for target classification. Tests were conducted using non-Gaussian noise, azimuth ambiguity, and extraneous scatterers. In general, classification results using the birange profile only were inferior to those using the impulse response or nearest neighbor classifiers. There were some cases where the birange classifier outperformed other methods. In the first case the additive noise was non-Gaussian and in the second case the responses of three extraneous point scatterers were added to the measured target frequency response.

In general, performance gains using the birange profile were slight. Also, the computational needs of the birange profile are much higher than any of the other methods considered. Based on this argument, these studies suggest that the birange profile can provide modest classification performance gain at the expense of a large increase in computation. However, these results are based on initial studies using suboptimum classifiers, and may not be true under other circumstances.

The birange as a time-domain profile is not an alternative to the impulse response but an augmentative display of target signatures. If the additional knowledge, provided by the birange, is weighted properly, then it will have positive impact on the radar target recognition problem. One may argue that, because both the transient response and the birange pro-

file are derived from the same data source, then neither one will enhance the identification process beyond what is already achieved using the data prior to any signal processing. The validity of this argument diminishes when the parameters of the underlying probability density function are not known *a priori*. Therefore, features extracted from the birange profile will potentially enhance the identification process under special circumstances.

6.2   Continuation of Research in This Area

The following research objectives are likely candidates for continuing research in this branch of radar signal processing.

Notice that the triple correlation for any limited data sequence has a hexagonal shape inside a squared region ($N \times N$). Furthermore, the hexagonal form of the triple correlation is admissable in the (t_1, t_2) plane, where "admissable" means that a replica of the triple correlation can fill the entire triple correlation plane without any gaps. Hence, it is possible to compute the birange using hexagonal fast Fourier transform methods (HFFT). By using the HFFT or hexagonal discrete Fourier transform of the triple correlation to compute the birange, the number of data storage and computations is reduced by about 25% compared to rectangular Fourier transform computation techniques.

The assumed scattering model in this report does not include dispersive targets. As in the transient response, many forms of dispersion may produce gradually decaying interactions as a function of time in the birange profile. If the returned signal decays as a function of frequency or loses energy at high frequencies, then, the triple correlation decays even faster. Similarly, if the returned signal is gaining strength at high frequencies, then the triple correlation increases significantly when including high frequency components. Therefore, it is important to adjust the lag of the

triple correlation estimate such that no significant information is lost at higher frequencies.

It may be interesting to investigate the birange profile of a class of canonical scatterers to gain additional insight about the nature of multiple interactions. The outcomes of such an investigation can then be used to better understand scattering from real radar targets.

A common problem in bispectral processing is the storage of large arrays of bispectral signatures. This problem can be avoided by employing sophisticated bispectral feature extraction methods. This can be accomplished by a thorough investigation of the parametric modeling aspect of the birange profiles. The extracted features can then be presented to a structural pattern recognition system to identify radar targets.

This report has focused on the extraction of second order multiple interactions using the bispectrum. Higher order multiple interactions can be detected using higher order spectra such as trispectrum. An investigation of this nature may have significant impact on target recognition studies, particularly because fourth order moments do not have the same shortcomings as third order moments.

Radar signatures that are used in this study correspond to the horizontal transmit horizontal receive polarization. An interesting problem is to incorporate other polarization into the birange profile. Parameters such as ellipticity and tilt of multiple interactions may be significant to radar scattering analysis [75].

Appendix A

Generation of Noise

The experiments performed in this study require the simulation of additive white Gaussian noise, colored Gaussian noise, and non-Gaussian noise. The white Gaussian noise is simulated by adding twelve uniformly distributed random variables x_i where x_i is uniform over $[-.5, .5]$. The distribution of the total sum of these random variables is the twelfth convolution of a rectangular pulse with itself which approximates a Gaussian function.

The colored Gaussian noise is simulated as the output of a stable linear AR or MA filter whose input is white Gaussian noise. The coefficients of the AR (or MA) filter define the form of coloring applied to the white noise signal (these coefficients define the spectra of the generated colored gaussian noise).

The distribution of a clutter random variable C can be modeled by a Weibull distribution, where the random variable $D = \{(C - \eta)/\alpha\}^\gamma$ has the exponential distribution

$$p_D(D) = \exp(-D). \tag{A.1}$$

Then the probability density function of C is

$$p_C(C) = \gamma/\alpha\{(C - \eta)/\alpha\}^{\gamma-1} \exp[-\{(C - \eta)/\alpha\}^\gamma] \tag{A.2}$$

The standard Weibull distribution is obtained for $\eta = 0$ and $\alpha = 1$ In this

174

case

$$E\{C\} = 1 - .57722/\gamma + .98905/\gamma^2 \qquad (A.3)$$

$$\mathrm{VAR}\{C\} = (\pi^2/6\gamma^2) \approx 1.64493/\gamma^2$$

In order to generate a random variable that has a Weibull distribution we need to generate an exponentially distributed random variable $D, p_D(D) = \exp(-D)$ then the clutter C can be computed from $D = \{(C - \eta)/\alpha\}^\gamma$, where η, γ, and α are adjustable parameters.

The method used to generate an exponentially distributed random variable is the following [16]. Let $X_i, i = 0, 1, \ldots$ be a sequence of independent random variables uniformly distributed over $[0, 1]$. Define a random variable N for $N > 0$, and N odd, such that [16]

$$X_1 < X_0, \ \sum_{j=1}^{2} X_j < X_0, \ldots, \sum_{j=1}^{N-1} X_j < X_0, \ \sum_{j=1}^{N} X_j > X_0 \qquad (A.4)$$

Then let T be the number of sequences rejected before an odd N satisfies the above conditions ($T = 0, 1, \ldots$) then the random variable $D = T + X_0$ is exponentially distributed with a standard density $\exp(-D)$ [16]. The random variable C can then be generated from D using $D = \{(C - \eta)/\alpha\}^\gamma$. Finally notice that the parameter γ plays the role of σ (the standard deviation) for a Gaussian distribution; thus reducing γ results in increasing the energy of the clutter signal and decreasing the signal to clutter ratio (SCR).

Bibliography

[1] E. M. Kennaugh and R. L. Cosgriff, "The Use of Impulse Response in Electromagnetic Scattering Problems," *1958 IRE National Conv. Rec.*, pt.1, pp. 72-77.

[2] E. M. Kennaugh and D. L. Moffatt, "Transient and Impulse Response Approximations," *Proc. IEEE*, Vol. 53, pp. 893-901, 1965.

[3] C. L. Bennett, G. F. Ross, "Time-Domain Electromagnetics and Its Applications," *Proc. of The IEEE*, Vol. 66, no. 3, pp. 299-318, March 1978.

[4] D. L. Moffatt, J. D. Young, A. A. Ksienski, H. C. Lin, and C. M. Roads, "Transient Response Characteristics in Identification and Imaging," *IEEE Trans. on Antennas and Propagation*, Vol. AP-29, no.2, pp. 192-205, March 1981.

[5] E. K. Walton, "Comparison of Fourier and maximum entropy techniques for high-resolution scattering studies," *Radio Science*, Vol. 22, no. 3, pp. 350-356, May 1987.

[6] M. P. Hurst, R. Mittra, "Scattering Center Analysis Via Prony Method," *IEEE Trans. on Antenna and Propagation*, Vol. AP-35, no. 8, pp. 986-991, August 1987.

[7] R. T. Compton, "Two Dimensional Imaging of Radar Targets With The MUSIC Algorithm," Ohio State Univ. ElectroSci. Lab. Dep. Elec. Eng., Rep. 719276-14. Dec. 1987, prepared under Contract no. GU0160 for Boing Aerospace Company.

[8] R. Carriere, R. L. Moses, "Autoregressive moving average modeling of radar target signatures," *Proc. 1988 National Conference*, Ann Arbor, MI, April 20-21, 1988, pp. 225-229.

[9] R. L. Moses, J. Carl "Autoregressive modeling of radar data with application to target identification," *Proc. 1988 National Conference*, Ann Arbor, MI, April 20-21, 1988, pp. 220-224.

[10] E. K. Walton, "Far-Field Measurements and Maximum Entropy Analysis of Lossy Material on a Conducting Plate", *IEEE Trans. on Antennas and Propagation*, Vol. 37, no. 8, pp. 1042-1048, August 1989.

[11] C. L. Nikias, M. R. Raghuveer, "Bispectrum Estimation: A Digital Signal Processing Framework," *Proc. IEEE*, Vol. 75, no. 7, pp. 869-891, July 1987.

[12] D. R. Brillinger and M. Rosenblatt, "Computation and interpretation of k-th order spectra," in *Spectral Analysis of Time Series*, B. Harris, Ed. New York, NY:Wiley, pp. 189-232, 1967.

[13] M. Rosenblatt, "Cumulants and cumulant spectra," *Time Series in Frequency Domain*, D. Brillinger and P.Krishnaiah, Eds. Amsterdam, The Netherlands: North Holland, pp. 369-382, 1983.

[14] T. S. Rao and M. M. Gabr, "An Introduction to Bispectral Analysis and Bilinear Time Series Models," Springer-Verlag, New York, 1984.

[15] E. K. Walton, I. Jouny, "Application of Bispectral Techniques to Radar Signature Analysis," *Proc. Workshop on Higher-order Spectral Analysis*, Vail, Colorado, pp. 56-61 June 1989.

[16] N. I. Johnson, S. Kotz, *Continous Univariate Distribution-1* Houghton Mifflin, 1970.

[17] S. Haykin, "Radar Signal Processing," *IEEE ASSP Magazine*, pp. 2-18, April 1985.

[18] H. L. Van Trees, *Detection, Estimation and Modulation Theory* part I. New York: Wiley 1968.

[19] M. D. Springer, *The Algebra of Random Variables*, New York: Wiley, 1979.

[20] J. S. Chen, E. K. Walton, "Comparison of Two Target Classification Techniques," *IEEE Trans. on Aerospace and Electronic Systems*, Vol. AES-22, no.1, pp. 15-21, January 1986.

[21] E. K. Walton, I. Jouny, "Application of Bispectral Techniques to Radar Scattering Signatures," *Proc. 11-th Annual Antenna Measurement Techniques Association*, Monterey, Calfornia, October 1989.

[22] A. A. Ksienski, Y. T. Lin, and L.J. White, "Low Frequency Approach to Target Identification," *Proc. IEEE*, Vol. 63, pp. 1651-1660, 1975.

[23] C. L. Nikias, R. Pan, "Time Delay Estimation in Unknown Gaussian Spatially Correlated Noise," *IEEE Trans. on Acoustics, Speech, and Signal Processing*, Vol. 36, no. 11, pp. 1706-1714, 1988.

[24] B. Bhanu, "Automatic target recognition: State of the art survey," *IEEE Transactions on Aerospace and Electronic Systems*, Vol. AES-22, no. 4, pp. 364-379, July 1986.

[25] S. C. Ahalt, F. D. Garber, I. Jouny, A. K. Krishnamurthy, "Performance of Synthetic Neural Network classification of Noisy radar Signals," *IEEE proceedings on 1988 Neural Information Processing Systems Conference*, Denver, Colorado, November 28- December 1, 1988.

[26] F. D. Garber, N. F. Chamberlain, and O. Snorrason, "Time-domain and frequency-domain feature selection for reliable radar target identification," in *proceeding of the IEEE 1988 National Radar Conference*, pp. 79-84, Ann Arbor, MI, April 20-21, 1988.

[27] G. B. Giannakis, A. Swami, "On Estimating Non-causal ARMA Non-causal processes," *Proc. Assp Workshop on Spectrum Estimation and Modeling*, pp. 187-191, August 3-5, 1988.

[28] A. Swami, J. M. Mendel, "ARMA parameter Estimation Using Only Output Cumulants," *Proc. Assp Workshop on Spectrum Estimation and Modeling*, pp. 193-198, August 3-5, 1988.

[29] B. Porat, B. Friedlander, "Optimal of MA and ARMA Parameters of NON-Gaussian Processes From Higher Order Cumulants," *Proc. Assp Workshop on Spectrum Estimation and Modeling*, pp. 208-212, August 3-5, 1988.

[30] D. L. Sherman, M. D. Zoltowski, "Eigenanalysis Based Bispectrum Estimation," *Proc. of Twenty-Sixth Annual Allerton Conference on Communication, Control, and Computing*,, pp. 249-250, September 28-30, 1988.

[31] L. M. Novak, M. B. Sechtin, M. J. Cardullo, "Studies of Target Detection Algorithms That Use Polarimetric Radar Data," *IEEE Transactions on Aerospace and Electronic Systems*, Vol. AES-25, no. 2, pp. 150-165, March 1989.

[32] G. B. Giannakis, "Cumulants: A Powerful Tool in Signal Processing," *Proceedings of The IEEE*, Vol. 75, no. 9, pp. 1333-1334, September 1987.

[33] R. O. Plaisted, H. G. Pena, "Higher Order Auto-Spectra by Maximum Entropy Method," *Geophysics*, vol. 48, pp. 1409-1410, October, 1983.

[34] C. L. Nikias, M. R. Raghauveer, "Discussion: Higher-order autospectra by maximum entropy method," *Geophysics*, Vol. 50, no. 1, pp. 165-166, January 1985.

[35] J. W. Van Ness, "Asymptotic normality of bispectral estimates," *Ann. Math. Statist.*, Vol. 37, pp. 1257-1272, 1966.

[36] M. J. Hinich, "Evidence of Nonlinearity in Daily Stock Returns," *Journal of Bus. Econ. Stat.*, Vol. 3, no. 1, pp 69-77, 1985.

[37] F. D. Garber, I. Jouny, "On M-ary Sequential Hypotheses Testing for Classification of Radar Targets," *Proc. MILCOM conference*, October 1987.

[38] F. D. Garber, A. Djouadi, "Bounds on The Bayes Classification Error Based on Pairwise Risk Functions," *IEEE Transactions on Pattern Analysis and Machine Intelligence*, Vol. PAMI-10, no. 2, pp. 281-288, March 1988.

[39] O. S. Sands, F. D. Garber, "Syntactic Pattern Recognition for Radar Target Identification," Technical Report No. 718048-2, Generated under contract No. N00014-86-k-0202, for office of Naval Research, The Ohio State University ElectroScience Laboratory, Columbus, Ohio, May 1987.

[40] H. C. Lin, "Identification of Catalogued and Uncatalogued Classes," Technical Report No. 783815-7, Generated under Grant No. AFOSR-74-2611, for Air Force Office of Scientific Research, The Ohio State University ElectroScience Laboratory, Columbus, Ohio, December, 1987.

[41] I. Jouny, F. D. Garber, "On M-ary Sequential Hypotheses Testing for Classification of Radar Signals," Technical Report No. 717220-4, Generated under contract No. N00014-85-k-0321, for Office of Naval Research, The Ohio State University ElectroScience Laboratory, Columbus, Ohio, July 1987.

[42] M. R. Raghuveer, C. L. Nikias, "Bispectrum Estimation: A parametric Approach, " *IEEE Transactions on Acoustics, Speech, and Signal Processing,* Vol. ASSP-33, no. 4, pp. 1213-1229, October 1985.

[43] A. W. Lohmann, G. Weigelt, and B. Wirnitzer, "Speckle Masking in Astronomy: Triple Correlation Theory and Application", *Applied Optics,* Vol. 22, no. 24, pp. 4028-4037, 1983.

[44] H. Bartelt, A. W. Lohmann, and B. Wirnitzer, "Phase and Amplitude Recovery From Bispectra", *Applied Optics,* Vol. 23,no. 18, pp. 3121-3129, 1984. pp. 4028-4037, 1983.

[45] Merrill I. Skolnik, "Introduction to Radar Systems", McGraw-Hill, 1980.

[46] R. J. Schalkoff, "Digital Image Processing and Computer Vision", Wiley, 1989.

[47] M. R. Raghuveer, "Time-Domain Approaches to Quadratic Phase Coupling Estimation", *IEEE Transactions on Automatic Control,* Vol. TAC-35, no. 1, pp. 48-56, 1990.

[48] M. A. Wolinsky, "Invitation to The Bispectrum", Technical Report, Applied Research Laboratories, The University of Texas at Austin, 8 February, 1988.

[49] T. Matsuoka, and T. Ulrych, "Phase Estimation Using the Bispectrum", *Proceedings of The IEEE,* Vol. 72, no. 10, October, 1984.

[50] M. Hinich, and M. Wolinsky, "A Test for Aliasing Using Bispectral Analysis", Technical Report, Applied Research Laboratories, The University of Texas at Austin, 11 August, 1986.

[51] Y. Kim, and E. J. Powers, "Digital Bispectral Analysis and Its Applications to Nonlinear Wave Interactions", *IEEE Transactions on Plasma Science,* Vol. PS-7, no. 2, June 1979.

179

[52] E. K. Walton, and I. Jouny, "Bispectral Analysis of Radar Signatures and Application to Target Classification", *Radio Science*, Vol. 25, no. 2, pp. 101-113, March-April, 1990.

[53] D. Kletter, and H. Messer, "Suboptimal Detection of Non-Guassian Signals by Third-Order Spectral Analysis," *IEEE Transactions on Acoustics, Speech, and Signal Processing*, Vol. ASSP-38, No. 6, pp. 901-909, June 1990.

[54] L. W. Couch II, "Digital and Analog Communication Systems", Macmillan, New York, New York, 1983.

[55] A. Papoulis, "Probability, Random Variables, and Stochastic Pocesses", McGraw-Hill, Second Ed., New York, 1984.

[56] D. Kletter, and H. Messer, "Optimal Detection of a Random Multitone Signal and its Relation to Bispectral Analysis", *Proc. IEEE 1990 ICASSP*, Albuquerque, New Mexico, April 1990.

[57] G. B. Giannakis, and M. K. Tsatsanis,"Signal Detection and Classification Using Matched Filtering and Higher-Order Statistics", *IEEE Transactions on Acoustics, Speech, and Signal Processing*, Vol. ASSP-38 No. 7, pp., July 1990.

[58] P. A. Nielson, and J. B. Thomas, "Detection of a Constant Signal Using The Bicovarince Function", *Proc. IEEE 1990 ICASSP*, Albuquerque, New Mexico, April 1990.

[59] Proceedings of The Workshop on Higher Order Spectra, Vail, Colorado, June 1989.

[60] S. L. Marple,"Digital Signal Processing with Applications", Prentice Hall, Englewood Cliffs, New Jersey, 1987.

[61] C. K. Papadopoulos and C. L. Nikias . "Transient Signal Estimation with Higher Order Statistics", *Proc. of Workshop on Higher Order Statistics,* Vail Colorado, pp. 89-94, 1989.

[62] E. T. Jaynes, "On the Rationale of Maximum Entropy", *Proceedings of the IEEE*, Vol. 70, no. 9, pp. 939-952, 1982.

[63] D. J. Thompson, "Multi-Window Bispectrum Estimation", *Proc. of Workshop on Higher Order Statistics,* Vail Colorado, pp. 89-94, 1989.

[64] E. K. Walton and J. D. Young, "The Ohio State University Compact Radar Cross-Section Measurement Range", *IEEE Transactions on Antenna and Propagation*, Vol. AP-32, no. 11, pp.1218-1223, November, 1984.

[65] D. Wehner, "High Resolution Radar", Artech House, Norwood, MA, 1987.

[66] W. M. Steedly and R. L. Moses, "High Resolution Exponential Modeling of Fully Polarized Radar Returns", Technical Report, No. 718048-13, Contract No. N00014-86-k0202, The Ohio State University ElectroScience Laboratory, Columbus, OH, November 1989.

[67] R. Carriere and R. L. Moses, "High Resolution Radar Target Modeling Using ARMA Models", Technical Report, No. 718048-11, Contract No. N00014-86-k0202, The Ohio State University ElectroScience Laboratory, Columbus, OH, April 1989.

[68] A. J. Kamis, E. K. Walton, F. D. Garber, "Radar Target Identification Techniques Applied to a Polarization Diverse Aircraft Data Base", Technical Report, No. 717220-2, Contract No. N00014-86-k0321, The Ohio State University ElectroScience Laboratory, Columbus, OH, March 1987.

[69] T. T. Goh., E. K. Walton, and F. D. Garber, "X-Band ISAR Techniques for Radar Target Identification," Technical Report, No. 717975-1, Contract No. V121723, The Ohio State UNiversity ElectroScience Laboratory, Columbus, OH, March 1987.

[70] "Radar Target Identification," Course Notes (1984), Department of Electrical Engineering, The Ohio State University, Columbus, OH.

[71] N. Akhter, "Far Zone Scattering from Rectangular and Triangular Dihedrals in the Principal Plane," M.S. Thesis, The Ohio State University, Department of Electrical Engineering, 1988.

[72] C. W. Chuang and D. L. Moffatt, "Complex Natural Resonances of Radar Targets Via Prony's Method," Technical Report, No. 3424-3, The Ohio State UNiversity ElectroScience Laboratory, Columbus, OH, April 1975.

[73] E. K. Walton, F. D. Garber, D. L. Moffat, and J. D. Young, "Resonant Region NCTR Research," Progress Report No. 718048-1, Contract No. N00014-86-k0202, The Ohio State University ElectroScience Laboratory, Columbus, OH, July 1986.

[74] N. N. Wang, "Reaction Formulation for Radiation and Scattering from Plates, Corner Reflectors, and Dielectric-Coated Cylinders," Technical Report, No. 2902-15, The Ohio State University ElectroScience Laboratory, Columbus, OH, April 1974.

[75] N. F. Chamberlain, "Recognition and Analysis of Aircraft Targets by Radar, Using Structural Pattern Representations Derived from Polarimetric Signatures," Ph.D. Dissertation, The Ohio State University, Columbus, OH, June 1989.

[76] O. S. Sands and F .D. Garber, "Matching of Structural Descriptions with Transitive, Anti-Symmetric Relational Attributes and Application to Radar Target Identification", submitted.

[77] E. K. Walton, "High-resolution frequency determination of discrete signal components," *Radio Science*, Vol. 19, no. 3, pp. 909-911, 1984.

[78] K. S. Lii and M. Rosenblatt,"Deconvolution and estimation of transfer function phase and coefficients for non-Gaussian linear processes," Ann. Statist., Vol. 10, pp. 1195-1208, 1982.

[79] C. L. Nikias, "Higher-Order Spectra in Signal Processing", *Tutorial Notes, Workshop on Higher-Order Spectral Analysis*, Vail Colorado, June 28, 1989.